Use of a Multivariate Analysis in the Search for Vector-Like Quarks at the LHC

Ester Amaral Simões

Mestrado em Física
Departamento de Física e Astronomia
2014

Orientador
Dr. Nuno Filipe da Silva Fernandes de Castro,
Investigador Auxiliar no Laboratório de Instrumentação e Física Experimental de Partículas

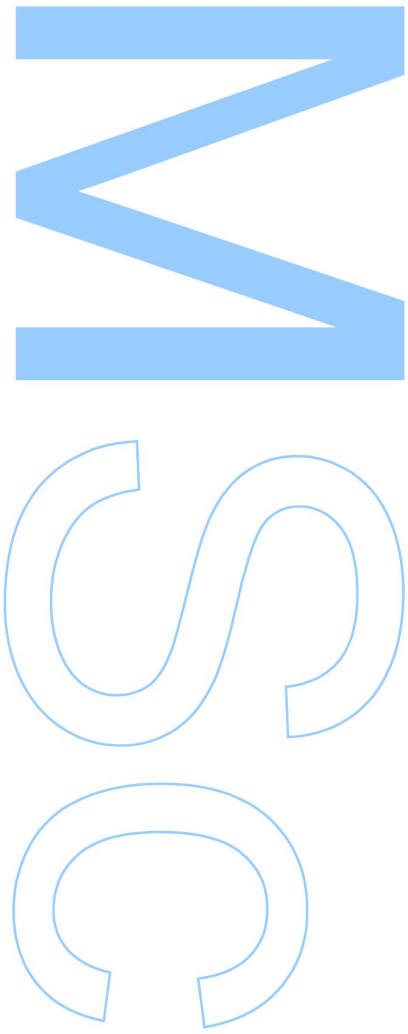

U.PORTO

FACULDADE DE CIÊNCIAS
UNIVERSIDADE DO PORTO

Todas as correções determinadas pelo júri, e só essas, foram efetuadas.

O Presidente do Júri,

Porto, _____/_____/_____

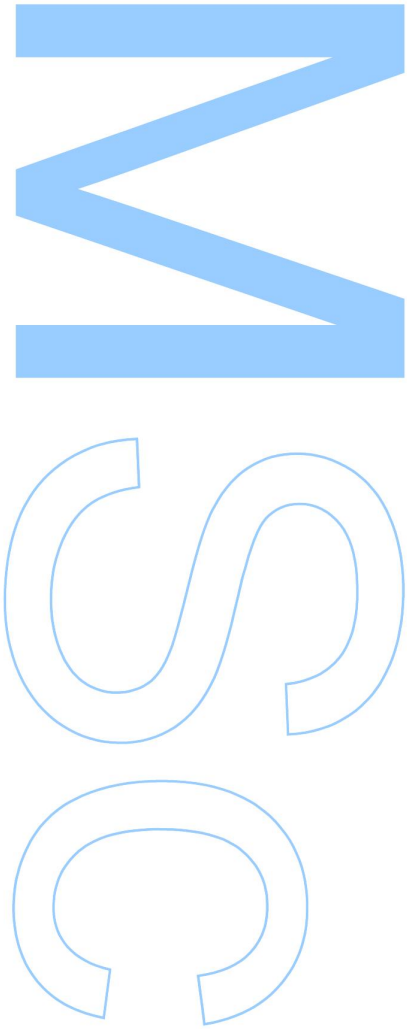

Any device in science is a window on to nature, and each new window contributes to the breadth of our view.

Cecil Frank Powell.

There is no excellent beauty that hath not some strangeness in the proportion.

Sir Francis Bacon.

Acknowledgements

First of all, my sincerest thanks to Dr. Nuno Castro, the most supportive and understanding supervisor a student can have. Thank you for all the hours spent teaching me how one can do Physics. And for this tremendously great opportunity for me.

I thank my colleague and friend Juan Pedro Araque for all the support given to me, in particular with the analysis code and the limits derivation. It was precious to learn so many things from a great programmer like you!

I thank the whole LIP-Minho team, in particular António Onofre, for all the valuable insight. To Miguel Fiolhais goes a special word of appreciation, for all the feedback and support given from as far as the other side of the Atlantic ocean!

Also, a word of gratitude towards those who taught me Physics and Mathematics since the very beginning. It has been a pleasure to learn from all of you. A special word goes to Professor José Leonardo - my Physics and Chemistry teacher - thank you for presenting me the wonderful world of thoughts, engines and stars.

I thank all my friends and colleagues over the years, the patient and the not so patient ones, for their guidance and the fruitful discussions we had. A word of appreciation and friendship goes to my dear companions André Patrício, Artur Sousa, Catarina Cosme and José Vieira.

Last but not least, I thank my mother Filomena, my father Casimiro, my sister Alice, my brother Sancho and my grandmother Júlia for all the support given during the roughest of times. It wasn't easy for you as well, I know. And to you, Tiago. You've put up with all the storms, always by my side. Thank you again.

I acknowledge Laboratório de Instrumentação e Física Experimental de Partículas (LIP) and the Portuguese ATLAS group for the significant financial support provided through the grants Bolsa de Iniciação Científica - Projecto ATLAS/LIP - CERN/FP/123595/2011 and Bolsa de Investigação (licenciado) - Projecto Estratégico nº FCOMP-01-0124- FEDER-037290 (ref.: Pest-C/FIS/LA0007/2013).

Resumo

Esta dissertação teve como objectivo a pesquisa da produção de pares de novos quarks não quirais, designados de quarks vectoriais, a partir da análise de dados colectados pelo detector ATLAS do LHC (Large Hadron Collider), localizado no CERN, no período de Abril a Dezembro de 2012, relativos a colisões protão-protão a uma energia de centro de massa de 8 TeV, correspondendo a uma luminosidade integrada de $20.3 \pm 0.6\,\mathrm{fb}^{-1}$. Com uma hipotética quarta geração sequencial de quarks quirais a ser excluída por dados do LHC, os quarks vectoriais são uma das adições ao Modelo Padrão ainda permitida por dados experimentais, sendo considerados em vários modelos de nova Física. Neste trabalho foi estudado o decaimento do quark vectorial T (B) a dar origem a um bosão Z e a um quark top (bottom). Foi considerada uma topologia dileptónica, em que um par de leptões carregados possui uma massa invariante compatível com o decaimento de um bosão de gauge Z, e em que pelo menos dois jactos são classificados como provenientes de um quark b (*b-tagged jets*). Foram identificadas algumas variáveis potencialmente úteis na separação de sinal e fundo: os momentos lineares no plano transverso dos dois jactos *b-tagged* de momento transverso mais elevado, $p_T(b1)$ e $p_T(b2)$, a soma escalar do momento transverso de todos os jactos, $H_T(\mathrm{jets})$, a massa invariante do quark vectorial T reconstruído, $M(T)$, e a distribuição angular $\Delta R(b1b2)$ entre os dois jactos *b-tagged* de momento transverso mais elevado. Estas variáveis foram usadas como input em três classificadores multivariacionais: um discriminante linear (LD), uma *boosted decision tree* (BDT) e uma rede neuronal (MLPBNN), que se determinou serem os classificadores com melhor performance. Não sendo observada nenhuma evidência para a existência de quarks pesados, os resultados obtidos antes e depois de uma análise multivariacional foram usados para colocar limites inferiores de massa de 625 GeV e 665 GeV (a 95% C.L.), respectivamente, para quarks T em singletos de $SU(2)$. Este último melhora o primeiro limite, derivado antes da aplicação de métodos multivariacionais, melhorando também o limite recentemente publicado pela Colaboração ATLAS.

Abstract

The subject of this dissertation is the search for the pair production of new non-chiral quarks, known as vector-like quarks, through the analysis of data collected by the ATLAS detector of the LHC (Large Hadron Collider), located in CERN, in the data-taking period between April and December of 2012, corresponding to an integrated luminosity of 20.3 ± 0.6 fb^{-1} of pp collisions at a center-of-mass energy $\sqrt{s} = 8$ TeV. With an hypothetical fourth sequential generation of chiral quarks being excluded by LHC data, vector-like quarks are one of the additions to the Standard Model still allowed by experimental data, being considered by several new Physics models. In this work was studied the decay of a vector-like T (B) to a Z boson and a top (bottom) quark. A dileptonic topology was considered, in which a pair of charged leptons has an invariant mass compatible with the decay of a Z gauge boson, and in which at least 2 jets are classified as coming from a $b-$quark (b-tagged jets). Some variables, potentially useful in the separation of signal from background, were identified: the linear transverse momenta of the two higher transverse momentum b-tagged jets, $p_T(b1)$ e $p_T(b2)$, the scalar sum of all the jets transverse momentum, H_T(jets), the invariant mass of the reconstructed T, $M(T)$, and the angular distribution $\Delta R(b1b2)$ between the two higher-p_T b-tagged jets. These discriminating variables were the input of three multivariate classifiers: a linear discriminant, a boosted decision tree (BDT) and a neural network (MLPBNN), categorized as the best performance classifiers. No evidence for a heavy quark signal is observed when selecting events with topologies sensitive to heavy quark pair-production via the strong interaction. The results obtained before and after a multivariate analysis were used to set lower mass limits of 625 GeV and 665 GeV (at 95% C.L.), respectively, on vector like T quarks when assuming the $SU(2)$ singlet hypothesis. The latter improves the former, derived before employing multivariate methods, improving also the limit recently published by the ATLAS Collaboration.

Contents

1 Introduction **18**

2 Theoretical Context **21**

2.1 The Standard Model of Particle Physics: an overview 21

2.2 The Lagrangian for the Standard Electroweak Model 22

2.3 Presenting Vector-like Quarks 24

2.3.1 Why are they called "vector-like" quarks? 25

2.3.2 Models with Vector-like Quarks 26

2.3.3 VLQs Representations and Couplings 26

2.3.4 VLQs Production and Decay 27

3 Experimental Apparatus **34**

3.1 CERN 34

3.2 Large Hadron Collider 35

3.3 ATLAS Detector 36

3.4 Worldwide LHC Computing Grid 39

4 Building the Analysis: $T \to Zt$ and $B \to Zb$ **41**

4.1 Data Sample 41

4.2 Trigger 42

4.3 Presenting Primary Physics Objects 43

4.4 Signal Modeling 45

4.5 Background Modeling 47

4.6 Search Strategy and Event Selection 48

4.7 Discriminating Variables 58

5 Multivariate Analysis with TMVA **67**

5.1 Multivariate Analysis Classifiers outlined 67

5.2 Training/testing MVA Classifiers 70

5.3 Applying MVA Classifiers 75

6 Results **78**

6.1 Limits On the Singlet T Quark Pair-Production Hypothesis 78

6.1.1 Before MVA 78

6.1.2 After MVA 79

7 Conclusions and Further Work **82**

Bibliography **82**

List of Figures

2.3.1 Observed lower limits at 95% C.L. on the mass of vector-like T (a) and B (b) quarks for ATLAS searches with 14.3 fb^{-1} and 20.3 fb^{-1} of 8 TeV data. 29
2.3.2 Observed lower limits at 95% C.L. on the mass of vector-like T (a) and B (b) quarks for CMS searches with 19.5 fb^{-1} and with 19.6 fb^{-1} of 8 TeV data, respectively (extracted from [1, 2]). 30
2.3.3 A representative diagram illustrating heavy quark pair production and vector-like decay modes (extracted from [3]). 30
2.3.4 The pair production cross section versus quark mass as predicted by HATHOR [4] for pp collisions at $\sqrt{s} = 7$ TeV and 8 TeV. The bottom panel shows the 8 TeV/7 TeV cross section ratio (extracted from [5]). . . 31
2.3.5 Vector-like T quark branching ratios (a) to the Wb, Zt, and Ht decay modes as a function of the T quark mass, computed with PROTOS [6] for an $SU(2)$ singlet and two types of doublets. Likewise, vector-like B quark branching ratios (b) to the Wt, Zb, and Hb decay modes for a singlet and two types of doublets (extracted from [3]). 32

3.2.1 Scheme of the LHC experiments ATLAS, ALICE, CMS and LHCb; and preaccelerators PS (Proton Synchrotron) and SPS (Super Proton Synchrotron); figure extracted from [7]. 36
3.3.1 Representation of ATLAS coordinate system: the side-A of the detector is defined as the one with positive z and side-C as that with negative z. The azimuthal angle ϕ is measured around the beam axis, and the polar angle θ is measured from the beam axis (figure extracted from [7]). . . . 37
3.3.2 Cut-away view of the ATLAS detector. The dimensions of the detector are 25 m in height and 44 m in length. The overall weight of the detector is approximately 7000 tonnes (figure extracted from [8]). 39

4.1.1 The cumulative luminosity delivered (green) versus time, recorded by ATLAS (yellow), and certified to be good quality data (blue) during stable beams and for pp collisions at 7 and 8 TeV centre-of-mass energy in 2011 and 2012. 42
4.1.2 Luminosity-weighted distribution of the mean number of interactions per crossing for 2012; full pp collisions dataset. 43
4.3.1 Performance (light-flavour rejection versus b-jet efficiency) of the MV1 tagging algorithm, as evaluated for jets with $p_T > 20$ GeV and $|\eta| < 2.5$ in a sample of simulated $t\bar{t}$ events (extracted from [9]). 45
4.3.2 Efficiency of the MV1 tagger to select b, c, and light-flavour jets, as a function of jet p_T (upper plot) and $|\eta|$ (lower plot). The weight selection on the MV1 output discriminant is chosen to be 70% efficient for b-jets with $p_T > 20$ GeV and $|\eta| < 2.5$, as evaluated on a sample of simulated $t\bar{t}$ events (extracted from [9]). 46
4.6.1 Unit-normalized distributions in the $ee + \mu\mu$ channel. Panel (a) displays the jet multiplicity, before requiring for 2 jets (after only requiring a Z boson candidate); panel (b) presents the b-tagged jets multiplicity, before requiring for two b-tagged jets (after a $Z+ \geq 2$ jets selection); panels (c) and (d) present the $p_T(Z)$ and H_T(jets) distributions, before a $p_T(Z) > 150$ GeV and H_T(jets) > 600 GeV selection, respectively. The filled histogram corresponds to SM backgrounds, while the red and blue solid lines correspond to the $T\bar{T}$ and $B\bar{B}$ signal, respectively, assuming a heavy quark mass of 650 GeV with vector-like singlet branching ratios. . 50
4.6.2 The E and p_T distributions for leptons, in the $ee + \mu\mu$ channel, after requiring $Z+ \geq 2$ jets. 51
4.6.3 The η and ϕ distributions for leptons, in the $ee + \mu\mu$ channel, after requiring $Z+ \geq 2$ jets. 52
4.6.4 Distributions for the Z boson candidate, in the $ee + \mu\mu$ channel, after requiring $Z+ \geq 2$ jets. Panels (a) and (b) show the invariant mass, $M(Z)$, panels (c) and (d) show the energy E, while (e) and (f) show the transverse momentum, $p_T(Z)$. 53
4.6.5 The η and ϕ distributions for the Z boson candidate, in the $ee + \mu\mu$ channel, after requiring $Z+ \geq 2$ jets. 54
4.6.6 Distribution of b-tagged jets multiplicity, in the $ee + \mu\mu$ channel, after requiring $Z+ \geq 2$ jets. 54

4.6.7 The p_T distributions of the highest-p_T b-tagged jet, in the $ee+\mu\mu$ channel, after requiring $Z+ \geq 2$ jets and $N_{tag} \geq 2$. 55
4.6.8 The p_T distributions of the second higher-p_T b-tagged jet, in the $ee + \mu\mu$ channel, after requiring after requiring $Z+ \geq 2$ jets and $N_{tag} \geq 2$. 55
4.6.9 The p_T distribution for the Z boson candidate, in the $ee + \mu\mu$ channel, after requiring $Z+ \geq 2$ jets , $N_{tag} = 1$ (upper panel) and $N_{tag} \geq 2$ (down panel). 56
4.6.10 The H_T(jets) distribution, in the $ee+\mu\mu$ channel, after requiring $p_T(Z) >$ 150 GeV; for $N_{tag} = 1$ (a) and $N_{tag} \geq 2$ (b). 57
4.6.11 The $m(Zb)$ invariant mass distributions, in the $ee + \mu\mu$ channel, after requiring $H_T > 600$ GeV. Upper panels: $N_{tag} = 1$; down panels: $N_{tag} \geq 2$. 59
4.6.12 The $m(Zb)$ invariant mass distributions, in the $ee + \mu\mu$ channel, after requiring $p_T(Z) > 150$ GeV. 60
4.6.13 The invariant mass (a), p_T (b), η (c) and ϕ (d) distributions for the reconstructed (hadronic) W boson invariant mass (from 2 jets, excluding the dominant b-jet), in the $ee + \mu\mu$ channel, after requiring $p_T(Z) >$ 150 GeV and $N_{tag} \geq 2$. 61
4.6.14 The invariant mass (a), p_T (b), η (c) and ϕ (d) distributions for the reconstructed T invariant mass (from W and the Zb system), in the $ee+\mu\mu$ channel, after requiring $p_T(Z) > 150$ GeV and $N_{tag} \geq 2$. 62
4.6.15 The ΔR distributions between the two higher-p_T b-tagged jets, in the $ee + \mu\mu$ channel, after requiring $p_T(Z) > 150$ GeV and $N_{tag} \geq 2$. 63
4.6.16 The ΔR distributions between the two leptons (from the Z boson candidate reconstruction), in the $ee + \mu\mu$ channel, after requiring $p_T(Z) >$ 150 GeV and $N_{tag} \geq 2$. 63
4.6.17 The ΔR distributions between the highest-p_T b-tagged jet and the first lepton (used in the Z boson candidate reconstruction), in the $ee + \mu\mu$ channel, after requiring $p_T(Z) > 150$ GeV and $N_{tag} \geq 2$. 64
4.6.18 The ΔR distributions between the highest-p_T b-tagged jet and the second lepton (used in the Z boson candidate reconstruction), in the $ee + \mu\mu$ channel, after requiring $p_T(Z) > 150$ GeV and $N_{tag} \geq 2$. 64
4.6.19 The ΔR distributions between the second higher-p_T b-tagged jet and the first lepton (used in the Z boson candidate reconstruction), in the $ee+\mu\mu$ channel, after requiring $p_T(Z) > 150$ GeV and $N_{tag} \geq 2$. 65

4.6.20 The ΔR distributions between the second higher-p_T b-tagged jet and the second lepton (used in the Z boson candidate reconstruction), in the $ee + \mu\mu$ channel, after requiring $p_T(Z) > 150$ GeV and $N_{tag} \geq 2$. 65
4.7.1 The chosen discriminating variables: (a) $p_T(b1)$, (b) $p_T(b2)$, (c) H_T(jets), (d) $\Delta R(b1b2)$ and (e) T invariant mass, in the $ee + \mu\mu$ channel, after requiring $p_T(Z) > 150$ GeV and $N_{tag} \geq 2$. 66

5.1.1 Schematic view of a decision tree. Starting from the root node, a sequence of binary splits using the discriminating variables x_i is applied to the data. Each split uses the variable that at this node gives the best separation between signal and background when being cut on. The same variable may thus be used at several nodes, while others might not be used at all. The leaf nodes at the bottom end of the tree are labeled "S" for signal and "B" for background depending on the majority of events that end up in the respective nodes (figure extracted from [10]). 68
5.1.2 Multilayer perceptron (MLP) neural network with one hidden layer. . . 69
5.2.1 Unit-normalized input variable distributions, in the $ee+\mu\mu$ channel, after requiring $p_T(Z) > 150$ GeV and $N_{tag} \geq 2$. The reference signal displayed corresponds to $T\overline{T}$ production assuming $SU(2)$ singlet quarks with a mass of 700 GeV. Upper panel, from left to right: $p_T(b1)$, $p_T(b2)$ and H_T(jets). Down panel, from left to right: $\Delta R(b1b2)$ and the reconstructed T quark invariant mass. The vertical text on the right-hand side of the plots indicates the under- and overflows. 71
5.2.2 Linear correlation coefficients between the discriminating variables used: (a) for a $T\bar{T}$ production signal sample, assuming $SU(2)$ singlet quarks with a mass of 700 GeV; for the total background sample (b). These coefficients are obtained after training (and testing) the classifiers with the aforementioned samples as input. 72
5.2.3 Linear correlation coefficients between the discriminating variables used for the data sample. 73
5.2.4 Background rejection versus signal efficiency plot (ROC curve) for the BDT, LD and MLPBNN classifiers, which are known to have a good performance, as verified by the area covered by their respective curves. The ROC curve for the automatic cuts performed by the MVA algorithm is also shown for comparison. 74

5.2.5 Overtraining test, with training and testing samples superimposed, for: (a) BDT, (b) LD and (c) MLPBNN classifiers. 76
5.3.1 Output of the multivariate classifiers employed in this MVA: (a) BDT, (b) LD and (c) MLPBNN. The signal contribution is multiplied by a factor of 10. The leftmost bin in each histogram contains underflow events. . . . 77

6.1.1 Predicted pair-production cross section as a function of the heavy quark mass and observed and expected upper limits for an $SU(2)$ singlet T quark. 79
6.1.2 Predicted pair-production cross section as a function of the heavy quark mass and observed and expected upper limits for an $SU(2)$ singlet T quark, derived with the outputs of (a) BDT, (b) LD and (c) MLPBNN classifiers. 80

List of Tables

2.1 The electroweak quantum numbers for the first generation of quarks and leptons. 24

2.2 Possible representations for vector-like quarks, with quantum numbers under $SU(2)_L$ and $U(1)_Y$ and Yukawa mixing terms in the Lagrangian, $\mathcal{L}_Y$. The Higgs boson is denoted as $H^{(c)}$ when it can be H or H^c, depending on the representation chosen. The gauge invariant mass term $\mathcal{L}_m$ common to all representations for VLQs is a striking feature of these new heavy quarks (table adapted from [11]). 27

3.1 General performance goals of the ATLAS detector (extracted from [8, 12]). For high-p_T muons, the muon spectrometer performance is independent of the inner-detector system. The unit employed for E and p_T is GeV. . . 40

4.1 Listed are the predicted and observed number of events ($ee+\mu\mu$ channel), and the statistical uncertainties associated, after the indicated selection levels, for reference $B\overline{B}_S$ and $T\overline{T}_S$ signal yields assuming $m_{B/T} = 650\,\text{GeV}$ and $SU(2)$ singlet branching ratios. SM backgrounds yields are listed by category, as well as the combined total. The events for the rightmost three selection levels contain at least two b-tagged jets (signal region). . . 49

6.1 Observed (expected) 95% C.L. limits on the T quark mass (GeV), assuming pair production of $SU(2)$ singlet quarks, before (left) and after a multivariate analysis (right). 81

List of Abbreviations

AGS	Alternating Gradient Synchrotron
ANN	Artificial Neural Network
ALICE	A Large Ion Collider Experiment
ATLAS	A Toroidal LHC ApparatuS
BDT	Boosted Decision Tree
BR	Branching Ratio
BSM	Beyond Standard Model
CERN	*Conseil Européen pour la Recherche Nucléaire*
C.L.	Confidence Level
CKM	Cabbibo-Kobayashi-Maskawa
CMS	Compact Muon Solenoid
EM	Electromagnetic
FCNC	Flavour-Changing Neutral Currents
GUT	Grand Unified Theory
HEP	High Energy Physics
ID	Inner Detector
JES	Jet Energy Scale
JVF	Jet Vertex Fraction
LAr	Liquid Argon

LHC	Large Hadron Collider
LHCb	Large Hadron Collider beauty
MC	Monte Carlo
MLP	Multi-layer Perceptron
MVA	Multivariate Analysis
NNLO	Next-to-next-to-leading-order
LO	Leading Order
PDF	Parton Distribution Function
PS	Proton Synchrotron
QCD	Quantum Chromodynamics
ROC	Receiver Operating Characteristic
RoI	Region-of-Interest
SCT	Silicon Microstrip Trackers
SM	Standard Model
SPS	Super Proton Synchrotron
SSB	Spontaneous Symmetry Breaking
SU	Special Unitary
SUSY	Supersymmetry
TMVA	Toolkit for Multivariate Data Analysis
TRT	Transition Radiation Tracker
UA1	Underground Area 1
UA2	Underground Area 2
VEV	Vacuum Expectation Value

VLQ Vector-Like Quark

WLCG Worldwide LHC Computing Grid

1 Introduction

A centrepiece of the Standard Model of Particle Physics (SM), described by the $SU(3) \otimes SU(2) \otimes U(1)$ gauge group, is the formulation of the electroweak interactions as arising from a spontaneously broken gauge symmetry. This hypothesis has been confirmed with incredible success by experimental physics programs over the past four decades, most notably by the LEP (Large Electron-Positron) and SLC (Stanford Linear Collider) collider programs [13, 14]. Nevertheless, the nature of the symmetry breaking mechanism is not yet fully understood. The Higgs boson, as proposed within the frame of the Standard Model, is the simplest manifestation of the Englert-Brout-Higgs-Guralnik-Hagen-Kibble [15, 16, 17] mechanism. The ATLAS and CMS collaborations have discovered a convincing candidate for the Higgs boson with a mass around 126 GeV at the CERN Large Hadron Collider (LHC) [18, 19]. Hence, the default electroweak symmetry breaking mechanism, whereby a weak isospin doublet of fundamental scalar fields obtains a vacuum expectation value, remains a valid assumption. Even though the Standard Model is currently the best description there is of the subatomic world, it is unlikely that it stands as the ultimate theory. It is of the uttermost importance to investigate what may lie beyond the SM and try to solve several unanswered questions, such as: how to explain the number of fermion generations and mass hierarchy? What is the origin of the matter-antimatter asymmetry? What is the nature of Dark Matter? Can we incorporate gravity in the SM? What is the mass of neutrinos, and do they follow Majorana or Dirac statistics? The Standard Model is generally regarded as a low-energy approximation of a more fundamental theory with new degrees of freedom and symmetries that would only manifest themselves at higher energies, i.e. we assume that the SM remains valid up to a cut-off scale Λ. Indeed, the SM violates a concept of naturalness [20] when extrapolated to energies above the electroweak scale, as fine tuning is required to account for the quadratic mass-squared divergences of fundamental scalar fields (such as the Higgs). Hence, naturalness demands these divergences to be cancelled, typically at a scale below 1 TeV. Models of physics beyond the SM (BSM models) typically address this issue by postulating a new symmetry, as in supersymmetry SUSY [21, 22, 23, 24].

In SUSY - a Bose-Fermi symmetry [25, 26] - new states related to the SM fermions and bosons introduce new interactions (new symmetries) that cancel the quadratically divergent ones. This new symmetry could also be a spontaneously broken global symmetry of the extended theory, with the Higgs boson emerging as a pseudo-Nambu-Goldstone boson [27]. This "collective" symmetry breaking is the essential ingredient in Little Higgs [28, 29] and Composite Higgs [30, 31] models, which are weakly coupled extensions of the Standard Model with little or no fine tuning. These latter models (amongst many others) share one of the simplest additions to the Standard Model: the introduction of isosinglet vector-like quarks (VLQs) [32] - a strategy supported by several theoretical motivations [33, 34, 35]. Vector-like quarks are hypothetical color-triplet, spin-$\frac{1}{2}$ fermions, whose left- and right-handed chiral components have the same transformation properties under the weak-isospin gauge group $SU(2)$, i.e. their left- and right-handed components have the same color and electroweak quantum numbers. Such quarks could mix with like-charge SM quarks [35, 36, 37, 38], and the mixing of the SM top quark with a charge $+\frac{2}{3}$ vector-like quark could play a role in regulating the divergence of the Higgs mass-squared. Hence, vector-like quarks emerge as an exciting subject in searches of new physics, since they are a characteristic feature of plenty non-supersymmetric natural models [39]. Furthermore, they are attracting a lot of attention since a fourth sequential generation of chiral quarks was excluded by experiments at the LHC [40], and by recent measurements for Higgs-mediated cross-sections [41, 42], when combined with results of direct searches at the Large Hadron Collider [43, 44]. Previous searches targetting a hypothetical fourth sequential generation of quarks were able to provide a vector-like quark interpretation [44]. Unlike chiral quarks, vector-like quarks are able to decay through neutral-current channels, since the GIM mechanism [45] ceases to operate with the addition of VLQs to the Standard Model. These extra heavy quarks, decaying through neutral-current channels, have been the aim of searches at the CERN Large Hadron Collider, by the ATLAS and CMS collaborations [46, 47, 48, 49, 50].

Since no evidence for a heavy quark signal was observed by these collaborations, the results obtained were used to set lower mass limits for the vector-like quarks in study [49, 51, 52]. Indeed, the CMS Collaboration published a vector-like T quark search, setting lower mass limits in the range of $690 - 780$ GeV [1], at a 95% confidence level (C.L.). Furthermore, just recently, the ATLAS Collaboration published a vector-like quark search [3], in which results were used to set lower mass limits of 685 GeV and 755 GeV (at 95% C.L.) on vector like B quarks, when assuming the $SU(2)$ singlet and doublet hypotheses, respectively. Likewise, lower mass limits of 655 GeV and 735 GeV

(at 95% C.L.) were obtained for vector-like T quarks when assuming the $SU(2)$ singlet and doublet hypotheses, respectively, depending on the assumptions for the branching ratios.

The present thesis is organized as follows: the SM and the addition of vector-like quarks to it are discussed in chapter 2; the experimental apparatus, including the ATLAS detector, is described in chapter 3; the construction of the analysis is described in chapter 4, the work with the multivariate techniques is explained in chapter 5 and the results are presented in chapter 6. The conclusions of this work, as well as some future work ideas, are drawn in chapter 7.

2 Theoretical Context

In this chapter, we briefly present and discuss the Standard Model of Particle Physics and the consequences of adding vector-like quarks to it.

2.1 The Standard Model of Particle Physics: an overview

In 1961, Glashow [53] first proposed the idea that the electromagnetic and weak interactions may be unified in a gauge theory based on the group $SU(2)\otimes U(1)$, which combines different massless chiral[1] states. Consider, for instance, a Universe in which quarks and leptons have no mass at all. At first, this could appear to be a surprising supposition. Nonetheless, the massless limit is where the present Standard Model begins. The seeming problem of generating masses in a manner consistent with gauge invariance was solved later by Weinberg and Salam, using the idea of "spontaneous symmetry breaking" (an expression coined by Baker & Glashow, in 1962), by introducing Higgs fields. The resulting theory, known as the Glashow-Weinberg-Salam model, was shown by 't Hooft [54, 55] to be a renormalizable quantum field theory. All these contributions combine to present us with what is known as the Glashow-Weinberg-Salam model gauge theory of the electroweak interactions, whose input fermionic degrees of freedom are massless spin one-half chiral particles. It has the group structure $SU(2)_L \otimes U(1)_Y$, where the $SU(2)_L$, $U(1)_Y$ represent weak isospin and weak hypercharge, respectively. We define the hypercharge Y as $Q = T_3 + \frac{1}{2}Y$, in analogy with the original Gell-Mann-Nishijima [56, 57] formula for strong interaction quantum numbers, where Q is the electric charge (in units of the positron charge, e) and T_3 is the third component of the weak isospin operator. The subscript "L" on $SU(2)_L$ indicates that among fermions, only left-handed states transform nontrivially under weak isospin. In fact, only left-handed components

[1] Chirality is defined as the eigenvalue of γ_5 ($\gamma_5 = i\gamma_0\gamma_1\gamma_2\gamma_3$, in the Dirac basis); with $\gamma_5 = 1$ corresponding to right-handedness, and $\gamma_5 = -1$ to left-handedness, where left- and right-handed fermion fields may be written as: $\psi_L = \frac{1}{2}(1-\gamma_5)\,\psi$, $\psi_R = \frac{1}{2}(1+\gamma_5)\,\psi$.

are coupled in the charge changing sector, whereas right-handed components provide mass.

The electroweak interactions that result from gauging $SU(2) \otimes U(1)$ reproduce all known phenomena (and predict new ones!), in particular the structure of neutral currents and the existence of gauge vector bosons, which have all been successfully verified experimentally.

Aditionally, Quantum Chromodynamics (QCD) - the theory of strong interactions - was developed in parallel with the supracited model of weak interactions through the 60s and 70s. In 1964, Murray Gell-Mann and George Zweig independently suggested the existence of quarks with different flavors as the components of hadrons [58]. In 1965, Moo-Young Han with Yoichiro Nambu [59] and Oscar W. Greenberg [60] proposed an additional gauge degree of freedom, the color charge. Since each quark has now three possible colours (RGB: red, green and blue), we can describe any particular quark flavour by a three component field $\psi(x) = [\psi(R, x), \psi(G, x), \psi(B, x)]$ and consider local gauge transformations where $\Lambda(x)$ is a 3×3 hermitian matrix operating on ψ. These transformations can change the color and belong to the symmetry group $SU(3)_C$. Now, to achieve local gauge invariance is required the introduction of eight massless gauge bosons - gluons - which carry pairs of colour labels. Quantum Chromodynamics reached its present form in 1973 with the discovery of asymptotic freedom of strong interactions by David Politzer [61, 62] and David Gross, together with Frank Wilczek [63]. Combining QCD with the Glashow-Weinberg-Salam model gives an $SU(3)_C \otimes SU(2)_L \otimes U(1)_Y$ [2] gauge invariant theory of the strong and electroweak forces, commonly known as the Standard Model of Particle Physics.

2.2 The Lagrangian for the Standard Electroweak Model[3]

All the pieces are now in place for presenting a model that is not simply an illustrative elegant "toy", rather it appears to describe quite well the universe we inhabit. The standard electroweak model is based on the gauge group [64] $SU(2) \otimes U(1)$, with gauge bosons W^i_μ, $i = 1, 2, 3$, and B_μ, for the $SU(2)$ and $U(1)$ gauge groups, respectively, and

[2] The subscript "C" in SU(3) stands for color.

[3] For what comes next, our notation and conventions are as follows: The metric $g_{\mu\nu}$ in an inertial coordinate system has diagonal elements $+---$; we use the Einstein's summation convention over repeated indices; greek indices run over the four space-time inertial coordinate labels t, x, y, z; and unless otherwise indicated, $c = \hbar = 1$.

the corresponding gauge coupling constants g and g' [4]. The left-handed fermion fields of the i^{th} fermion family transforms as doublets $\psi_i = \begin{pmatrix} \nu_i \\ l_i^- \end{pmatrix}$ and $\begin{pmatrix} u_i \\ d_i' \end{pmatrix}$ under $SU(2)$, where $d_i' \equiv \sum_j V_{ij} d_j$, V is the Cabbibo-Kobayashi-Maskawa mixing matrix (which rules the mixing between quarks). The right-handed fields are $SU(2)$ singlets. There is in Nature a replication of the fermion multiplets. Indeed, the number n_g of fermion generations in the SM is not imposed by any symmetry principle. Experimentally, there is strong evidence that $n_g = 3$. So, the SM incorporates three fermion families (three quark generations and three lepton generations) and a single complex Higgs doublet $\Phi = \begin{pmatrix} \Phi^+ \\ \Phi^0 \end{pmatrix}$, which is introduced for mass generation[5]. After SSB (spontaneous symmetry breaking), the Lagrangian for the fermion fields, ψ_i, is given by [65]:

$$\mathcal{L}_F = \sum_i \bar{\psi}_i \left(i\gamma^\mu \partial_\mu - m_i - \frac{g m_i H}{2 m_W} \right) \psi_i \tag{2.2.1}$$

$$-\frac{g}{2\sqrt{2}} \sum_i \bar{\Psi}_i \gamma^\mu \left(1 - \gamma^5\right) \left(T^+ W_\mu^+ + T^- W_\mu^- \right) \Psi_i$$

$$-e \sum_i Q_i \bar{\psi}_i \gamma^\mu A_\mu \psi_i$$

$$-\frac{g}{2\cos\theta_W} \sum_i \bar{\psi}_i \gamma^\mu \left(g_V^i - g_A^i \gamma^5 \right) \psi_i Z_\mu .$$

The weak angle $\theta_W \equiv \arctan(g'/g)$, where $g = \frac{e}{\sin\theta_W}$ and $g' = \frac{e}{\cos\theta_W}$ (e is the positron electric charge), is a parameter of the model. The following quantities are now defined: $M_W = \frac{A}{\sin\theta_W}$, $A \equiv B\cos\theta_W + W^3 \sin\theta_W$ is the (massless) photon field, whilst $W^\pm \equiv (W^1 \mp i W^2)/\sqrt{2}$ and $Z \equiv -B\sin\theta_W + W^3\cos\theta_W$ are the massive charged and neutral weak boson fields, respectively. T^+ and $T^-$are the weak isospin raising and lowering operators, with $T^\pm = (T_1 + T_2)/\sqrt{2}$, where $T_i = \frac{1}{2}\tau_i$ and τ_i are the Pauli matrices. The vector and axial-vector couplings are $g_V^i \equiv t_{3L}(i) - 2Q_i \sin^2\theta_W$ and $g_A^i \equiv t_{3L}(i)$, where $t_{3L}(i)$ is the weak isospin of fermion i ($+\frac{1}{2}$ for u_i and ν_i; $-\frac{1}{2}$ for d_i and l_i - refer to table 2.1); Q_i is the charge operator, it returns the charge value of ψ_i in units of e.

[4] For the strong interaction we would also have a similar description based on the $SU(3)$ gauge group.

[5] When introducing a set of scalar fields Φ, this set develops a $U(1)_{em}$ symmetric vacuum expectation value $< \Phi >_0$ so that we have the following pattern of symmetry breaking: $SU(2)_L \times U(1)_Y \xrightarrow{< \Phi >_0} U(1)_{em}$. Three of the original four $SU(2 \times U(1)$ gauge bosons acquire mass, while one (the photon) remains massless.

	T	T_3	$\frac{1}{2}Y$	Q
ν_{eL}	$\frac{1}{2}$	$\frac{1}{2}$	$-\frac{1}{2}$	0
e_L	$\frac{1}{2}$	$-\frac{1}{2}$	$-\frac{1}{2}$	-1
u_L	$\frac{1}{2}$	$\frac{1}{2}$	$\frac{1}{6}$	$\frac{2}{3}$
d_L	$\frac{1}{2}$	$-\frac{1}{2}$	$\frac{1}{6}$	$-\frac{1}{3}$
e_R	0	0	-1	-1
u_R	0	0	$\frac{2}{3}$	$\frac{2}{3}$
d_R	0	0	$-\frac{1}{3}$	$-\frac{1}{3}$

Table 2.1: The electroweak quantum numbers for the first generation of quarks and leptons.

The first term in $\mathcal{L}_F$ (eq. 2.2.1) contains the Yukawa coupling of H [6] to ψ_i, and the usual free-field term, m_i is the mass of the i^{th} fermion ψ_i. In non-minimal models it is also possible to include additional charged and neutral scalar Higgs fields. The second term in our Lagrangian describes the charged-current weak interaction [66, 67]. For $q^2 \ll M_W^2$, this term reduces to the four-fermion interaction[7], with the Fermi constant given (at tree level) by $G_F/\sqrt{2} = g^2/8M_W^2$. The third term represents the electromagnetic interaction (QED) and the last one is the weak neutral-current interaction.

The Standard Model, as summarized by the Lagrangian in eq. 2.2.1, predicts a definite pattern of quark mixing: flavour-changing neutral currents (FCNC) are absent at tree level and suppressed at one loop by the GIM mechanism [45], with a branching ratio of the order of 10^{-14}, and the mixing in charged currents is given by the unitary Cabbibo-Kobayashi-Maskawa (CKM) matrix [68].

2.3 Presenting Vector-like Quarks

Vector-like quarks present themselves as a very promising playground for searches of new physics. They are one of the simplest examples of extra (colored) fermions still allowed by experimental data. Vector-like quarks at the TeV scale are strongly motivated by (at least) two theoretical ideas, usually combined: they are required if the Higgs is a pseudo-Goldstone boson to induce electroweak symmetry breaking and account for the observed lightness of the Higgs [69, 70, 71], as they emerge as fermion ressonances in

[6] H is the physical neutral scalar which is the only remaining part of Φ after spontaneous symmetry breaking. A Yukawa coupling is the general term for an interaction between fermions and scalars of the form $\bar{\psi}\psi\Phi$.

[7] Fermi's theory involves a weak Lagrangian which is a product of four fermion fields: $\bar{\psi}_p\psi_n\bar{\psi}_e\psi_\nu$.

flavour theories of *partial compositeness* [72, 73] [8].

But how are these hipothetical new heavy fermions characterized? A fermion is defined to be vector-like if its left- and right- handed chiralities belong to the same representation of the symmetry group of the underlying theory: for the Standard Model, $G \equiv SU(3)_c \otimes SU(2)_L \otimes U(1)_Y$.

2.3.1 Why are they called "vector-like" quarks?

Vector-like quarks, as seen before, feature a striking characteristic: their left and right handed chiralites transform in the same way under the Standard Model (SM) gauge groups $SU(3)_c \times SU(2)_L \times U(1)_Y$.

But why are they called "vector-like"?

A concise summary of the present knowledge of (charged) weak interactions is given by the following Lagrangian density[74]:

$$\mathcal{L}_{\mathcal{W}} = gW_a(x)[J^a_W(x) + j^a_W(x)] + h.c., \tag{2.3.1}$$

where the $J^a_W(x)$ is the quark weak current and $j^a_W(x)$ is the lepton weak current, which are coupled to a massive charge vector field $W_a(x)$.

Now, if excluding the lepton charged currents, the Lagrangian density is of the form:

$$\mathcal{L}_{\mathcal{W}} = \frac{g}{\sqrt{2}}\left[J^{\mu+}W^+_\mu + J^{\mu-}W^-_\mu\right], \tag{2.3.2}$$

Let us compare Standard Model chiral quarks with these vector-like quarks. The charged currents associated with chiral quarks are only left handed, i.e. $J^{\mu+} = J^{\mu+}_L + J^{\mu+}_R$, with:

$$\begin{cases} J^{\mu+}_L = & \bar{u}_L\gamma^\mu d_L = \bar{u}_L\gamma^\mu(1-\gamma^5)d = V - A(\text{vector-axial current}) \\ J^{\mu+}_R = & 0 \end{cases} \tag{2.3.3}$$

On the other hand, vector-like quarks have both left and right handed charged currents:

$$J^{\mu+} = J^{\mu+}_L + J^{\mu+}_R = \bar{u}_L\gamma^\mu d_L + \bar{u}_R\gamma^\mu d_R = V, \tag{2.3.4}$$

which, unlike chiral quark currents, transform as a vector, henceforth justifying the designation attributed to these quarks.

[8] The quarks and leptons acquire a mass by mixing with composite fermions.

2.3.2 Models with Vector-like Quarks

Vector-like quarks are the key ingredient in many theoretical BSM models - some of the most popular scenarios which include them are outlined next:

- Composite Higgs (Georgi-Kaplan) Models: the electroweak symmetry breaking is prompted by a condensate of the top quark and a vector-like singlet, invoking a seesaw mechanism between the two states [75, 76, 77, 78];
- Extra Dimensions: excited partners of Standard Model quarks belonging to heavier tiers of universal extra dimensional are vector-like fermions;
- Gauging of the flavour group: vector-like fermions are necessary for anomaly cancellation and can play a role in the mechanisms of quark mass generation [79, 80];
- Little Higgs Models: vector-like states emerge as partners of Standard Model fermions in larger representations of the symmetry group [28, 69, 29];
- Supersymmetric non-minimal extensions of the SM: vector-like matter can be introduced in non-minimal supersymmetric models to enhance corrections to the Higgs mass, without affecting too much electroweak precision measurements [81, 82]. VLQs also appear in non-minimal, GUT-inspired, supersymmetric scenarios [83].

2.3.3 VLQs Representations and Couplings

The simplest scenarios with vector-like quarks present (besides SM particles) are those in which the new quarks interact with SM quarks and the Higgs boson through Yukawa couplings. Classifying vector-like quarks in multiplets of $SU(2)_L$ allows us to write gauge-invariant interaction terms for singlet, doublet and triplet representations [37]. In table 2.2 are listed all the possibilities, along with the respective quantum numbers under the gauge groups $SU(2)_L$ and $U(1)_Y$, and the Yukawa mixing terms in the Lagrangian.

After the Higgs develops its vacuum expectation value (vev), vector-like states can mix with SM quarks: the mixing occurs in the left-handed sector for the singlet and triplet representations and in the right-handed sector for the doublet representation. The mass eigenstates will henceforth be labelled as:

$$\left\{X_{5/3},\ T,\ B,\ Y_{-4/3}\right\}.$$

In this work the focus is on the vector-like quarks with SM-like charges, T and B, whose decays are listed in the next section (2.3.4). Further details on models with vector-like

	SM quarks	Singlets	Doublets	Triplets
	$\begin{pmatrix} u \\ d \end{pmatrix}\begin{pmatrix} c \\ s \end{pmatrix}\begin{pmatrix} t \\ b \end{pmatrix}$	$(T)\ (B)$	$\begin{pmatrix} X \\ T \end{pmatrix}\begin{pmatrix} T \\ B \end{pmatrix}\begin{pmatrix} B \\ Y \end{pmatrix}$	$\begin{pmatrix} X \\ T \\ B \end{pmatrix}\begin{pmatrix} T \\ B \\ Y \end{pmatrix}$
$SU(2)_L$	$q_L = 2$ $q_R = 1$	1	2	3
$U(1)_Y$	$q_L = 1/6$ $u_R = 2/3$ $d_R = -1/3$	$2/3 \quad -1/3$	$7/6 \quad 1/6 \quad -5/6$	$2/3 \quad -1/3$
$\mathcal{L}_Y$	$-y_u^i q_L^{-i} H^c u_R^i$ $-y_d^i q_L^{-i} V_{CKM}^{i,j} H\, d_R^j$	$-\lambda_u^i q_L^{-i} H^c T_R$ $-\lambda_d^i q_L^{-i} H\, B_R$	$-\lambda_u^i \psi_L^{-i} H^{(c)} u_R^i$ $-\lambda_d^i \psi_L^{-i} H^{(c)}\, d_R^j$	$-\lambda_i \bar{q}_L^i \tau^a H^{(c)} \psi_R^a$
$\mathcal{L}_m$	not allowed	$-M\bar{\psi}\psi$		

Table 2.2: Possible representations for vector-like quarks, with quantum numbers under $SU(2)_L$ and $U(1)_Y$ and Yukawa mixing terms in the Lagrangian, $\mathcal{L}_Y$. The Higgs boson is denoted as $H^{(c)}$ when it can be H or H^c, depending on the representation chosen. The gauge invariant mass term $\mathcal{L}_m$ common to all representations for VLQs is a striking feature of these new heavy quarks (table adapted from [11]).

quarks, in particular their electroweak interactions, described by new Lagrangians, can be found in [37].

2.3.4 VLQs Production and Decay

VLQs can be produced in the same way as SM quarks plus FCNCs channels. There can be pair production of vector-like quarks, dominated by QCD and sensitive to the new quarks masses; and also single production, characterized by electroweak contributions only, and sensitive to both the vector-like quark mass and its mixing parameters. At higher masses, single production mediated by the electroweak interactions could potentially dominate, depending on the strength of the interaction between the new quarks and the weak gauge bosons. The single production of vector-like quarks is highly model-dependent and experimentally there is still not enough sensitivity to study it [52], hence it will not be discussed.

Vector-like quarks can decay to SM particles, namely ordinary quarks plus a gauge or a Higgs boson. These decays occur through the mixing of these new quarks with the SM ones, hence modifying their couplings to the Z, W and Higgs boson. In general, the new quarks predicted in BSM models, such as Little Higgs and Composite Higgs, are expected to couple mainly to the third generation of SM quarks[9] (to the top and bottom quarks). Indeed, for generic Yukawa matrices and vector-like quark mass terms, it has been shown [35] that the mixing of these new heavy quarks is of order m/M, where m,

[9]For a more detailed discussion refer to [84].

M denote the masses of SM and new quarks, respectively. Furthermore, constraints on top couplings are weaker than for the other quarks [85, 86], i.e. there is more room for mixing also from the experimental side[10].

This mixing gives rise to two other important effects: it produces a modification of the couplings of the SM quarks (more precisely, of the lighter eigenstates), and allows for the single production of VLQs (the heavier eigenstates), which become the dominant production mechanism for high enough masses - current mass bounds from the LHC are around the region where single production dominates [38]. Indeed, vector-like quarks with masses up to $\sim 400-600$ GeV have been excluded by all experiments [11]. Indeed, the CMS Collaboration published a vector-like quark top search, setting lower mass limits in the range of $690-780$ GeV [1]. Furthermore, just recently, the ATLAS Collaboration published a vector-like quark search [3], in which results were used to set lower mass limits of 685 GeV and 755 GeV (at a 95% confidence level, C.L.) on vector like B quarks, when assuming the $SU(2)$ singlet and doublet hypotheses, respectively. Likewise, lower mass limits of 655 GeV and 735 GeV (at 95% C.L.) were obtained for vector-like T quarks when assuming the $SU(2)$ singlet and doublet hypotheses, respectively, depending on the assumptions for the branching ratios. Indeed, the limits derived are dependent on the branching ratios assumed, as seen in fig. 2.3.1, which presents the (observed) lower limits at 95% C.L. on the mass of vector-like T (a) and B (b) quarks for ATLAS searches with 14.3 fb^{-1} and 20.3 fb^{-1} of 8 TeV data. Mass exclusions are drawn sequentially for the different analyses in chronological order. For a given bin in the branching ratio (BR) plane, the strongest of all limits considered is shown (i.e. no combination is made of the different analyses, except for the $Ht+X$ and $Wb+X$ analyses for the T quark, which are combined). This figure considers all available limits on the vector-like T and B quarks derived by the ATLAS Collaboration [50, 88, 52]. The dependence of the derived limits on the branching ratios is verified in fig. 2.3.2 as well, which presents the observed lower limits at 95% C.L. on the mass of vector-like T (a) and B (b) quarks for the CMS Collaboration searches [1, 2] with 19.5 fb^{-1} and 19.6 fb^{-1} of 8 TeV data, respectively.

Once produced, the final state topology depends on the decay modes of the new quarks. Since the GIM mechanism ceases to operate for vector-like quarks, these can proceed at tree-level to a W, Z, or H boson plus a SM quark. Thus, fig. 2.3.3 depicts a T or a B vector-like quark, represented by Q, decaying to either an Standard Model t or b quark,

[10]However, in some models it is possible to avoid direct constraints and have large mixing with the lighter generations consistent with experimental data [87].

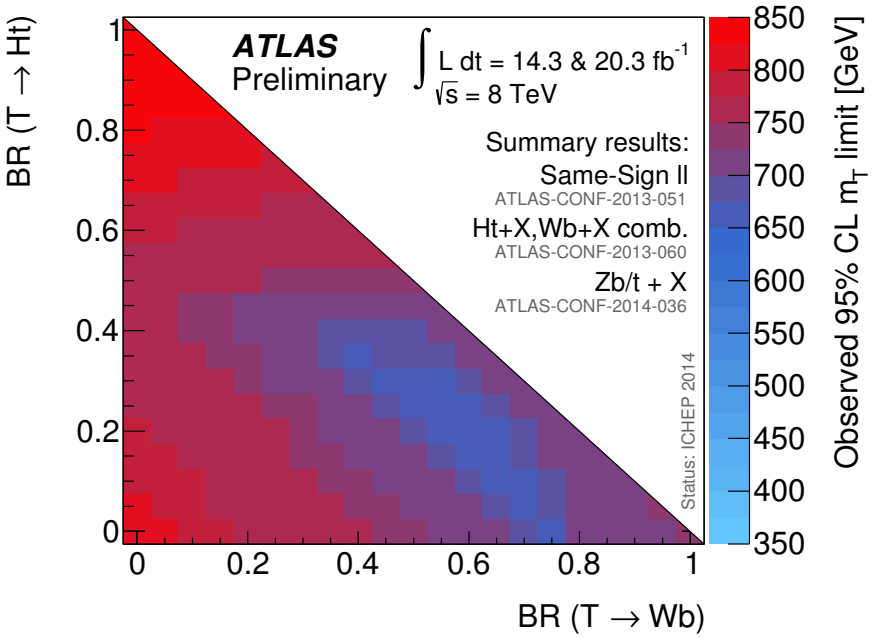

(a)

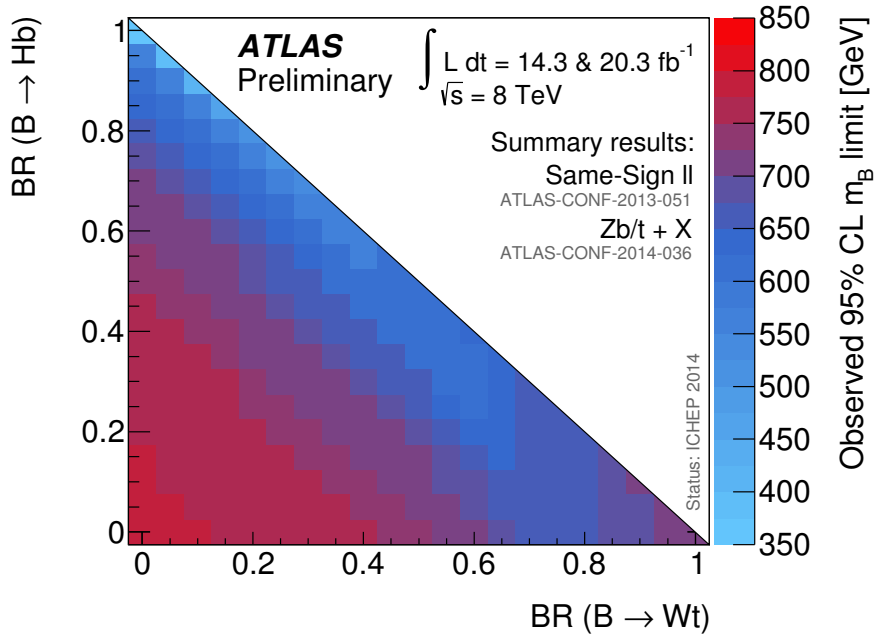

(b)

Figure 2.3.1: Observed lower limits at 95% C.L. on the mass of vector-like T (a) and B (b) quarks for ATLAS searches with 14.3 fb^{-1} and 20.3 fb^{-1} of 8 TeV data.

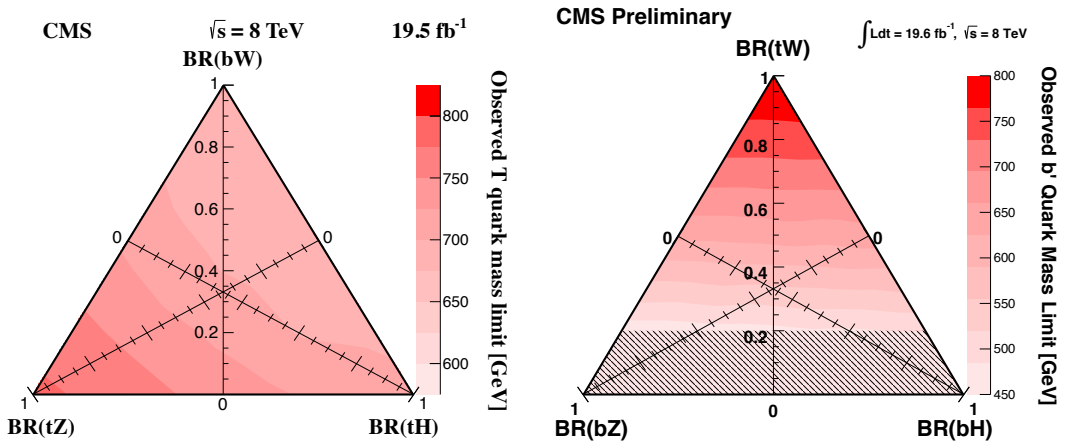

(a) (b)

Figure 2.3.2: Observed lower limits at 95% C.L. on the mass of vector-like T (a) and B (b) quarks for CMS searches with 19.5 fb^{-1} and with 19.6 fb^{-1} of 8 TeV data, respectively (extracted from [1, 2]).

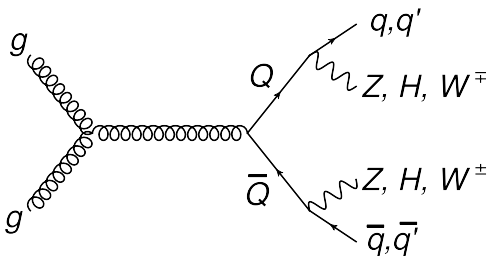

Figure 2.3.3: A representative diagram illustrating heavy quark pair production and vector-like decay modes (extracted from [3]).

represented by q or q', and a Z, H, or W boson.

This search considers pair production exclusively, and the cross sections are depicted in Fig. 2.3.4 as a function of the new quark mass, at $\sqrt{s} = 7$ TeV and $\sqrt{s} = 8$ TeV, dashed and solid lines, respectively.

This cross section prediction was computed with HATHOR v1.2 [4], an approximate next-to-next-to-leading-order (NNLO) calculation, using the MSTW2008 NNLO [89], at a 90% confidence level (C.L.), set of parton distribution functions (PDFs), and is independent of the electroweak quantum numbers of the new quark. The 8 TeV cross section ranges from ~ 5 pb for a quark mass of 350 GeV to ~ 10 fb for a quark mass of 850 GeV. Uncertainties have been calculated according to the MSTW prescription [90] and range from approximately 10 to 20% in the mass range considered in this analysis.

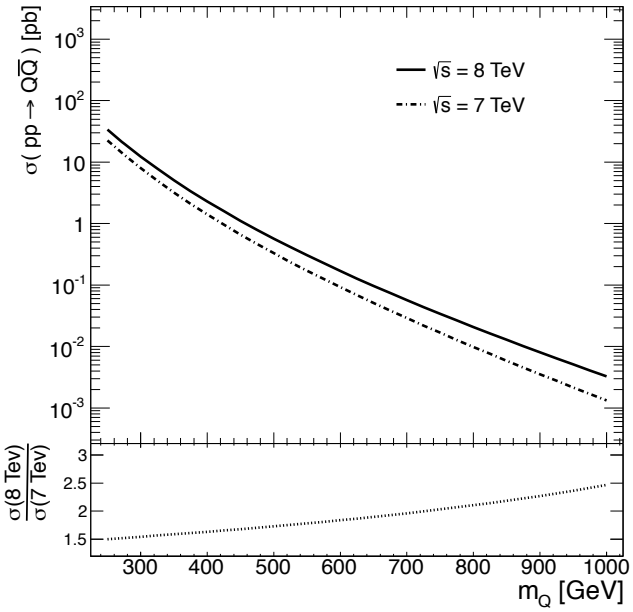

Figure 2.3.4: The pair production cross section versus quark mass as predicted by HATHOR [4] for pp collisions at $\sqrt{s} = 7$ TeV and 8 TeV. The bottom panel shows the 8 TeV/7 TeV cross section ratio (extracted from [5]).

For the VLQs with charges $\frac{2}{3}$ and $-\frac{1}{3}$, T and B respectively, whose pair production is the focus of this work, the possible decay channels are:

$$\begin{aligned} T &\to W^+b \quad T \to Zt, \quad T \to Ht \\ B &\to W^-t \quad B \to Zb \quad B \to Hb. \end{aligned} \tag{2.3.5}$$

The branching ratios, as computed by PROTOS v2.2 [37, 6], for these decay channels are plotted in fig. 2.3.5 as a function of the vector-like quarks T and B masses [11]. A weak-isospin ($SU(2)$) singlet T quark hypothesis is depicted in fig. 2.3.5 (a), as well as a T that is part of an $SU(2)$ doublet. The doublet prediction is valid for an (X, T) doublet, where the charge of the X quark is $+5/3$, as well as a (T, B) doublet when a mixing assumption of $V_{Tb} \ll V_{tB}$ is made [37]. The charged-current mode, $BR(T \to Wb)$, is absent in the doublet cases. Similarly, fig. 2.3.5 (b) shows the branching ratio of a B quark as a function of its mass for the singlet and doublet hypotheses. In the case of a (T, B) doublet, $BR(B \to Wt) = 1$. Branching ratio values are also presented in fig. 2.3.5 (b) for a (B, Y) doublet, where the charge of the Y quark is $-4/3$. The charged-current mode, $BR(B \to Wt)$, is absent in the (B, Y) doublet case.

[11] The branching ratios in fig. 2.3.5 are valid for small mixing between the new heavy quarks T and B and the third-generation quark t (top) and b (bottom).

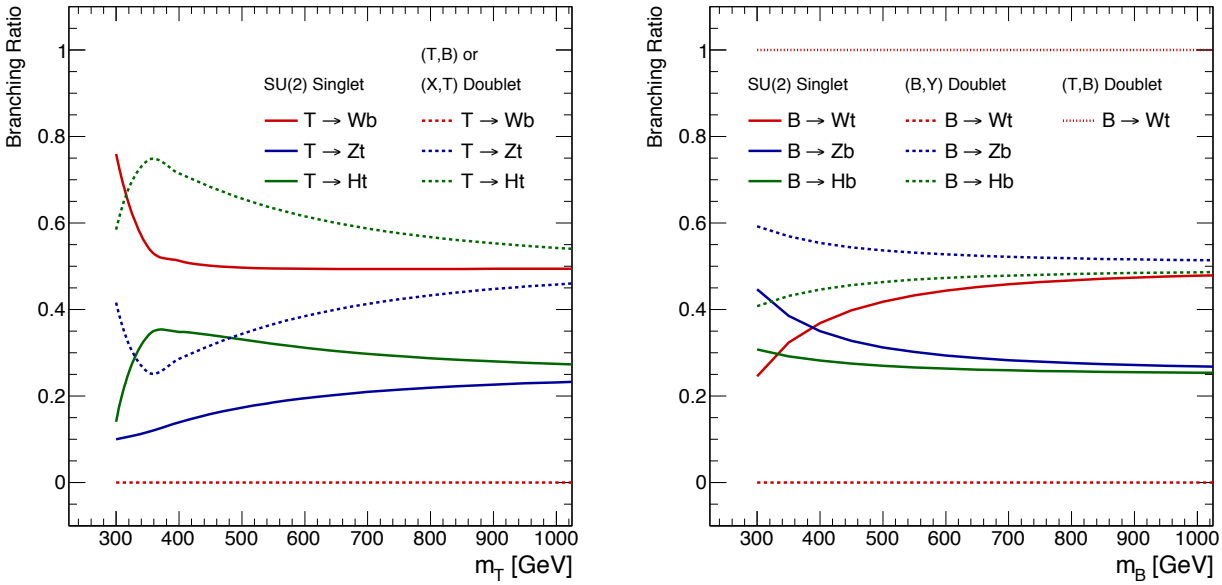

(a) (b)

Figure 2.3.5: Vector-like T quark branching ratios (a) to the Wb, Zt, and Ht decay modes as a function of the T quark mass, computed with PROTOS [6] for an $SU(2)$ singlet and two types of doublets. Likewise, vector-like B quark branching ratios (b) to the Wt, Zb, and Hb decay modes for a singlet and two types of doublets (extracted from [3]).

Despite the demanding environment of an hadron collider, such as the Large Hadron Collider (LHC), new heavy quark searches should be relatively clean, since these can be pair-produced through their gauge couplings to gluons (with a strength given by the strong coupling constant g_s) with a large cross section and, being rather heavy, their signals can be distinguished from the backgrounds.

3 Experimental Apparatus

In this chapter, the experimental infrastructure chain - the CERN laboratory (section 3.1), the Large Hadron Collider (LHC) (section 3.2), and the ATLAS detector (section 3.3) - is presented and briefly described. The functioning of the Worldwide LHC Computing Grid, in charge of the analysis of the LHC's output data, is outlined in section 3.4.

3.1 CERN

At the end of the Second World War, a handful of visionary scientists dreamed with the creation of an European atomic physics laboratory that would not only unite European scientists but also allow them to share the increasing costs of nuclear physics investigation. Among these enlightned pioneers were Raoul Dautry, Pierre Auger and Lew Kowarski in France, Edoardo Amaldi in Italy and Niels Bohr in Denmark. In 1952, eleven countries signed an agreement which established a provisional european council – the acronym CERN[1] was born. After some sessions of the provisional council, the CERN european laboratory was founded, in 1954, sitting astride the Franco-Swiss border near Geneva, and the exciting physics searches began!

CERN has come a long way since its foundation in 1954. It was one of Europe's first joint ventures and now has 21 member states. From the observation of the antideuteron in 1965[2], to the discovery of the W and Z bosons[3] - the weak interactions mediators -

[1] The name CERN is derived from the acronym for the French "Conseil Européen pour la Recherche Nucléaire", or European Council for Nuclear Research, a provisional body founded in 1952 with the goal of establishing a world-class fundamental physics research organization in Europe. At that time, the physics research program focused on understanding the inside of the atom, hence the word "nuclear".

[2] The antideuteron was observed simultaneously by two teams, one led by Antonino Zichichi using the Proton Synchrotron (PS) at CERN, and the other led by Leon Lederman, using the Alternating Gradient Synchrotron (AGS) accelerator at the Brookhaven National Laboratory, New York .

[3] Carlo Rubbia and Simon van der Meer were the key scientists behind this discovery, having received the Nobel Prize in physics only a year after the discovery. Rubbia instigated the conversion of the SPS accelerator into a proton-antiproton collider and was spokesperson of the UA1 experiment while Van der Meer designed the stochastic cooling technique [91] crucial to the collider's operation.

by the UA1 and UA2 (Underground Area 1 and 2) experiments at the SPS (Super Proton Synchrotron) in 1983, to the recent discovery (on the 4th July of 2012) of the long sought Higgs-consistent particle, with a mass around 126 GeV, by the ATLAS and CMS Collaborations at the Large Hadron Collider, the CERN laboratory is offering scientists and engineers all over the World the possibility to solve some of Nature's most intriguing mysteries, probing the fundamental structure of the Universe. In addition to plenty scientific discoveries, some of which listed above, several technological breakthroughs took place at CERN, such as the invention of the World Wide Web by Sir Tim Berners-Lee, and the recent establishment of the global computer network infrastructure Worldwide LHC Computing Grid, which is discussed in section 3.4.

3.2 Large Hadron Collider

At 10.28 am on 10 September 2008 a beam of protons was successfully steered around the 27-kilometre Large Hadron Collider (LHC) [92] for the first time. The Large Hadron Collider (LHC) at CERN extends the frontiers of particle physics with its unprecedented high energy and luminosity. It is the biggest and most powerful machine ever designed by mankind and was built in collaboration with over 10000 scientists and engineers from over 100 countries; lying in a tunnel 27 kilometres in circumference, at a depth ranging from 50 m to 175 m underground, beneath the Franco-Swiss border near Geneva, Switzerland. LHC's tunnel was previously the functioning grounds of its predecessor: the lepton-positron collider LEP (Large Electron-Positron Collider).

Inside the LHC, bunches of up to 10^{11} protons (p) collide 40 million times per second to provide several TeV proton-proton (pp) collisions at a design luminosity of $10^{34}\,\mathrm{cm}^{-2}\mathrm{s}^{-1}$. The LHC also collides heavy ions (A), in particular lead nuclei, at 5.5 TeV per nucleon pair, at a design luminosity of $10^{27}\,\mathrm{cm}^{-2}\mathrm{s}^{-1}$. The LHC is currently in shutdown, in order to upgrade the accelerator to its design center-of-mass energy, $\sqrt{s} = 14$ TeV, resuming operations in early 2015, with run II of data-taking.

The LHC contains two parallel beam pipes that intersect at four points, each containing a proton beam traveling in opposite directions around the circular tunnel. Each of the four collision points, depicted in fig. 3.2.1, correspond to one of the main LHC experiments: ATLAS (A Toroidal LHC ApparatuS), CMS (Compact Muon Solenoid), ALICE (A Large Ion Collider Experiment) and LHCb (Large Hadron Collider beauty).

The LHC comprises more than one thousand dipole magnets, each 14.3 meters long, to bend the beams in a circular trajectory, while an additional ~ 400 quadrupole magnets

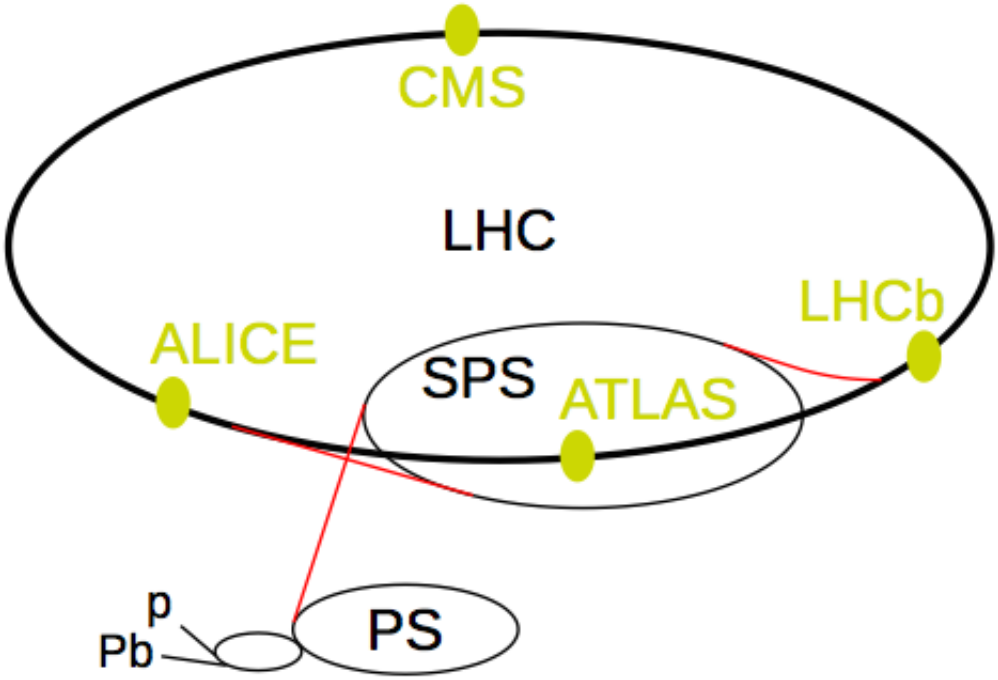

Figure 3.2.1: Scheme of the LHC experiments ATLAS, ALICE, CMS and LHCb; and preaccelerators PS (Proton Synchrotron) and SPS (Super Proton Synchrotron); figure extracted from [7].

are used to maintain the beams focused. These type-II superconducting magnets, made of copper-clad niobium-titanium (NbTi), operate at an average temperature of 1.9 K, kept by approximately 96 tonnes of superfluid liquid helium He-II.

The high interaction rates, radiation doses, particle multiplicities and energies, as well as the requirements for precision measurements that characterize the Large Hadron Collider, have definitely set new standards for the design of particle colliders.

3.3 ATLAS Detector

The ATLAS (A Toroidal LHC ApparatuS) detector [8] is a general purpose particle physics detector that probes pp collisions at the LHC, identifying and measuring the momentum and energy of the particles created. This detector is nominally forward-backward symmetric with respect to the interaction point, has a cilindrical geommetry covering a solid angle of $\sim 4\pi$, and consists of particle-tracking detectors (inner detector), electromagnetic and hadronic calorimeters, and a muon spectrometer. A cut-away view of the ATLAS detector is illustrated in fig. 3.3.2.

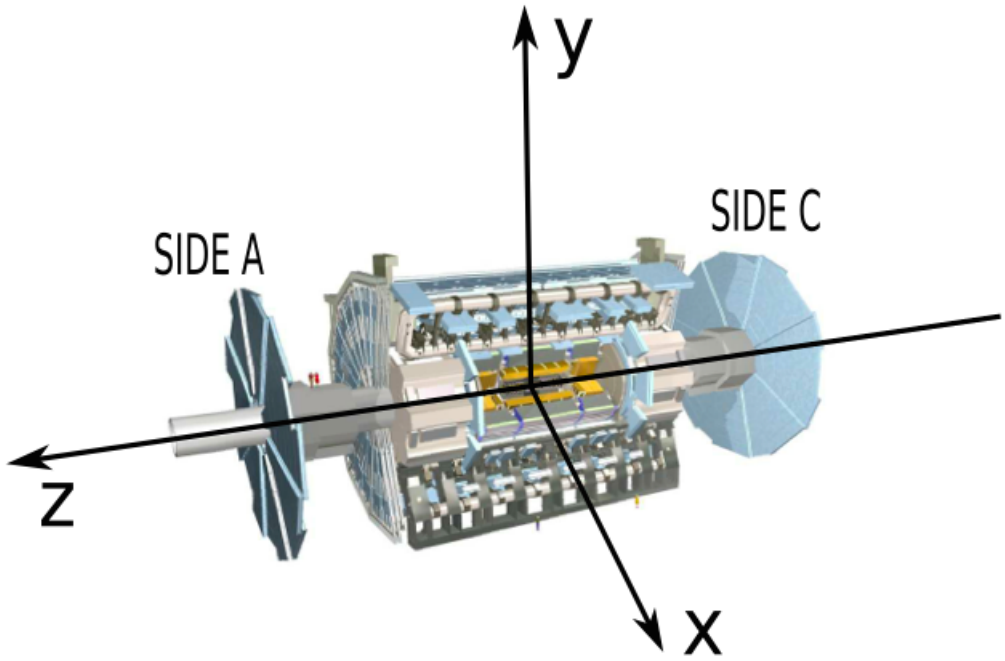

Figure 3.3.1: Representation of ATLAS coordinate system: the side-A of the detector is defined as the one with positive z and side-C as that with negative z. The azimuthal angle ϕ is measured around the beam axis, and the polar angle θ is measured from the beam axis (figure extracted from [7]).

ATLAS uses a right-handed coordinate system (fig. 3.3.1) with its origin at the nominal interaction point (IP) in the centre of the detector, and the z-axis along the beam line. The x-axis points from the IP to the centre of the LHC ring, and the y-axis points upwards.

Cylindrical coordinates (r, ϕ) are used in the transverse plane, ϕ being the azimuthal angle around the beam line. Observables labelled "transverse" are projected into the $x-y$ plane. The pseudorapidity is defined in terms of the polar angle θ as $\eta = -ln\, tan(\frac{\theta}{2})$ [4]. The transverse momentum p_T , the transverse energy E_T and the missing transverse energy E_T^{miss} are defined in the $x - y$ plane. The distance ΔR in the pseudorapidity-azimuthal angle space is defined as $\Delta R = \sqrt{\Delta\eta^2 + \Delta\phi^2}$.

At small radii transverse to the beamline, approximately 1000 particles will emerge from the collision point every 50 ns within $|\eta| < 2.5$, creating a very large track density in the inner detector [93]. To achieve the momentum and vertex resolution requirements

[4] In the case of massive objects such as jets, the rapidity $y = \frac{1}{2} ln\, [(E + p_z)/(E - p_z)]$ is sometimes used.

imposed by the benchmark physics processes, high-precision measurements must be made with fine detector granularity. Pixel and silicon microstrip (SCT) trackers, used in conjunction with gas-filled straw tubes of the Transition Radiation Tracker (TRT) for larger radii, offer these features. The ID (inner detector) is surrounded by a thin superconducting solenoid which provides a 2 T magnetic field, and by high-granularity liquid-argon (LAr) sampling electromagnetic calorimetry. The electromagnetic (EM) calorimeters employ lead absorbers and use liquid argon as the active medium. The barrel EM calorimeter covers $|\eta| < 1.5$ and the end-cap EM calorimeters $1.4 < |\eta| < 3.2$. While the electromagnetic calorimeter was designed to identify and measure the energy of the particles that interact through the electromagnetic force, the hadronic calorimeter absorbs the energy of particles that interact via the strong force, after crossing the electromagnetic calorimeter, i.e. the particle shower resulting from the hadronization of the quarks (also known as jet). Hadronic calorimetry in the region $|\eta| < 1.7$ is achieved using steel absorbers and scintillating tiles as the active medium. Liquid argon calorimetry with copper absorbers is employed in the hadronic end-cap calorimeters, which cover the region $1.5 < |\eta| < 3.2$. Forward liquid argon calorimeters employing copper and tungsten absorbers cover the region $3.1 < |\eta| < 4.9$. The muon spectrometer measures the deflection of muons with $|\eta| < 2.7$ using multiple layers of high-precision tracking chambers located in a toroidal field of approximately 0.5 T and 1 T in the central and end-cap regions, respectively. The muon spectrometer is also instrumented with separate trigger chambers covering $|\eta| < 2.4$.

ATLAS makes use of a trigger system with three distinct levels: L1, L2 and the event filter. Each trigger level refines the decisions made at the previous level, applying additional selection criteria if necessary. The L1 trigger searches for high transverse-momentum muons, electrons, photons, jets, and $\tau -$ leptons decaying into hadrons, as well as large missing and total transverse energy. In each event, the first-level trigger also defines Regions-of-Interest (RoI's), recording sets of coordinates in η and ϕ of these RoI's within the detector. The RoI data include information on the type of feature identified and the criteria passed, e.g. a threshold. This information is subsequently used by the high-level trigger. L1 is implemented in custom electronics, using a subset of the detector information to reduce the event rate to a design value of 75 kHz. The second-level trigger selection is seeded by the RoI information provided by the L1 trigger over a dedicated data path. L2 selections use all the available detector data within the RoI's (approximately 2% of the total event data), decreasing the trigger rate to approximately 3.5 kHz. The last step of the event selection is performed by the event filter, which

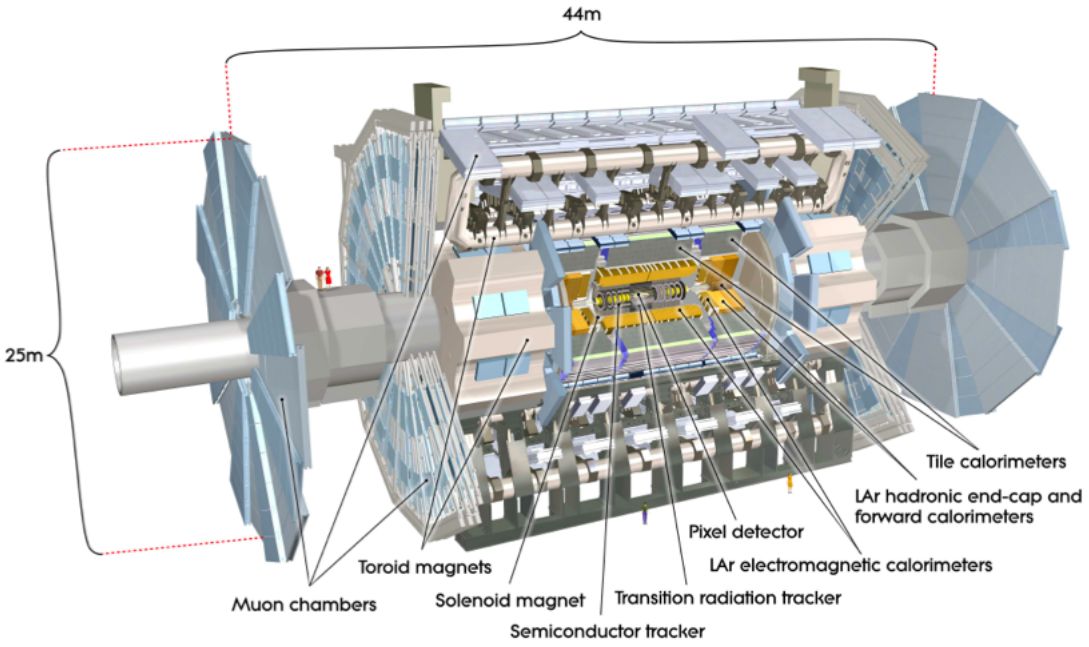

Figure 3.3.2: Cut-away view of the ATLAS detector. The dimensions of the detector are 25 m in height and 44 m in length. The overall weight of the detector is approximately 7000 tonnes (figure extracted from [8]).

reduces the event rate to approximately 200 Hz.

The general performance goals for the ATLAS detector are summarized in table 3.1.

3.4 Worldwide LHC Computing Grid

The Worldwide LHC Computing Grid (WLCG) project is a global network of more than 170 computing centres in 40 countries, linking up national and international grid infrastructures and designed to analyze the $\sim$ 30 Petabytes (30 million Gigabytes) of data annually generated at the LHC [94]. The data from the LHC experiments is distributed around the globe, according to a four-tiered model. Data coming from the experiment data acquisition systems is written to tape in the CERN Tier-0 facility, and a second copy of the raw data is simultaneously provided to the Tier-1 centers, in Europe, Asia, and North America, via dedicated 10 Gb/s links. Subsequently, the Tier-1 centers make data available to more than 150 Tier-2 centers, each consisting of one or several collaborating computing facilities able to store enough data and provide adequate computing power for the required analysis tasks.

Individual scientists can access and further process the data through Tier-3 computing

Detector component	Required resolution	η coverage	
		Measurement	Trigger
Tracking	$\sigma_{p_T}/p_T = 0.05\% \times p_T \oplus 1\%$	$\lvert\eta\rvert < 2.5$	–
EM calorimetry	$\sigma_E/E = 10\%/\sqrt{E} \oplus 0.7\%$	$\lvert\eta\rvert < 3.2$	$\lvert\eta\rvert < 2.5$
Hadronic calorimetry (jets)			
Barrel and end-cap	$\sigma_E/E = 50\%/\sqrt{E} \oplus 3\%$	$\lvert\eta\rvert < 3.2$	$\lvert\eta\rvert < 3.2$
Forward	$\sigma_E/E = 100\%/\sqrt{E} \oplus 10\%$	$3.1 < \lvert\eta\rvert < 4.9$	$3.1 < \lvert\eta\rvert < 4.9$
Muon spectrometer	$\sigma_{p_T}/p_T = 10\%$ at $p_T = 1$ TeV	$\lvert\eta\rvert < 2.7$	$\lvert\eta\rvert < 2.4$

Table 3.1: General performance goals of the ATLAS detector (extracted from [8, 12]). For high-p_T muons, the muon spectrometer performance is independent of the inner-detector system. The unit employed for E and p_T is GeV.

resources, which consist of local clusters. As an example of the data-processing chain, the analysis of the data presented in this dissertation involved the CERN Tier-0 facility (the origin of the raw data), the processing of LHC data at the PIC (Barcelona) Tier-1 center, local facilities in Coimbra and Lisbon (Portuguese ATLAS group Tier-2) and the cluster at Universidade do Minho (Braga), a Tier-3 facility.

4 Building the Analysis: $T \to Zt$ and $B \to Zb$

This chapter is devoted to the construction of the analysis, starting with the review of the results recently published by the ATLAS Collaboration [3]. This search analysis is focused on the pair production of new heavy quarks that decay to a Z boson and a third generation Standard Model quark. In the case of a new charge $+2/3$ quark (T), the decay targeted is $T \to Zt$, while the decay targeted for a new charge $-1/3$ quark (B) is $B \to Zb$. A dileptonic topology was considered, with exactly 2 leptons, in which a pair of charged leptons has an invariant mass compatible with the decay of a Z gauge boson, and in which at least 2 jets are classified as coming from a $b-$quark (b-tagged jets). In the final stages of the event selection is required a high-p_T Z boson and a high value of H_T(jets)[1].

4.1 Data Sample

The data analysed in this search were collected with the ATLAS detector, at the CERN Large Hadron Collider, between April and December of 2012 during LHC proton-proton (pp) collisions at $\sqrt{s} = 8$ TeV and correspond to an integrated luminosity of 20.3 ± 0.6 fb^{-1} [93]. Figure 4.1.1 illustrates the total integrated luminosity as a function of time, in 2011 and 2012.

Fig. 4.1.2 illustrates the luminosity-weighted distribution of the mean number of interactions per bunch crossing for 2012 (full pp collisions dataset). The mean value of μ here is $< \mu >= 20.7$, and corresponds to the mean of the Poisson distribution on the number of interactions per crossing for each bunch. It is calculated from the instantaneous luminosity per bunch as $\mu = (L_{bunch} \times \sigma_{inel}) \,/\, (n_{bunch} \times f_r)$, where L_{bunch} is the instantaneous luminosity per bunch, σ_{inel} is the inelastic cross section which is

[1]The H_T(jets) is defined as the scalar sum of the transverse momenta, $\sum p_T$, of all the jets.

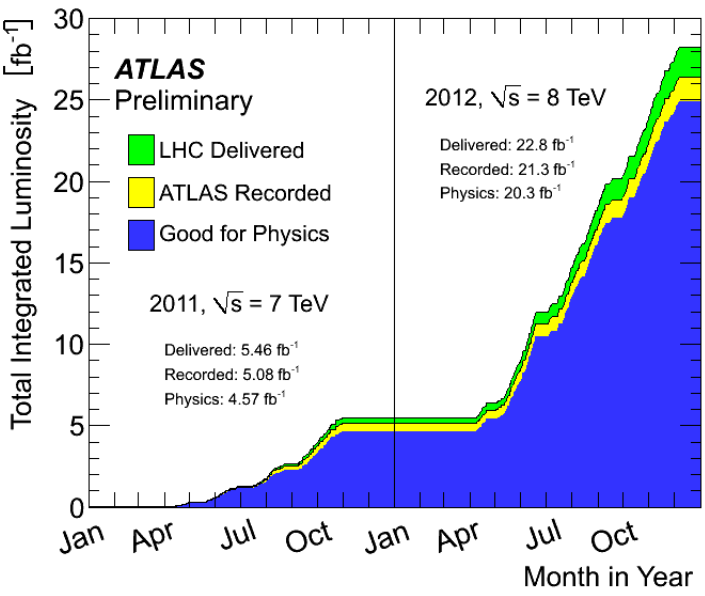

Figure 4.1.1: The cumulative luminosity delivered (green) versus time, recorded by ATLAS (yellow), and certified to be good quality data (blue) during stable beams and for pp collisions at 7 and 8 TeV centre-of-mass energy in 2011 and 2012.

taken to be 73 mb, n_{bunch} is the number of colliding bunches and f_r is the LHC operating revolution frequency. Refer to [95] for a more detailed explanation.

4.2 Trigger

Events recorded by single electron or muon triggers under stable beam conditions and for which all detector subsystems were operational are considered. Single lepton triggers with different p_T thresholds are combined to increase the overall efficiency. The p_T thresholds implemented are 24 and 60 GeV for electron-triggers and 24 and 36 GeV for muon-triggers. The lower threshold triggers include isolation requirements on the candidate leptons, resulting in inefficiencies at higher p_T that are recovered by the higher p_T threshold triggers. The trigger isolation criteria are looser or identical than the requirements placed on the final reconstructed electrons and muons. Events satisfying the trigger requirements must also have a reconstructed vertex with at least five associated tracks, consistent with the beam collision region in the $x-y$ plane. If more than one such vertex is found, the primary vertex selected is the one with the largest sum of the squared p_T of its associated tracks. The events selected for this analysis contain exactly one pair

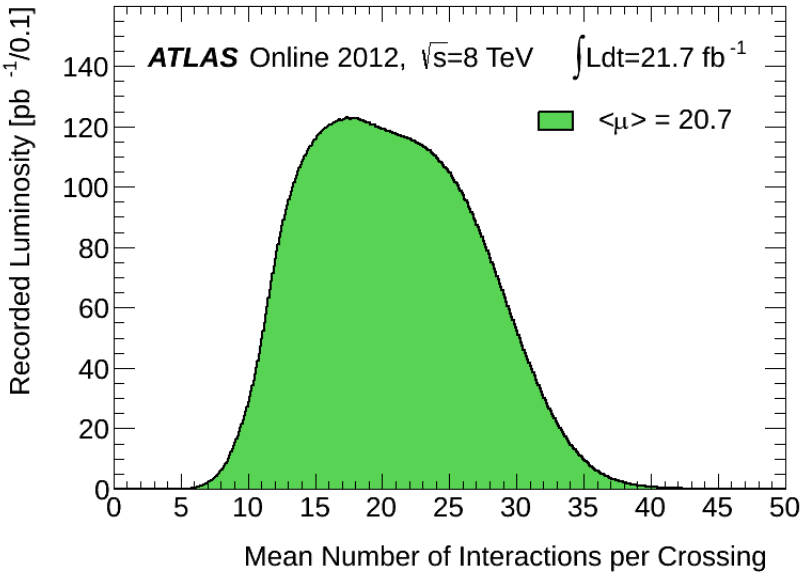

Figure 4.1.2: Luminosity-weighted distribution of the mean number of interactions per crossing for 2012; full pp collisions dataset.

of same flavor reconstructed leptons (electrons or muons) with opposite electric charge - dilepton topology - allowing for the reconstruction of a Z boson candidate. At least one reconstructed lepton in an event must match ($\Delta R < 0.15$) a lepton reconstructed by the high-level trigger.

4.3 Presenting Primary Physics Objects

The primary physics objects used in this search are electrons, muons, and hadronic jets, including jets that have been tagged for the presence of a b-hadron, known as b-tagged jets. A summary of the reconstruction methods and identification criteria applied to each of the aforementioned physics objects is given below, largely based on [3].

Electron candidates [96] are reconstructed from energy deposits (know as clusters) in the electromagnetic calorimeter that are matched to corresponding reconstructed tracks in the silicon tracker (inner detector). The candidates are required to have a transverse energy, E_T, greater than 25 GeV and $|\eta_{\text{cluster}}| < 2.47$ (where $|\eta_{\text{cluster}}|$ is the pseudorapidity of the cluster associated with the electron candidate). Candidates in the transition region between the barrel and end-cap calorimeters, $1.37 < |\eta_{\text{cluster}}| < 1.52$, are excluded. The longitudinal impact parameter of the electron track with respect to the selected primary vertex of the event is required to be less than 2 mm. Electron

candidates used to reconstruct Z boson candidates satisfy medium quality requirements [96] on the EM cluster and associated track.

Muon candidates [97] are reconstructed from track segments in the various layers of the muon spectrometer system that are matched to corresponding reconstructed tracks in the silicon tracker (inner detector). The final candidates are refitted using the complete track information from both detector systems. Muon candidates are required to satisfy $p_T > 25$ GeV and $|\eta| < 2.5$. The hit pattern in the inner detector must be consistent with a well-reconstructed track, and the longitudinal impact parameter of the muon track with respect to the selected primary vertex of the event is required to be less than 2 mm. Muons must also satisfy a p_T-dependent track isolation requirement: the scalar sum of the track p_T in a cone of variable radius $\Delta R < 10\,\text{GeV}/p_T^{\mu}$ around the muon (excluding the muon itself) must be less than 5% of the muon p_T.

Jets are reconstructed using the anti-k_t algorithm [98, 99, 100] with a radius parameter $R = 0.4$ from calibrated topological clusters built from energy deposits in the calorimeters. Prior to jet finding, a local cluster calibration scheme [101] is applied to correct the topological cluster energy for the effects of non-compensation, dead material, and out-of-cluster leakage. The corrections are obtained from simulation of charged and neutral particles. After energy calibration [102], jets are required to satisfy $p_T > 25$ GeV and $|\eta| < 2.5$. To reduce selected jets that originate from secondary pp interactions, a requirement on a variable referred to as the "jet vertex fraction" (JVF) is made. The requirement ensures that at least 50% of the sum of the transversa momenta of tracks with $p_T > 0.5$ GeV associated with a jet comes from tracks compatible with originating from the primary vertex. During jet reconstruction, no distinction is made between identified electron and jet energy deposits. Hence, if any selected jet is within $\Delta R < 0.2$ of a selected electron, the jet is excluded to avoid double-counting of electrons as jets. Subsequently, any electrons or muons within $\Delta R < 0.4$ of the axis of selected jets are discarded.

One of the most successful methods for identifying b-jets relies on the fact that these nearly always contain a fast-moving B-hadron. Such particles are characterized by decays to many-particle final states, with lifetimes of about 10^{-12} s. Hence b-jets typically contain multiprong decay vertices close to the production vertex - an unique feature that other jets do not share. In this study, for the identification of $b-$tagged jets is used the MV1 algorithm [103], which employs an artifical neural network, combining information from the impact parameters of displaced tracks, as well as topological properties of secondary and tertiary decay vertices reconstructed within the jet. Fig. 4.3.1 shows

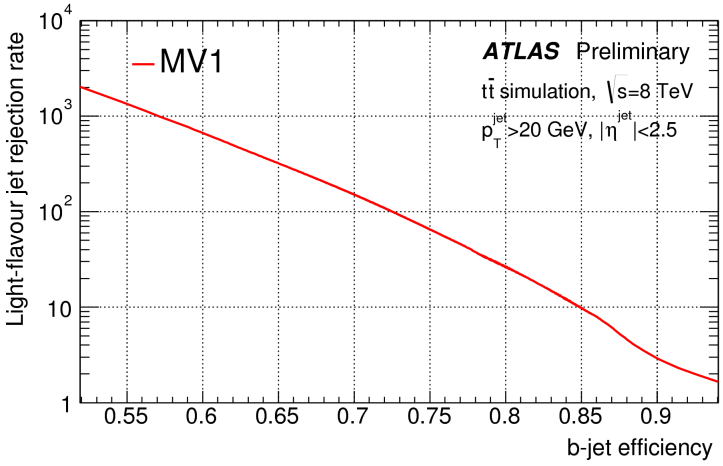

Figure 4.3.1: Performance (light-flavour rejection versus b-jet efficiency) of the MV1 tagging algorithm, as evaluated for jets with $p_T > 20$ GeV and $|\eta| < 2.5$ in a sample of simulated $t\bar{t}$ events (extracted from [9]).

the performance of the MV1 tagging algorithm evaluated for a $t\bar{t}$ sample produced using Powheg interfaced to Pythia 6 [104] with the Perugia 2011C tune [105], and CT10 parton density functions (PDFs) [106]. The performance of the MV1 algorithm has been calibrated at working points corresponding to efficiencies of 60%, 70% and 80%. In this study, the working point used corresponds to a 70% efficiency to tag a b-quark, with a light-jet rejection factor of ~ 130 and a charm jet rejection factor of 5, as determined for b-tagged jets satisfying $p_T > 20$ GeV and $|\eta| < 2.5$ in simulated $t\bar{t}$ events. The efficiency of the MV1 algorithm to tag b, c, and light-flavour jets as b-tagged, for this working point, is shown in Fig. 4.3.2, as a function of jet p_T and η, respectively.

4.4 Signal Modeling

Monte Carlo (MC) simulated samples of leading-order (LO) pair-production events were generated for the $T\bar{T}$ and $B\bar{B}$ hypotheses with PROTOS v2.2 interfaced with PYTHIA [104] v6.421, and using the MSTW 2008 LO [89] set of parton distribution functions (PDFs). These samples are normalized using the TOP++ cross-section predictions. The vector-like quarks decay with a branching ratio of 1/3 to each of the three modes (W, Z, H). Arbitrary sets of branching ratios consistent with the three modes summing to unity are obtained by reweighting the samples using particle-level information. A Standard Model Higgs boson with a mass of 125 GeV is assumed. The primary set of samples includes quark masses between 350 GeV and 850 GeV in steps of 50 GeV

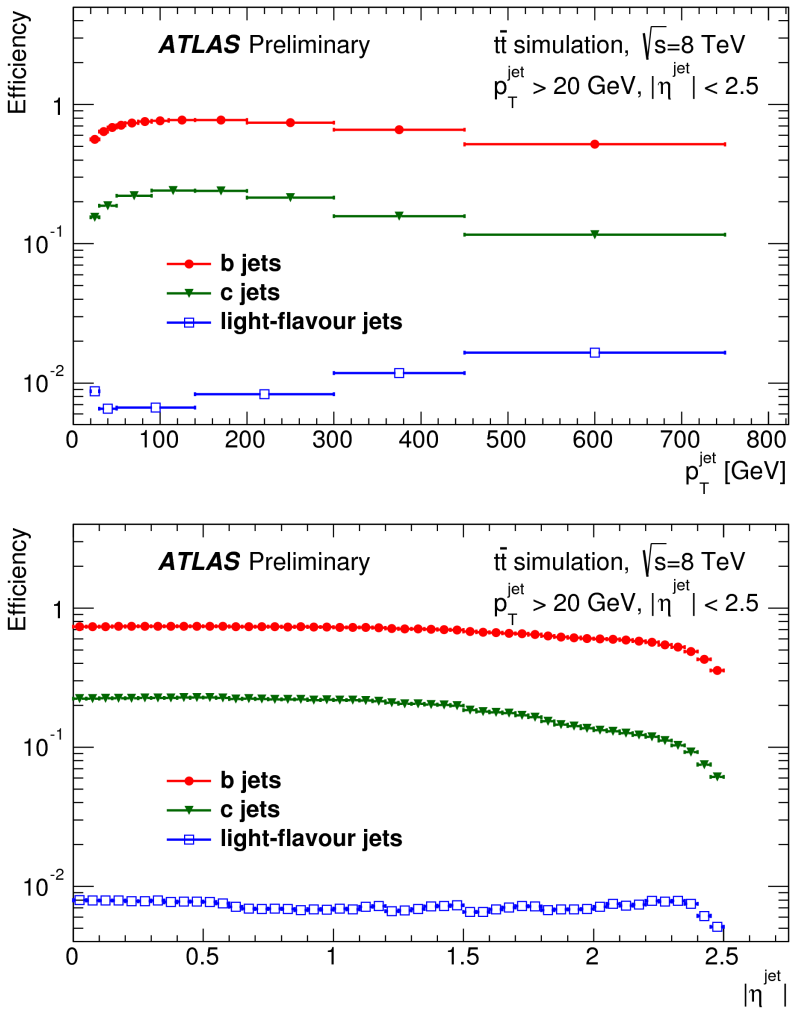

Figure 4.3.2: Efficiency of the MV1 tagger to select b, c, and light-flavour jets, as a function of jet p_T (upper plot) and $|\eta|$ (lower plot). The weight selection on the MV1 output discriminant is chosen to be 70% efficient for b-jets with $p_T > 20$ GeV and $|\eta| < 2.5$, as evaluated on a sample of simulated $t\bar{t}$ events (extracted from [9]).

and implement $SU(2)$ singlet couplings. Additional samples were produced at two mass points - 350 GeV and 600 GeV - using $SU(2)$ doublet couplings, in order to confirm that kinematic differences resulting from the different chirality of singlet and doublet couplings are negligible in this analysis. The aforementioned samples were passed through a fast detector simulation [107], while additional samples with quark masses of 400 GeV, 600 GeV, and 800 GeV were also produced using full detector simulation [108] based on GEANT v4 [109] to test the agreement. All signal samples were filtered at the generator level to require the presence of at least one lepton (electron or muon) with $p_T > 10$ GeV and $|\eta| < 2.8$.

4.5 Background Modeling

The SM backgrounds in this analysis are predicted primarily with simulated samples normalized to next-to-leading order or higher cross section calculations. The cross-section normalization is set by the NNLO prediction calculated with the DYNNLO program [110]. The leading-order multi-parton event generator SHERPA [111] was used to produce Z+jets samples, using v1.4.1 with the CT10 [106] PDF set, and generated setting the charm and bottom quarks to be massive. Filters are used to divide the samples into events containing a bottom hadron, events without a bottom hadron but containing a charm hadron, and events with neither of these hadrons. To increase the statistical precision of the prediction of events with large Z boson transverse momentum, $p_T(Z)$, each hadron filtered sample is produced in different $p_T(Z)$ intervals: inclusive, 70−140 GeV, 140−280 GeV, 280−500 GeV, and $>$ 500 GeV. Samples in the first three ranges are reconstructed with a fast detector simulation while the latter two use full detector simulation.

After SM Z+jets processes, the pair production of top quarks ($t\bar{t}$) is the next most relevant background source at the final stages of event selection. The $t\bar{t}$ cross section for pp collisions at a centre-of-mass energy of $\sqrt{s} = 8$ TeV is $\sigma_{t\bar{t}} = 253^{+13}_{-15}$ pb for a top quark mass of 172.5 GeV. It has been calculated at next-to-next-to leading order (NNLO) in QCD including resummation of next-to-next-to-leading logarithmic (NNLL) soft gluon terms with TOP++2.0 [112, 113, 114, 115, 116, 117, 118]. The PDF and α_S uncertainties were calculated using the PDF4LHC prescription [119] with the MSTW2008 68% CL NNLO [89, 90], CT10 NNLO [106, 120] and NNPDF2.3 5f FFN [121] PDF sets, added in quadrature to the scale uncertainty.

Simulated $t\bar{t}$ events are produced using POWHEG [122] for the matrix element with

the CT10 PDF set. Parton shower and hadronization are performed with PYTHIA. The other small Standard Model background processes modeled with simulation include diboson, single top, $t\bar{t}+W/Z$, and W+jets processes. The diboson processes (WW, WZ and ZZ) are simulated with ALPGEN [123], another leading-order multi-parton event generator, interfaced to HERWIG [124] for parton shower and hadronization, and normalized to NLO cross section predictions [125].

Samples generated with MC@NLO [126] interfaced to HERWIG are used to estimate the Wt and $s-$channel single top processes, while ACERMC [127] interfaced to PYTHIA is used to estimate the t-channel process. The single top processes are normalized to NLO cross sections [128]. The $t\bar{t}$+W/Z processes are generated with MADGRAPH [129], with parton shower and hadronization performed with PYTHIA, and also normalized to NLO cross sections [130]. For the production method of the W+jets samples refer to [3]. The multi-jet background is estimated using data samples satisfying the nominal trigger requirements but enriched in fake leptons obtained by requiring that both leptons fail the standard identification requirements. Other requirements are applied to reduce Drell-Yan and $t\bar{t}$ contamination. The multi-jet estimate is then obtained by applying the same kinematic selection to these samples as the nominal data sample with a normalization determined at the preselection level to account for the difference between data and all other backgrounds in the dilepton mass region between 50 and 75 GeV. In both the ee and $\mu\mu$ channels, the difference is comparable or smaller than the uncertainty on all other backgrounds. No multi-jet events are predicted to pass the final event selection, but the estimate in the earlier stages of the analysis has a small influence on the data-driven Z+jets corrections, which was found to be negligible [3].

4.6 Search Strategy and Event Selection

At a first selection level is required that events contain a Z boson candidate and at least 2 jets ($Z+ \geq 2$ jets). Z boson candidates are formed if the invariant mass of same flavor and opposite charge lepton pairs (electron or muon)[2] differs from the known value for the Z boson mass ($\sim$ 91 GeV [65]) by less than 10 GeV (Z candidate invariant mass window).

In order to better understand the selection cuts applied in the analysis, unit-normalized distributions of simulated signal and background events are presented in fig. 4.6.1, where

[2]One of the Z boson decay channels is $Z \to l\bar{l}$, where l stands for lepton. In this work l stands only for electrons or muons.

	$Z+ \geq 2$ jets	≥ 2 b-jets	$p_T(Z) > 150$ GeV	$H_T(\text{jets}) > 600$ GeV
$T\overline{T}_S$	22.2 ± 0.4	12.1 ± 0.3	10.0 ± 0.3	8.5 ± 0.2
$B\overline{B}_S$	36.7 ± 0.6	18.7 ± 0.4	16.5 ± 0.4	14.2 ± 0.3
$Z +$ light	281776.3 ± 1747.3	298.8 ± 128.8	5.6 ± 1.0	0.1 ± 0.1
$Z +$ charm	207629.1 ± 611.6	598.1 ± 30.8	57.6 ± 3.2	3.9 ± 0.6
$Z +$ bottom	55372.6 ± 104.7	4420.1 ± 27.7	380.8 ± 4.8	19.4 ± 1.0
$t\bar{t}$	5982.1 ± 42.6	2185.5 ± 25.4	33.1 ± 3.2	4.6 ± 1.2
Other background	8643.9 ± 29.4	274.3 ± 6.3	41.5 ± 1.7	4.0 ± 0.5
Total background	559403.9 ± 1854.9	7776.9 ± 137.8	518.6 ± 6.9	32.1 ± 1.7
Data	560131	7790	542	31

Table 4.1: Listed are the predicted and observed number of events ($ee+\mu\mu$ channel), and the statistical uncertainties associated, after the indicated selection levels, for reference $B\overline{B}_S$ and $T\overline{T}_S$ signal yields assuming $m_{B/T} = 650$ GeV and $SU(2)$ singlet branching ratios. SM backgrounds yields are listed by category, as well as the combined total. The events for the rightmost three selection levels contain at least two b-tagged jets (signal region).

panels (a) and (b) display the jet and b-tagged jet multiplicity, and panels (c) and (d) present the $p_T(Z)$ and $H_T(\text{jets})$ distributions, before applying a selection cut based on each of them, respectively.

The following remarks apply to all the distributions shown throughout this chapter: the reference signals displayed correspond to $B\overline{B}$ and $T\overline{T}$ production assuming $SU(2)$ singlet quarks with a mass of 650 GeV. The hatched bands in the upper and lower panels represent the total background uncertainty; the leftmost bin in each histogram contains underflow events, and the rightmost bin contains overflow events. The kinematic distributions for the leptons and the Z boson candidate are plotted in figs. 4.6.2-4.6.3 and figs. 4.6.4-4.6.5. In fig. 4.6.6 is presented the b-tagged jets multiplicity.

In table 4.1 is listed the predicted and observed number of events ($ee + \mu\mu$ channel) for the cut-flow implemented in this study, for reference $B\overline{B}_S$ and $T\overline{T}_S$ signal yields assuming $m_{B/T} = 650$ GeV and $SU(2)$ singlet branching ratios. SM backgrounds yields are listed by category, as well as the combined total. All the values in the table must coincide with the ones in the upper captions of the distributions at the same selection level, concerning the number of signal, background and data events, to ensure the consistency of our study.

Events passing the $Z+ \geq 2$ jets selection are then separated according to the number of b-tagged jets in the event (N_{tag}). Vector-like quark pair-production signal events are expected to yield at least two b-jets ($N_{tag} \geq 2$), whether produced directly from a heavy

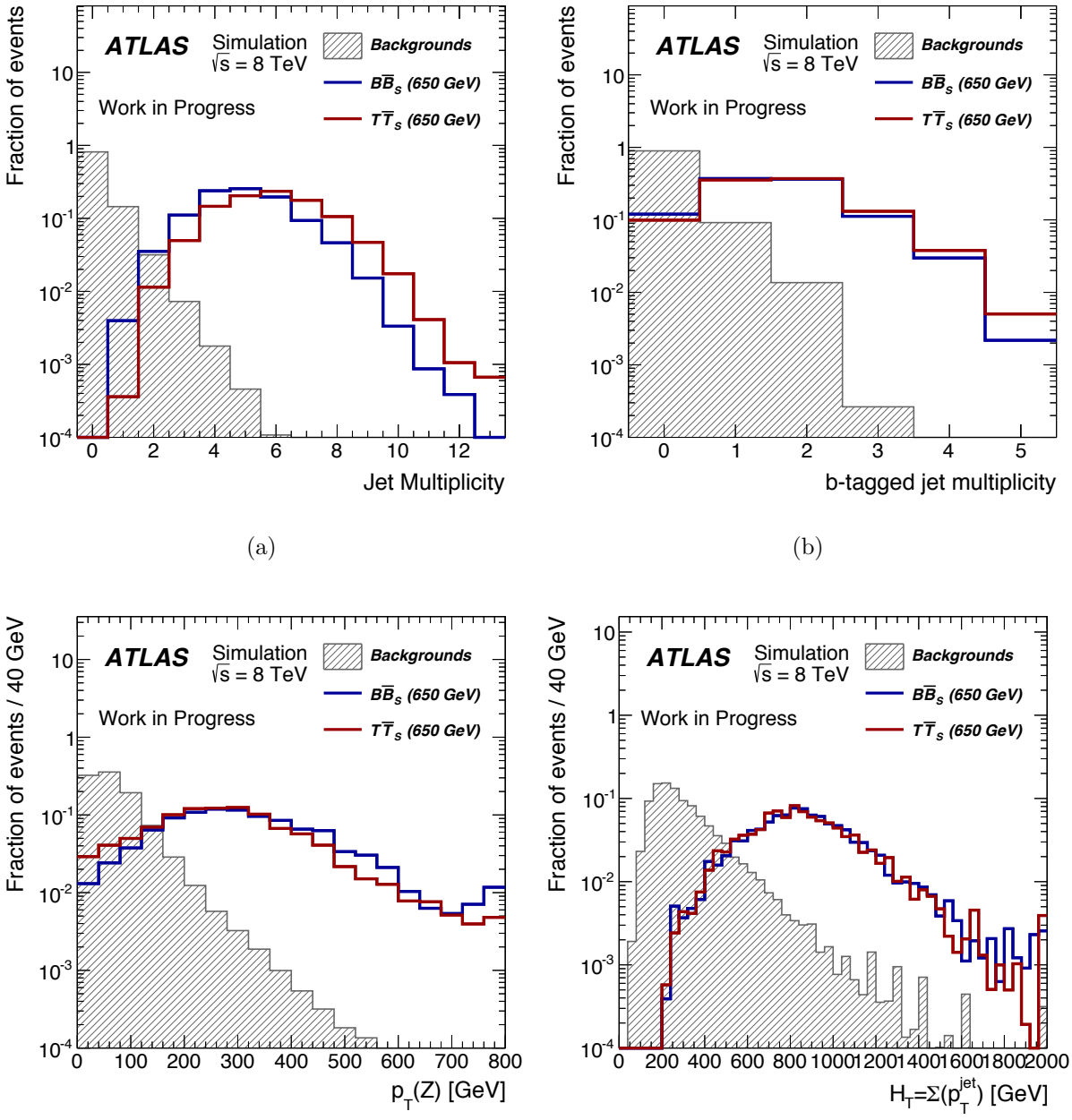

(a) (b)

(c) (d)

Figure 4.6.1: Unit-normalized distributions in the $ee+\mu\mu$ channel. Panel (a) displays the jet multiplicity, before requiring for 2 jets (after only requiring a Z boson candidate); panel (b) presents the b-tagged jets multiplicity, before requiring for two b-tagged jets (after a $Z+\geq 2$ jets selection); panels (c) and (d) present the $p_T(Z)$ and H_T(jets) distributions, before a $p_T(Z) > 150$ GeV and H_T(jets) > 600 GeV selection, respectively. The filled histogram corresponds to SM backgrounds, while the red and blue solid lines correspond to the $T\bar{T}$ and $B\bar{B}$ signal, respectively, assuming a heavy quark mass of 650 GeV with vector-like singlet branching ratios.

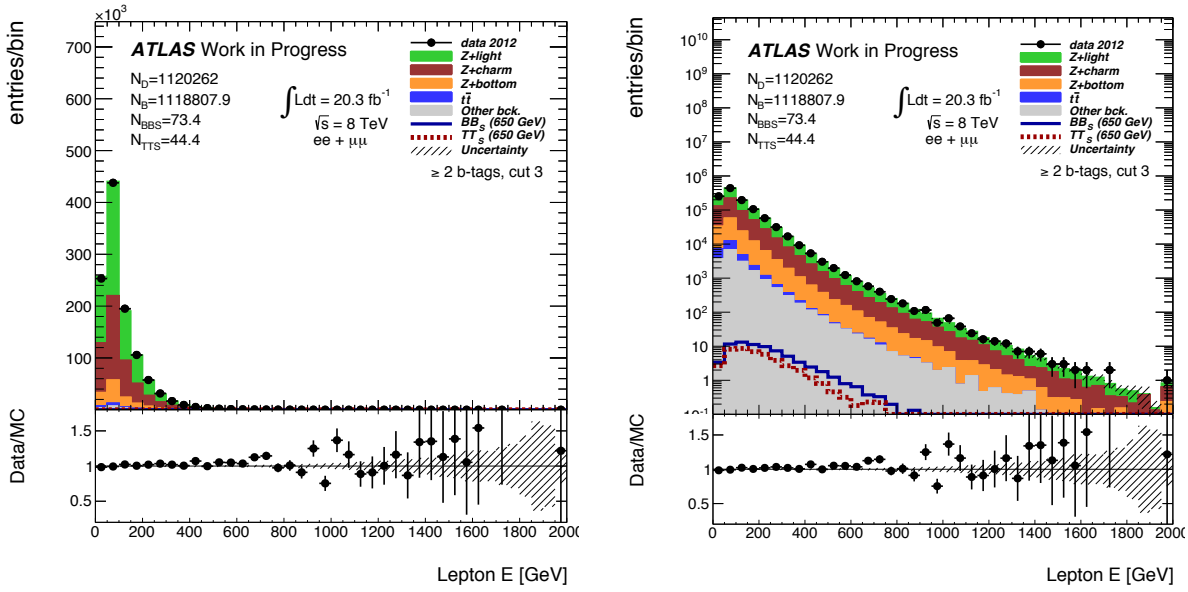

(a)

(b)

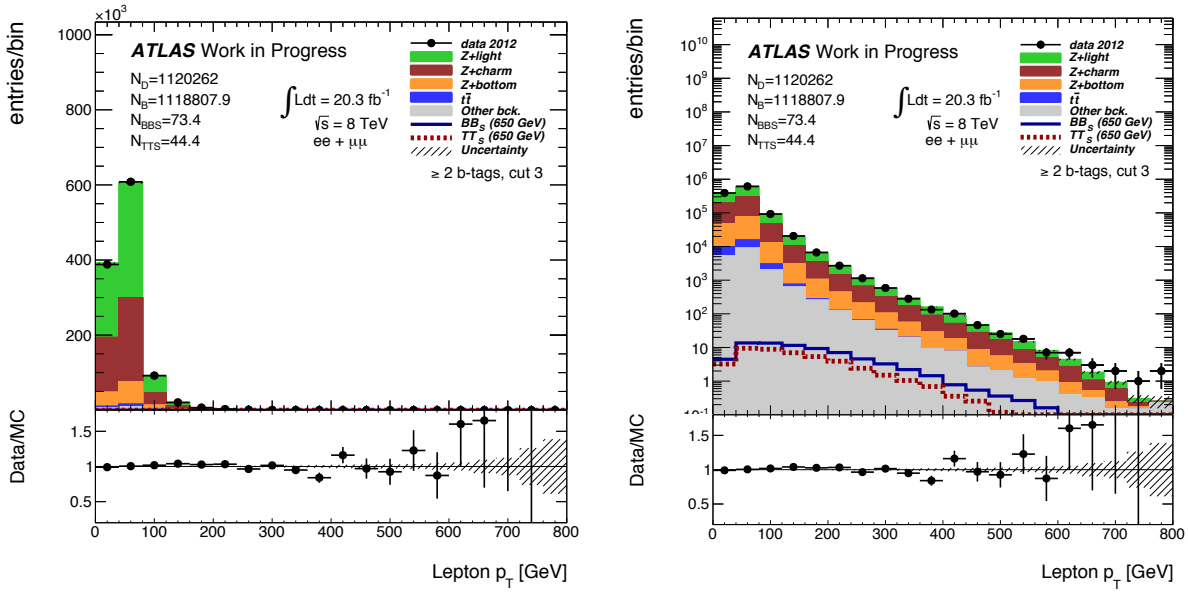

(c)

(d)

Figure 4.6.2: The E and p_T distributions for leptons, in the $ee + \mu\mu$ channel, after requiring $Z+ \geq 2$ jets.

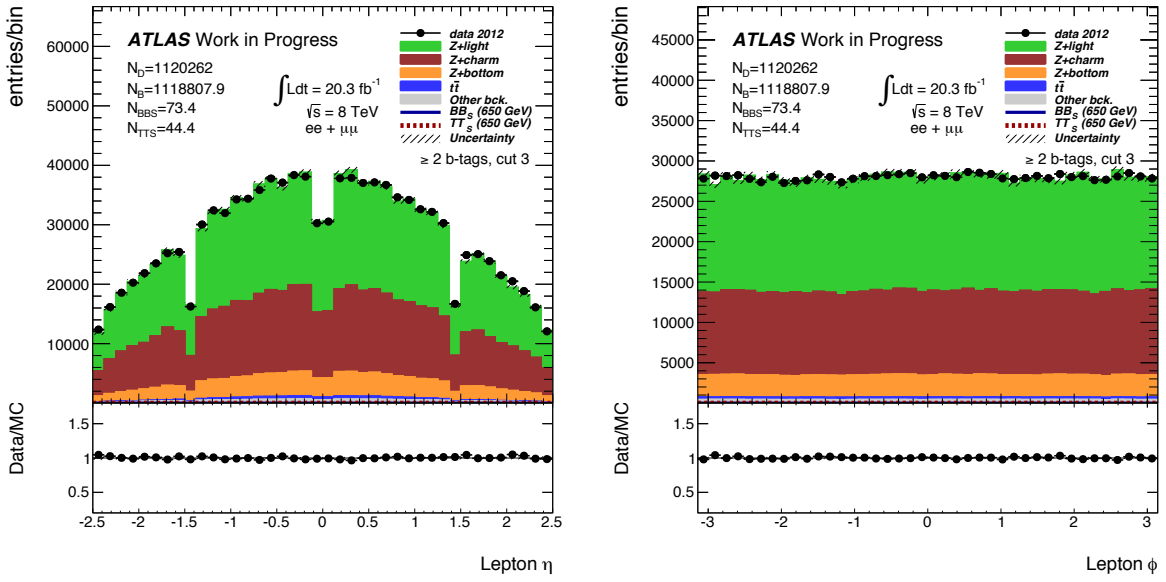

(a) (b)

Figure 4.6.3: The η and ϕ distributions for leptons, in the $ee+\mu\mu$ channel, after requiring $Z+ \geq 2$ jets.

quark decay, the decay of a top quark, or the decay of a Higgs boson. Furthermore, in order to effectively suppress the existent large Z+jets background, events are required to contain at least two b-tagged jets. Hence, to test the signal plus background hypothesis, it is useful to categorize events in two main regions: those belonging to the signal region, with $N_{tag} \geq 2$; and the ones with $N_{tag} < 2$, defining the control regions, whose purpose is to validate the modeling of the backgrounds. Indeed, analysing the signal and background event content listed in table 4.1, after requiring a Z boson candidate and at least two jets, where $N_{tag} = 0$, it is straightforward to see that this is a background dominated region: there are only a few dozens of signal events ($B\overline{B}_S$ and $T\overline{T}_S$), when compared to a total of approximately 5×10^5 background events. On the other hand, the ratio between the number of signal and background events is much larger for the signal region, after requiring $p_T(Z) > 150$ GeV: there are approximately three dozens of signal events, while the number of total background events is now reduced for ~ 500 events.

Figs. 4.6.7-4.6.8 are depicted the p_T distributions for the two higher-p_T b-tagged jets, after a $Z+ \geq 2$ jets, further requiring at least two b-tagged jets. The distribution of the transverse momentum of the Z boson candidate is also shown in fig. 4.6.9, at the same selection level, for $N_{tag} = 1$ and $N_{tag} \geq 2$; refer also to table 4.1.

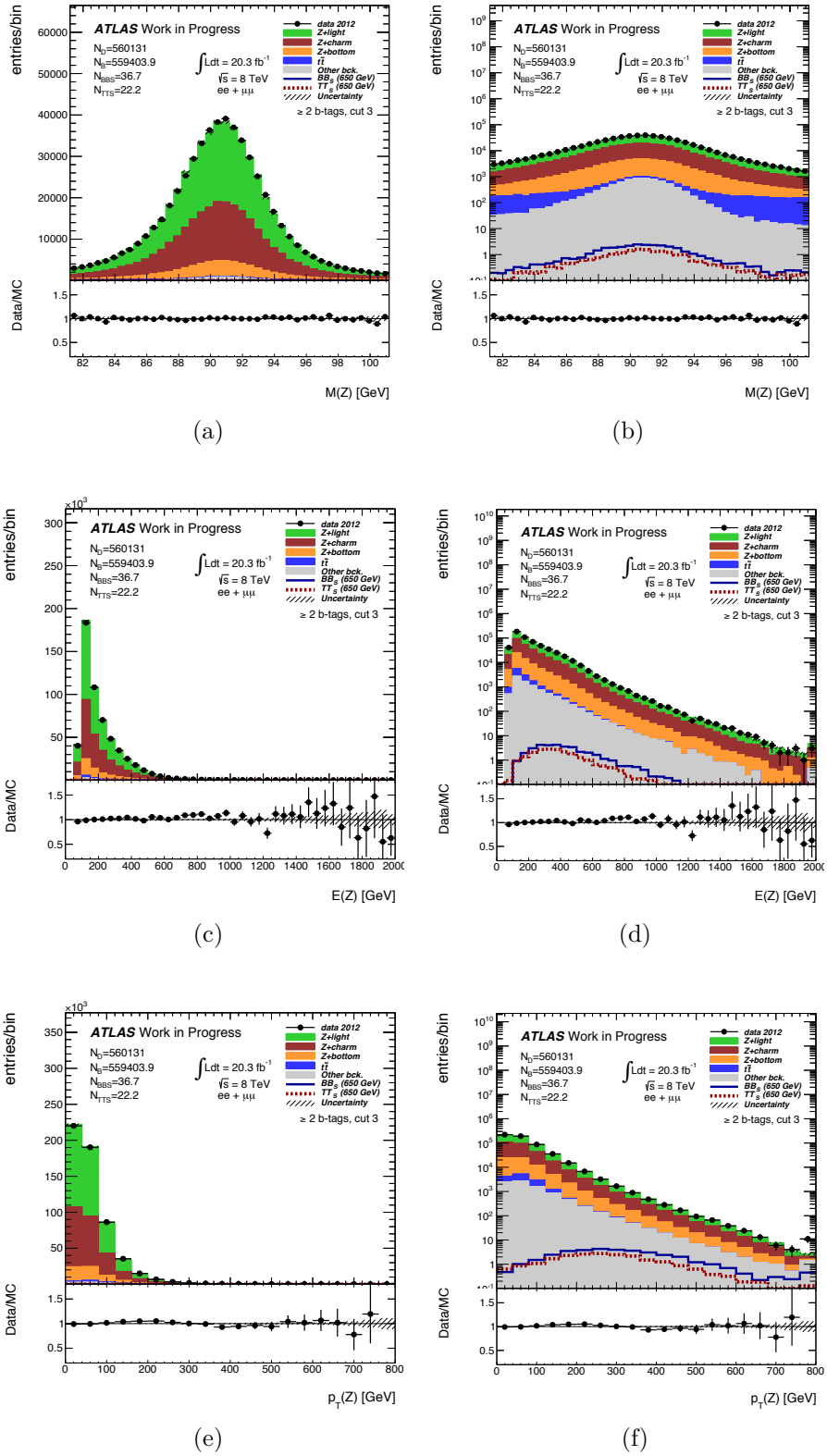

Figure 4.6.4: Distributions for the Z boson candidate, in the $ee + \mu\mu$ channel, after requiring $Z+ \geq 2$ jets. Panels (a) and (b) show the invariant mass, $M(Z)$, panels (c) and (d) show the energy E, while (e) and (f) show the transverse momentum, $p_T(Z)$.

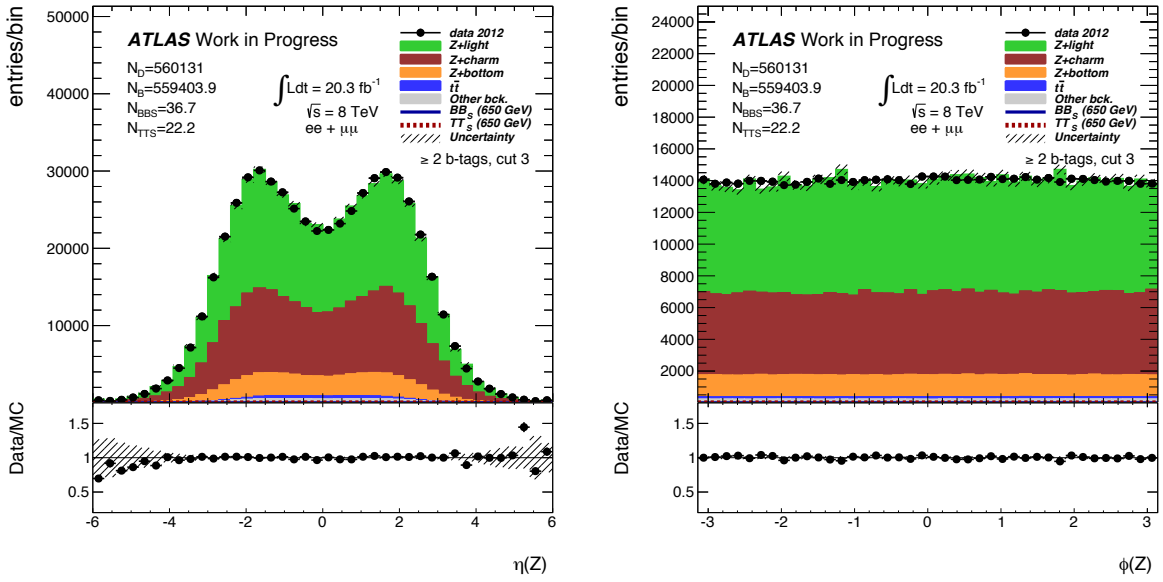

(a) (b)

Figure 4.6.5: The η and ϕ distributions for the Z boson candidate, in the $ee+\mu\mu$ channel, after requiring $Z+ \geq 2$ jets.

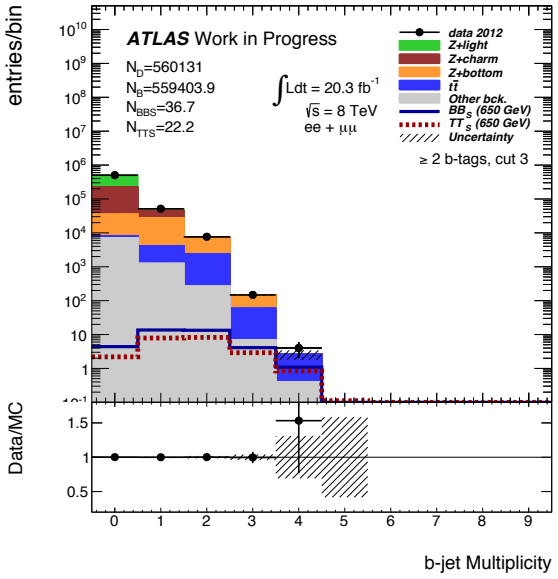

(a)

Figure 4.6.6: Distribution of b-tagged jets multiplicity, in the $ee + \mu\mu$ channel, after requiring $Z+ \geq 2$ jets.

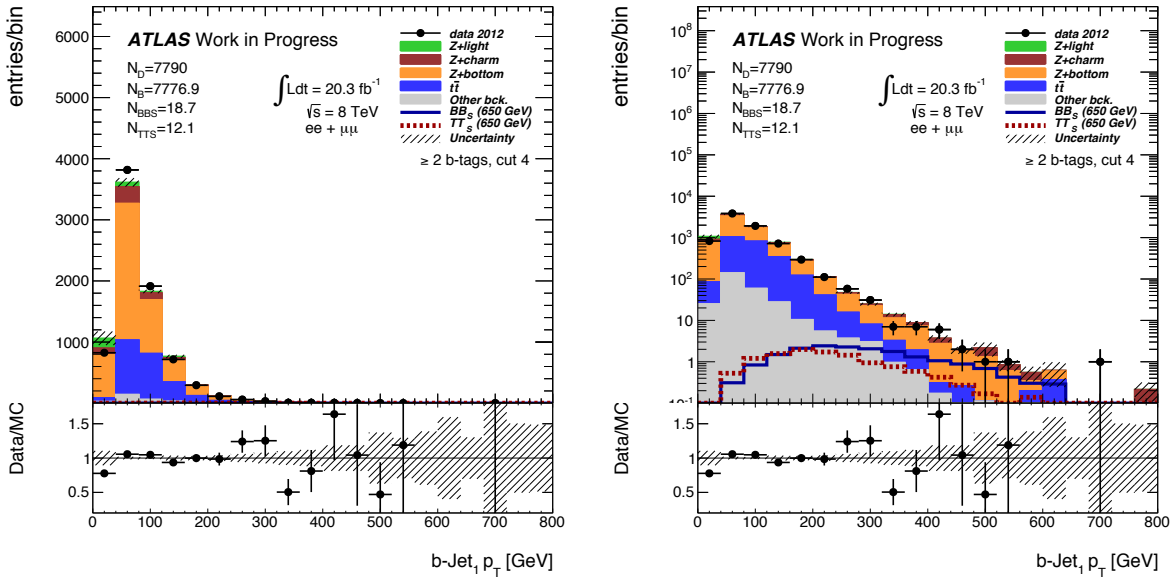

(a) (b)

Figure 4.6.7: The p_T distributions of the highest-p_T b-tagged jet, in the $ee + \mu\mu$ channel, after requiring $Z+ \geq 2$ jets and $N_{tag} \geq 2$.

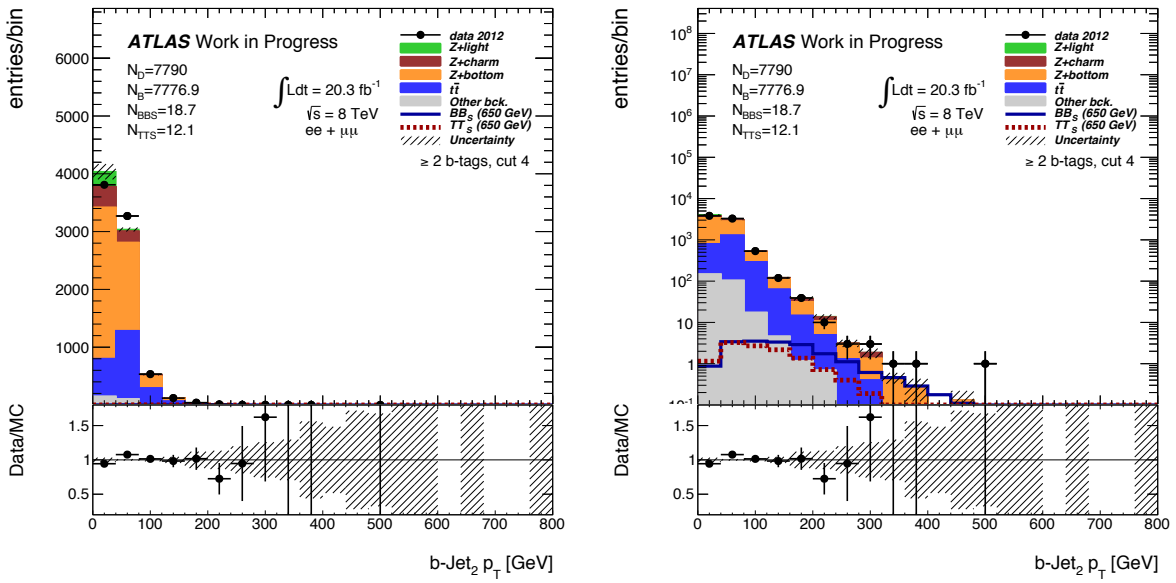

(a) (b)

Figure 4.6.8: The p_T distributions of the second higher-p_T b-tagged jet, in the $ee + \mu\mu$ channel, after requiring after requiring $Z+ \geq 2$ jets and $N_{tag} \geq 2$.

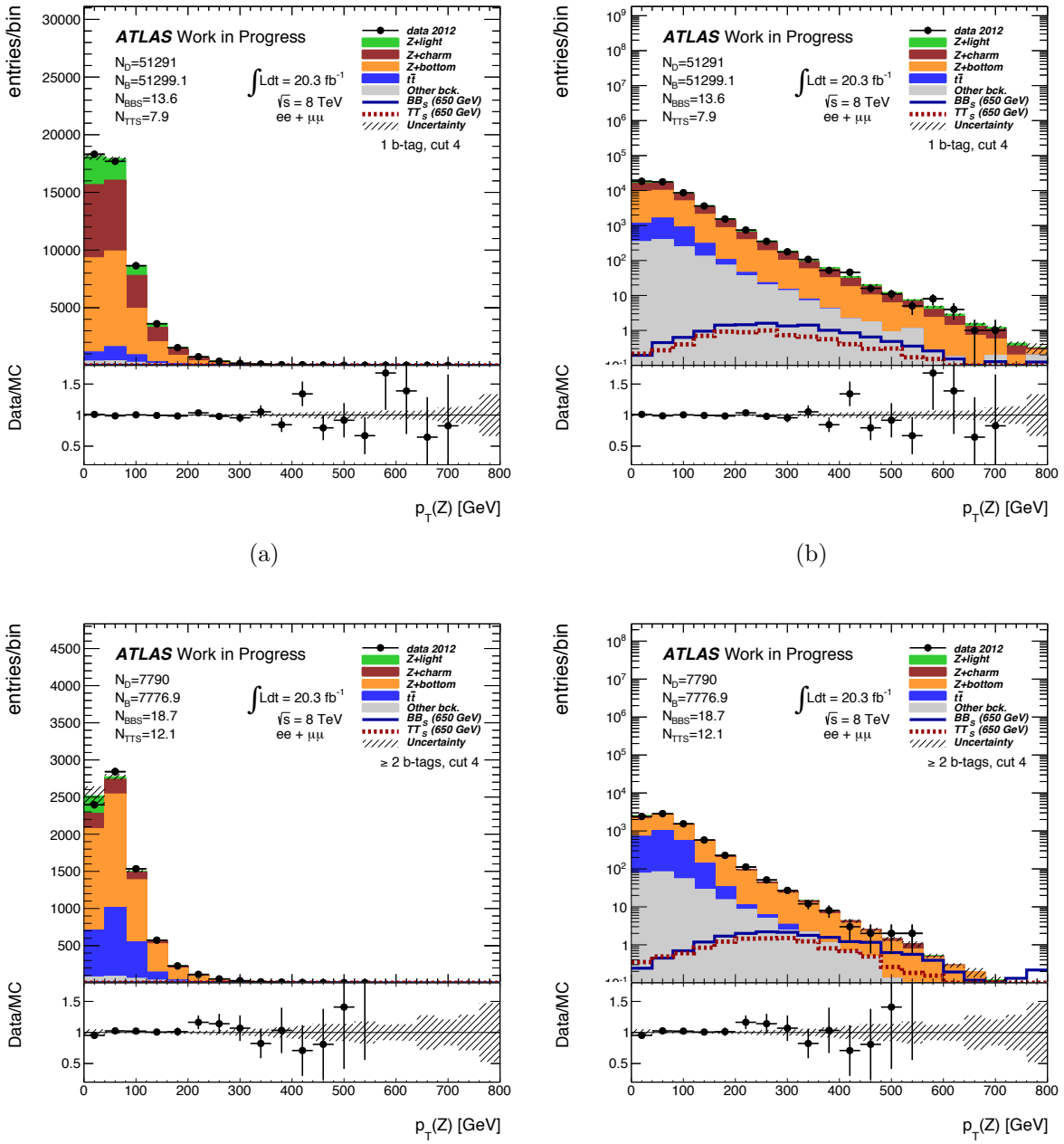

Figure 4.6.9: The p_T distribution for the Z boson candidate, in the $ee + \mu\mu$ channel, after requiring $Z+ \geq 2$ jets , $N_{tag} = 1$ (upper panel) and $N_{tag} \geq 2$ (down panel).

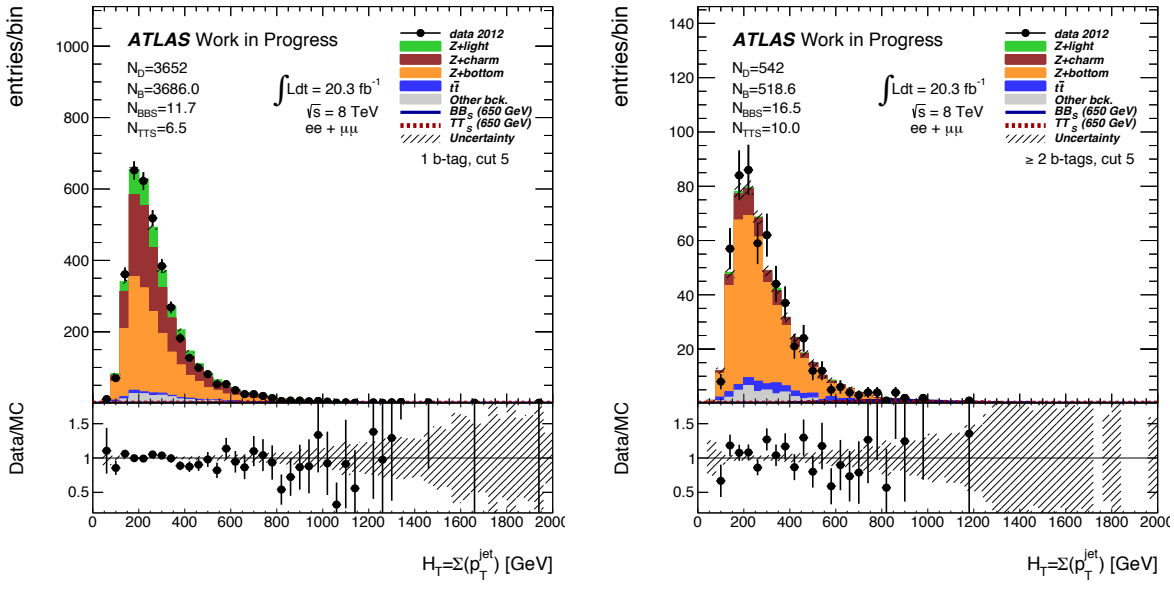

(a) (b)

Figure 4.6.10: The H_T(jets) distribution, in the $ee+\mu\mu$ channel, after requiring $p_T(Z) > 150$ GeV; for $N_{tag} = 1$ (a) and $N_{tag} \geq 2$ (b).

The extraction of a $T\bar{T}$ and $B\bar{B}$ signal in the presence of a large background can be boosted by knowing that vector-like quarks T/B are heavy, hence produced with relatively low momenta. Because of this, their decay products are often emitted with large momenta at large angles to the initial beam direction. This naturally defines a signal region that is characterized by a high-p_T Z boson, which justifies an additional requirement: $p_T(Z) > 150$ GeV. This requirement on the minimum transverse momentum of the Z boson is common in searches for heavy quarks (refer to [37] and experimental results in [52]), since it largely reduces the dominant $t\bar{t}$ background in the signal region $N_{tag} \geq 2$. Indeed, when analysing panel (c) in fig. 4.6.1, it is clear that there is an advantage in cutting the p_T near the 150 GeV, since there is a significant portion of the background that will not have to be dealt with.

Signal events from VLQ pair production often produce several energetic jets (as seen in the jet-multiplicity distribution in fig. 4.6.1 (a)), which makes the scalar sum of the transverse momenta of all jets in the event, H_T(jets), a powerful variable to further reduce the background, in particular the $Z+$jets fraction. The H_T(jets) distribution is shown in fig. 4.6.10, after requiring $p_T(Z) > 150$ GeV.

The final selection level of the current ATLAS analysis [3] is characterized by H_T(jets) $>$ 600 GeV. The invariant mass for the Zb system, reconstructed with a Z boson candidate

reconstructed from a pair of oppositely charged electrons or muons, and the highest p_T $b-$tagged jet, is plotted in fig. 4.6.11. The B quark, decaying to a Z boson and a bottom quark, was reconstructed in previous works by the ATLAS Collaboration, namely in [5, 3].

Explicit Reconstruction of Vector-like Quarks

After reviewing the relevant steps of the analysis, the goal now is to reconstruct the vector-like quark T. Hence, this work is focused on the decay of a vector-like quark T to a Z boson and top quark. The objects characterizing this decay were reconstructed: the W boson plus the Zb system (since the top quark decays to a W boson and a bottom quark). The best W that can be reconstructed is by choosing the 2 jets whose invariant mass sum is the closest to the real W boson, i.e. the difference between the two jets invariant mass and $M(W)_{\text{PDG}} \simeq 80.385$ GeV [65] is minimum. Then, the vector-like quark T can be obtained by summing the Lorentz 4-vectors of the reconstructed W and the Zb system. The Zb system invariant mass is illustrated in fig. 4.6.12. The objects reconstructed will be simply referred to by "W" and "T", in what follows, and are presented in fig. 4.6.13 and fig. 4.6.14, respectively, after requiring $p_T(Z) > 150\,\text{GeV}$. Since the $H_T(\text{jets})$, whose distribution is depicted in fig. 4.6.10, appears to be an attractive choice for a discriminant variable, the $H_T(\text{jets}) > 600$ GeV selection cut is relaxed to allow for a multivariate analysis with this variable as an input.

The $\triangle R$ distributions between the two leptons used in the Z boson candidate reconstruction and the two highest-p_T $b-$tagged jets, corresponding to 6 distinct distributions, are also presented in figs. 4.6.15-4.6.20, after requiring $p_T(Z) > 150$ GeV.

4.7 Discriminating Variables

This section is devoted to the presentation of kinematic distributions that were found to have the most signal-background dicrimination potential, fitting the role of best discriminant variables. Here are included linear distributions with events containing a high transverse momentum Z boson candidate reconstructed from a pair of oppositely charged leptons and at least two jets, in which at least two are b-tagged, further satisfying $p_T(Z) > 150\,\text{GeV}$. The goal now is to evaluate how much can the results be improved by using multivariate techniques, instead of applying selection cuts and decreasing statistics (both background and signal).

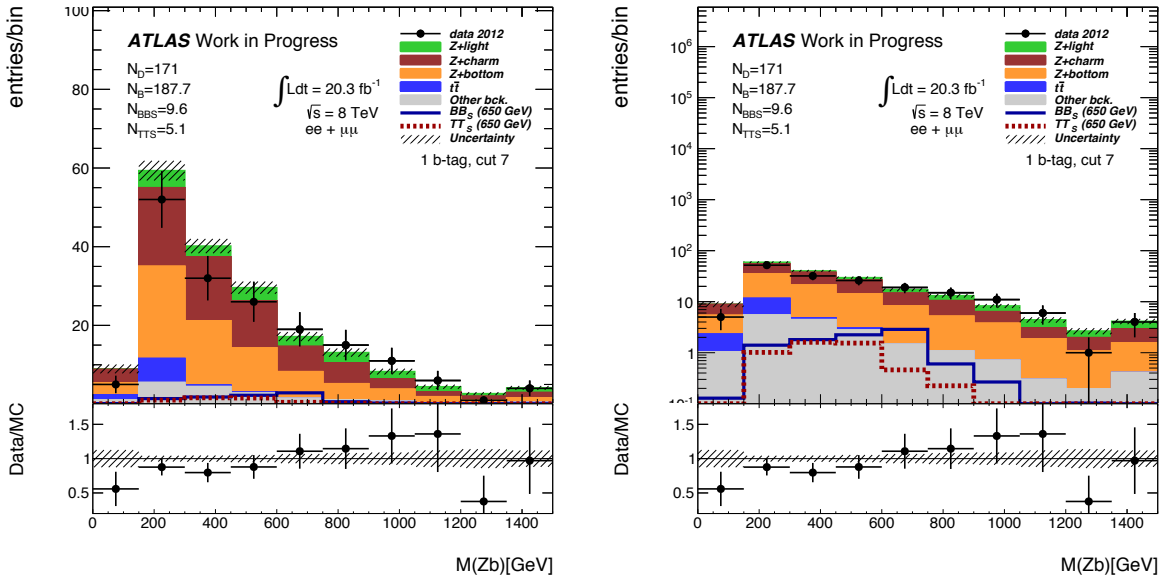

(a)

(b)

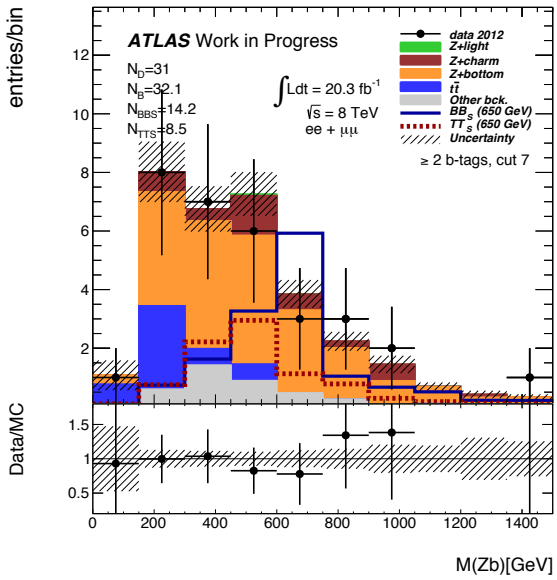

(c)

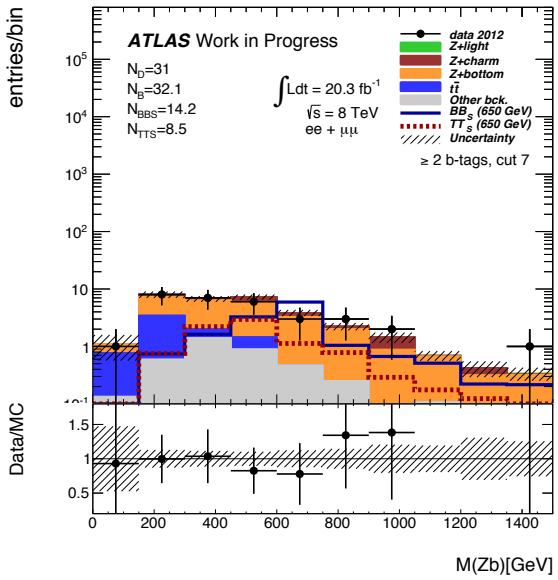

(d)

Figure 4.6.11: The $m(Zb)$ invariant mass distributions, in the $ee + \mu\mu$ channel, after requiring $H_T > 600\,\text{GeV}$. Upper panels: $N_{tag} = 1$; down panels: $N_{tag} \geq 2$.

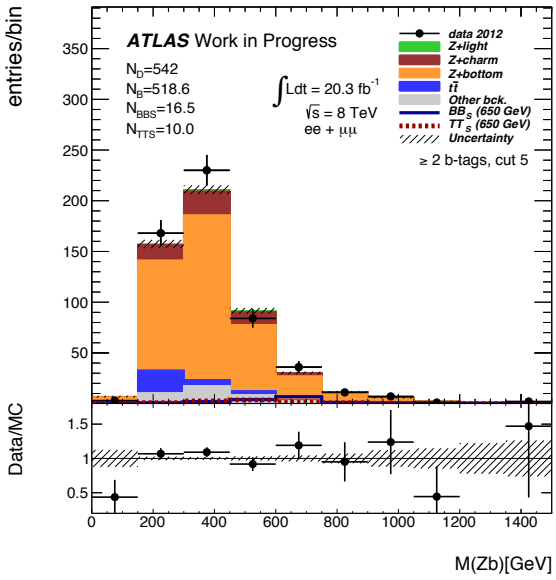

(a)

Figure 4.6.12: The $m(Zb)$ invariant mass distributions, in the $ee + \mu\mu$ channel, after requiring $p_T(Z) > 150$ GeV.

The cut in the H_T(jets) variable (fig. 4.6.10) was relaxed, so it can be used as a discriminating variable, in order to investigate if it is possible to obtain better signal-background separation by using a multivariate analysis, instead of cutting further to supress the background, simultaneously compromising a significant fraction of the number of signal events available (refer to fig. 4.6.1, panel (d)). The distributions chosen to be used as discriminating variables in a multivariate analysis were the transverse momentum of the two higher-p_T b-tagged jets, $p_T(b1)$ and $p_T(b2)$, the total jet transverse momenta H_T(jets), the ΔR distribution between the two higher-p_T b-tagged jets, $\Delta R(b1b2)$, and the reconstructed T quark invariant mass, giving a total of 5 distinct discriminating variables, presented in fig. 4.7.1. The invariant mass of the Zb system, $M(Zb)$, plotted in fig. 4.6.11, which presents itself as a natural discriminant, only depending on the Z and the bottom quark 4-Lorentz vectors, was already studied in [3], hence it will not be studied here.

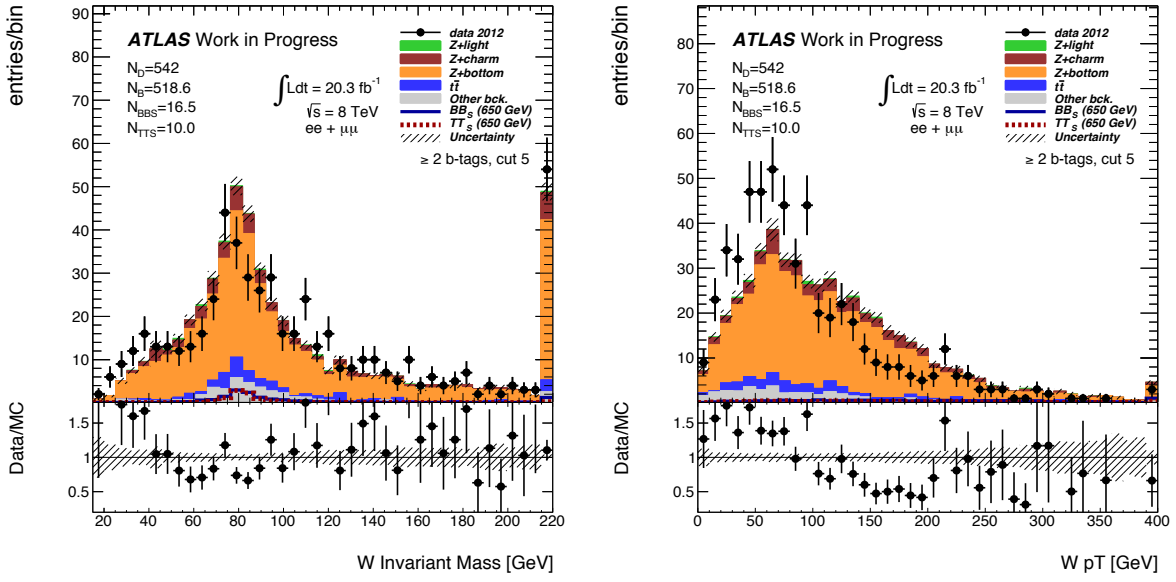

(a)

(b)

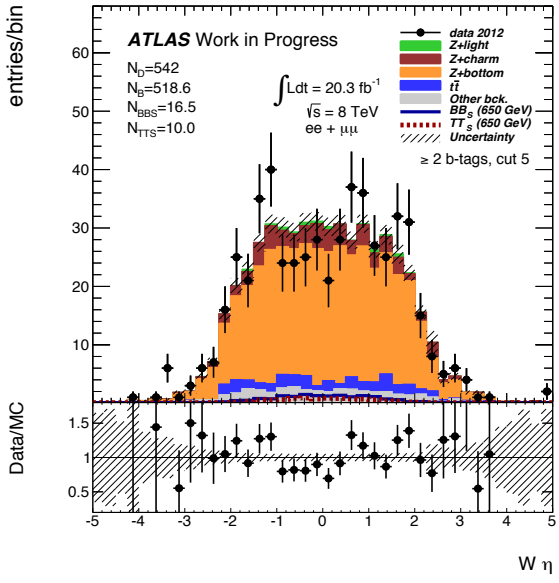

(c)

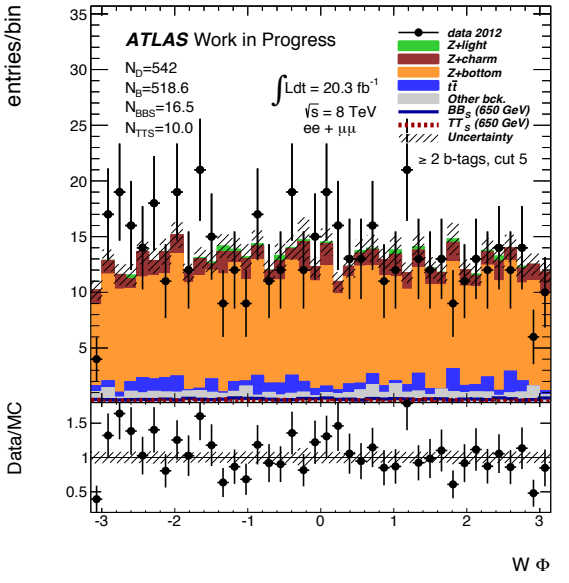

(d)

Figure 4.6.13: The invariant mass (a), p_T (b), η (c) and ϕ (d) distributions for the reconstructed (hadronic) W boson invariant mass (from 2 jets, excluding the dominant b-jet), in the $ee + \mu\mu$ channel, after requiring $p_T(Z) > 150\,\text{GeV}$ and $N_{tag} \geq 2$.

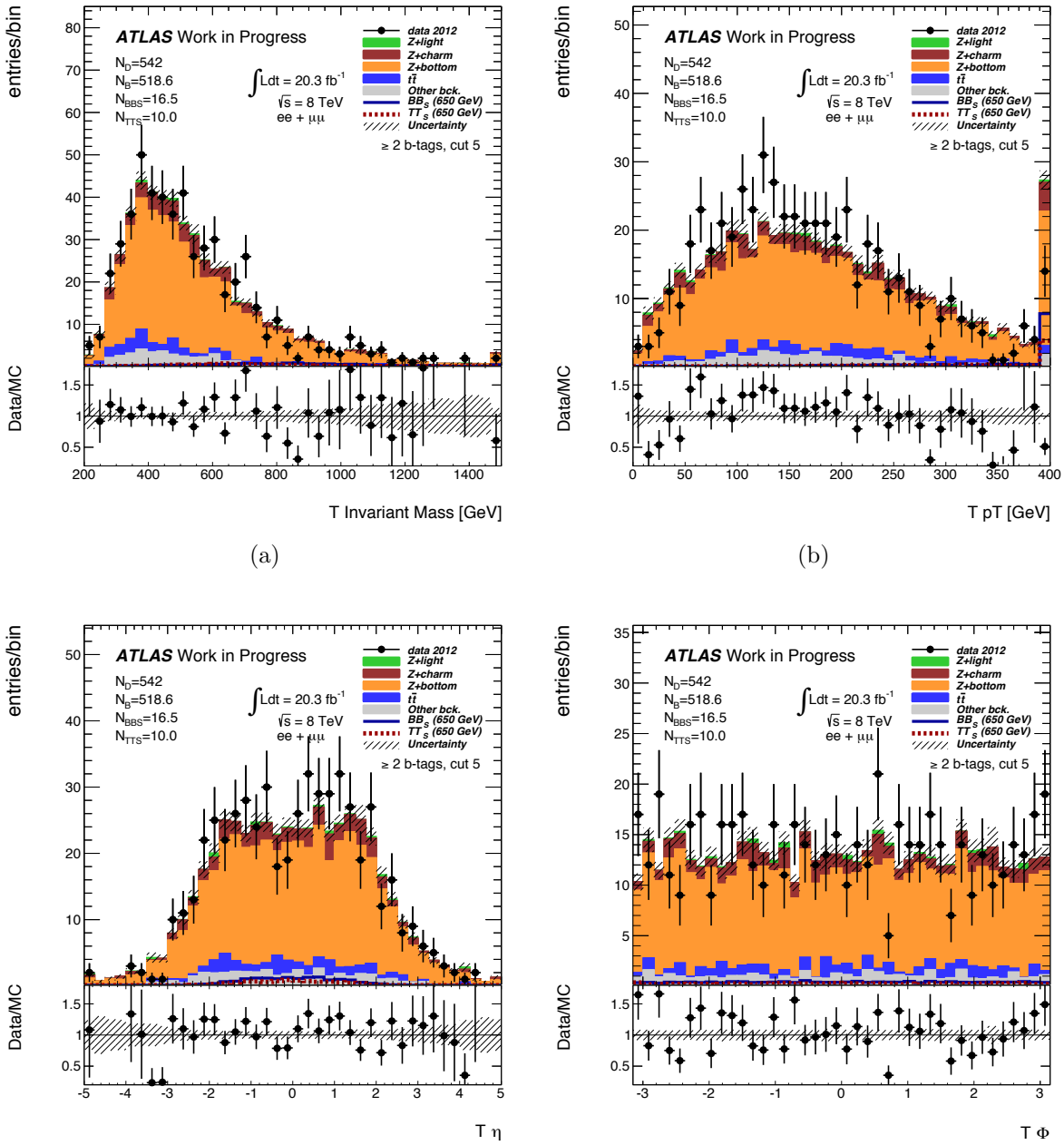

Figure 4.6.14: The invariant mass (a), p_T (b), η (c) and ϕ (d) distributions for the reconstructed T invariant mass (from W and the Zb system), in the $ee+\mu\mu$ channel, after requiring $p_T(Z) > 150$ GeV and $N_{tag} \geq 2$.

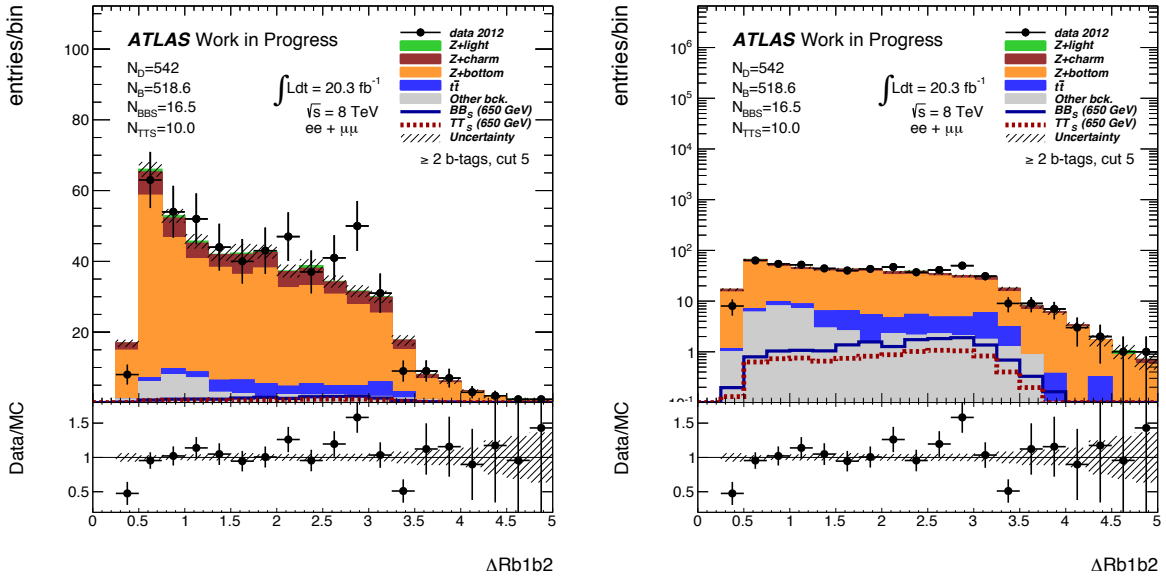

(a) (b)

Figure 4.6.15: The ΔR distributions between the two higher-p_T b-tagged jets, in the $ee + \mu\mu$ channel, after requiring $p_T(Z) > 150$ GeV and $N_{tag} \geq 2$.

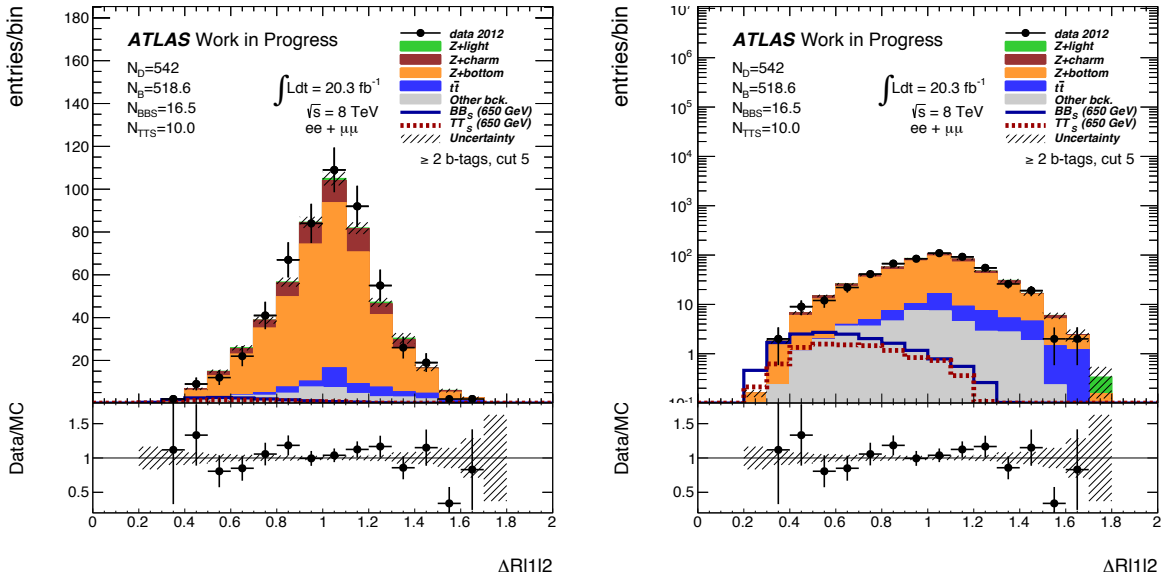

(a) (b)

Figure 4.6.16: The ΔR distributions between the two leptons (from the Z boson candidate reconstruction), in the $ee + \mu\mu$ channel, after requiring $p_T(Z) > 150$ GeV and $N_{tag} \geq 2$.

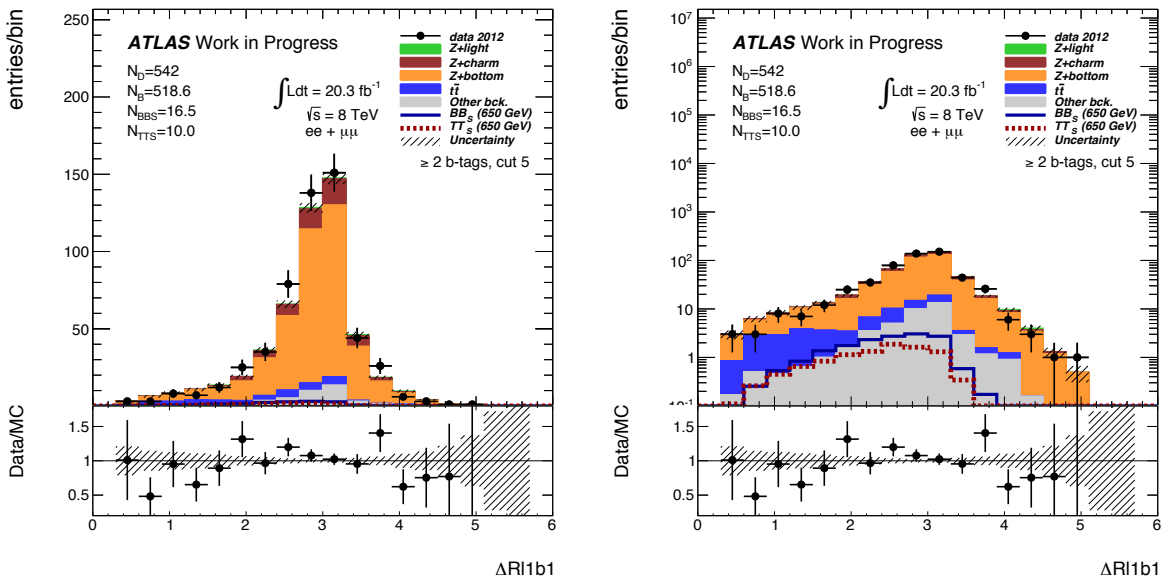

(a) (b)

Figure 4.6.17: The ΔR distributions between the highest-p_T b-tagged jet and the first lepton (used in the Z boson candidate reconstruction), in the $ee + \mu\mu$ channel, after requiring $p_T(Z) > 150$ GeV and $N_{tag} \geq 2$.

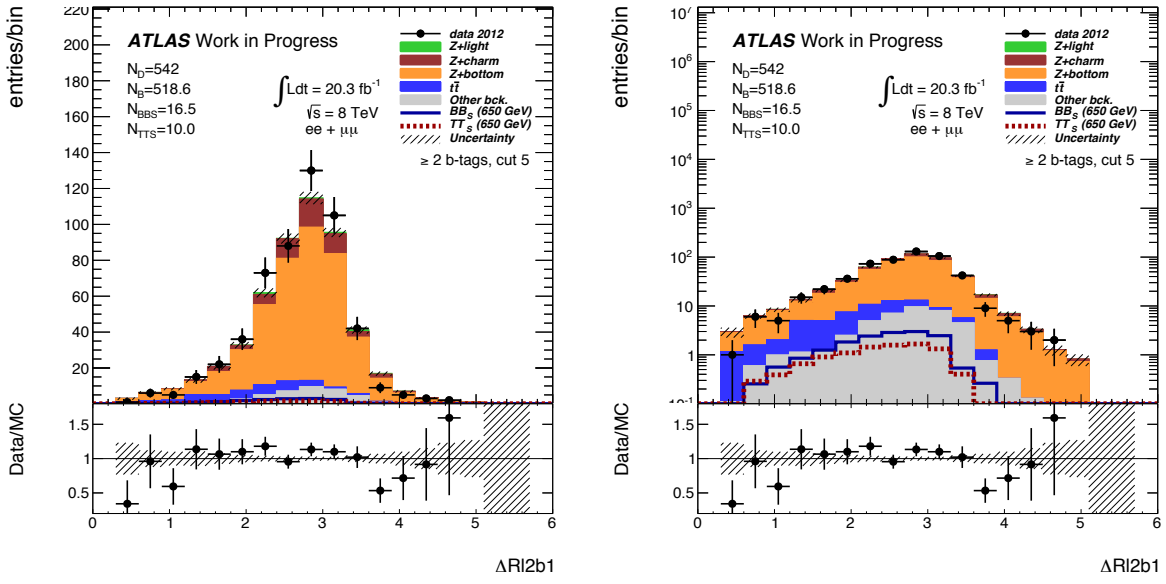

(a) (b)

Figure 4.6.18: The ΔR distributions between the highest-p_T b-tagged jet and the second lepton (used in the Z boson candidate reconstruction), in the $ee + \mu\mu$ channel, after requiring $p_T(Z) > 150$ GeV and $N_{tag} \geq 2$.

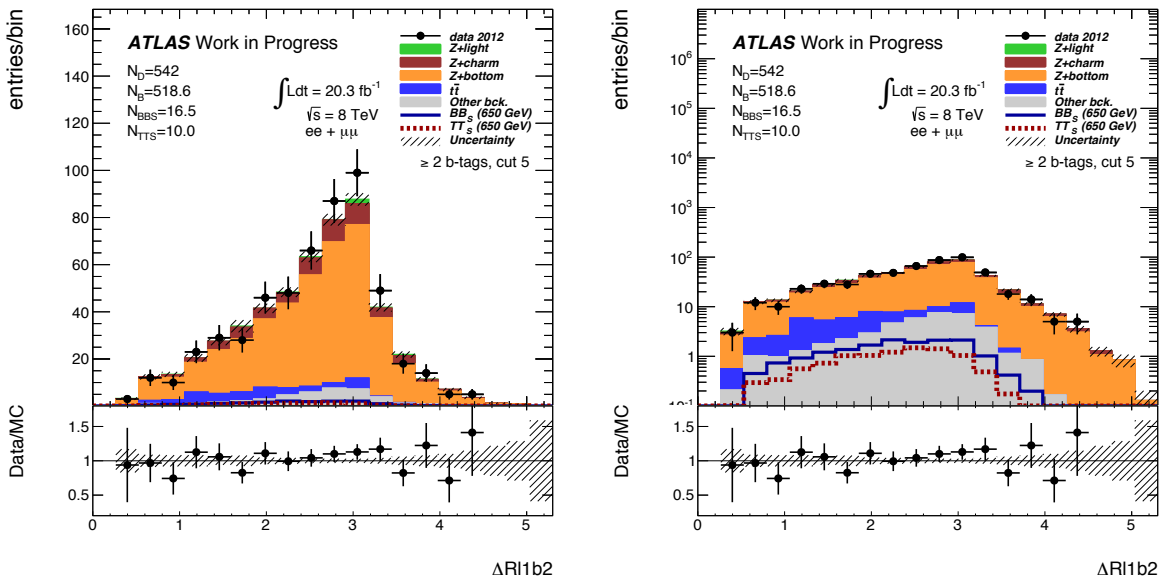

(a) (b)

Figure 4.6.19: The ΔR distributions between the second higher-p_T b-tagged jet and the first lepton (used in the Z boson candidate reconstruction), in the $ee+\mu\mu$ channel, after requiring $p_T(Z) > 150$ GeV and $N_{tag} \geq 2$.

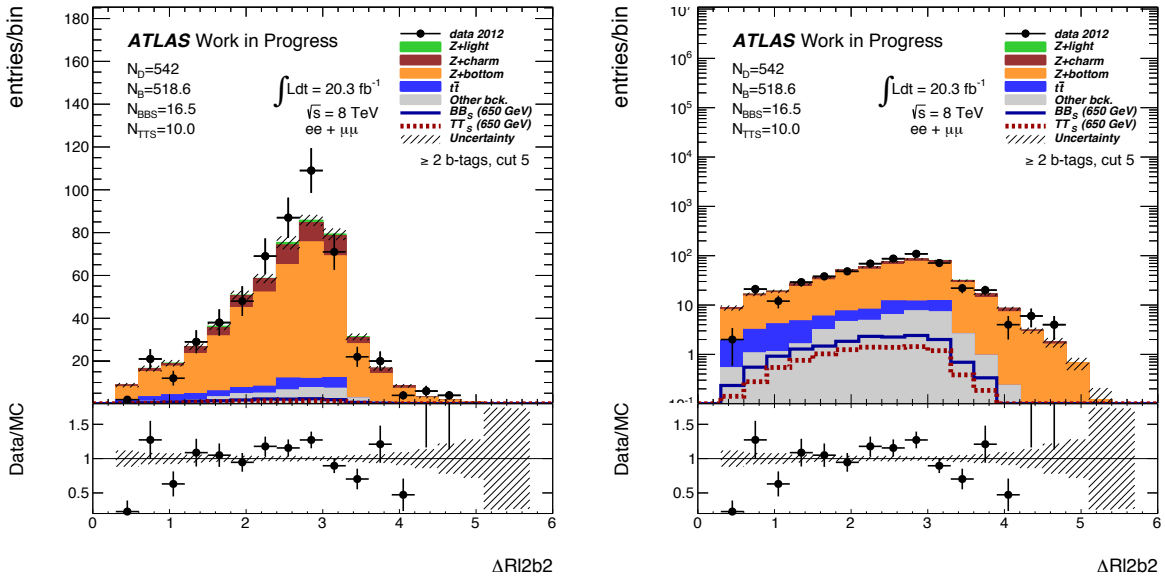

(a) (b)

Figure 4.6.20: The ΔR distributions between the second higher-p_T b-tagged jet and the second lepton (used in the Z boson candidate reconstruction), in the $ee+\mu\mu$ channel, after requiring $p_T(Z) > 150$ GeV and $N_{tag} \geq 2$.

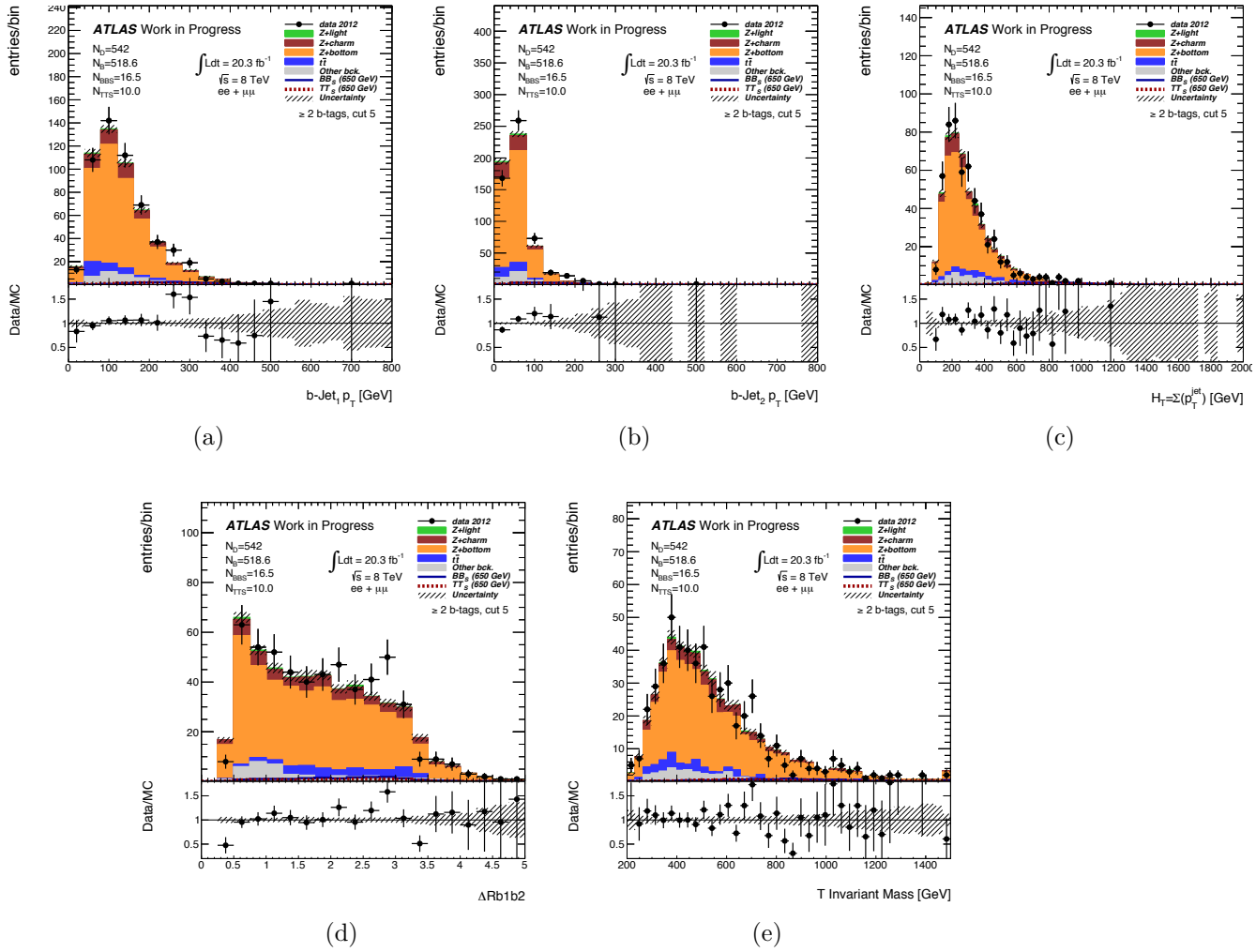

Figure 4.7.1: The chosen discriminating variables: (a) $p_T(b1)$, (b) $p_T(b2)$, (c) H_T(jets), (d) $\Delta R(b1b2)$ and (e) T invariant mass, in the $ee + \mu\mu$ channel, after requiring $p_T(Z) > 150\,\text{GeV}$ and $N_{tag} \geq 2$.

5 Multivariate Analysis with TMVA

In high-energy physics, with the search for ever smaller signals in ever larger data sets, it has become essential to extract a maximum of the available information from the data. The ATLAS experiment at CERN collects enormous amount of data, hence the use of data mining techniques can be a real help. In a Multivariate Analysis (MVA), variables potentially useful in signal-background discrimination are used as input in multivariate classifiers, which separate (classify) multidimensional data into categories, for instance signal and background.

An MVA analysis is performed with the TMVA (Toolkit for Multivariate Data Analysis with ROOT) package [10], using as input the discriminating variables chosen in section 4.7.

5.1 Multivariate Analysis Classifiers outlined

This section briefly outlines the multivariate analysis classifiers used in this work: a boosted decision tree (BDT), a linear discriminant (LD) and a neural network (MLPBNN).

Boosted Decision Tree (BDT)

A decision tree is a binary tree structured classifier that allows a straightforward interpretation, since it can be visualized by a single two-dimensional structure, as illustrated by fig. 5.1.1. Repeated left/right (yes/no) decisions are taken on one single variable at a time until a stop criterion is fulfilled. The phase space is separated this way into several regions that are eventually categorized in signal or background, depending on the majority of training events that end up in the final $leaf$ node. For decision trees, each output node represents a specific value of the target variable. The boosting of a decision tree extends this concept from one tree to several trees, which constitute a $forest$. The trees are derived from the same training set by reweighting events, being finally combined into a single classifier which is given by a weighted average of all the individual

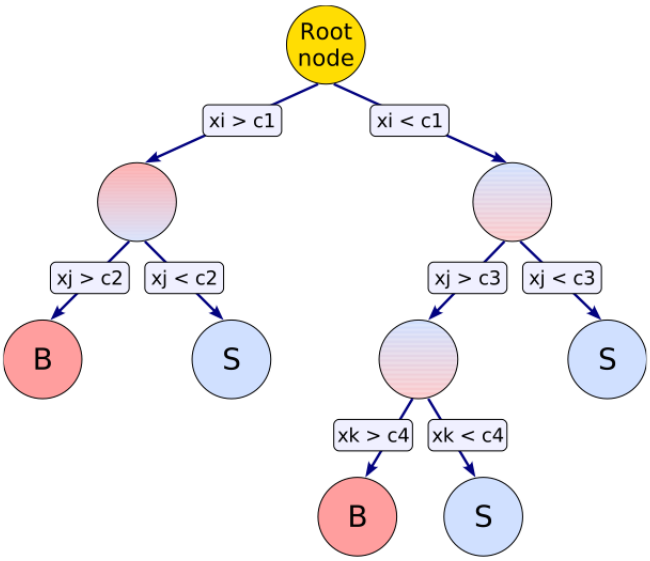

Figure 5.1.1: Schematic view of a decision tree. Starting from the root node, a sequence of binary splits using the discriminating variables x_i is applied to the data. Each split uses the variable that at this node gives the best separation between signal and background when being cut on. The same variable may thus be used at several nodes, while others might not be used at all. The leaf nodes at the bottom end of the tree are labeled "S" for signal and "B" for background depending on the majority of events that end up in the respective nodes (figure extracted from [10]).

decision trees. Boosting increases the statistical stability of the classifier trees, and also improves the separation performance, when compared to a single decision tree.

Linear Discriminant (LD)

The linear discriminant analysis provides data classification using a linear model, where linear refers to the discriminant function $y(x)$ being linear in the parameters β, for $y(x) = x^T\beta + \beta_0$, where β_0 (denoted the bias) is adjusted so that for signal $y(x) \geq 0$ and $y(x) < 0$ for background. It can be shown that this is equivalent to the Fisher discriminant (refer to [10] for a detailed description), which seeks to maximise the ratio of between-class variance to within-class variance by projecting the data onto a linear subspace.

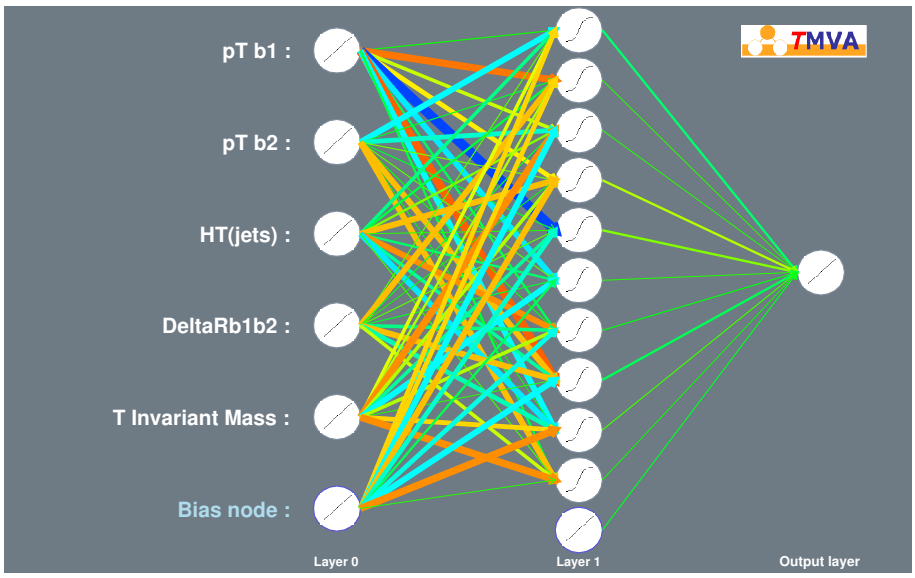

Figure 5.1.2: Multilayer perceptron (MLP) neural network with one hidden layer.

Artificial Neural Network (MLPBNN)

An Artificial Neural Network (ANN) is defined as any simulated ensemble of interconnected neurons, with each neuron producing a certain response at a given set of input signals. By applying an external signal to some input neurons, the network is put into a defined state that can be measured by the response of one (or several) output neurons. One can therefore understand the neural network as a mapping from a space of input variables $x_1, ..., x_{n_{var}}$ onto a one-dimensional space, in case of a signal-versus-background problem, or a multi-dimensional space of output variables $y_1, ..., y_{m_{var}}$. The mapping is nonlinear it at least one neuron has a nonlinear response to its input. In this study it is used an MLP (multi-layer perceptron) neural network [1]. While in principle a neural network with n neurons can have n^2 directional connections, the complexity can be diminished by organising the neurons in layers and only allowing direct connections from a given layer to the following layer. This kind of neural network is named multi-layer perceptron (MLP). The first layer of a multilayer perceptron is the input layer, the last one is the ouput layer, and the ones between these are termed hidden layers. Fig. 5.1.2 illustrates the architecture of a MLP neural network with one hidden layer.

[1] In particular the MLPBNN extension, which employs the Broyden-Fletcher-Goldfarb-Shannon (BFGS) training method and a bayesian regulator (refer to [10] for a detailed description).

5.2 Training/testing MVA Classifiers

In this study the problem to solve is one of classification: the goal is to separate signal from background. It is used a $T\bar{T}$ production signal sample, assuming $SU(2)$ singlet quarks with a mass of 700 GeV, and a background sample which includes all the distinct backgrounds used in the present analysis for vector-like quarks pair-production, whose modeling is explained in section 4.5. The signal sample for VLQs with a mass of 700 GeV is assumed to be the benchmark, since it is in this mass region that limits are expected to be improved (as will be seen in section 6.1.1).

The first step in a classification analysis is to define input variables, which correspond to the best discriminating variables chosen. In this case, the input variables used are the transverse momentum of the two higher-p_T b-tagged jets, the total jet transverse momenta H_T(jets), the ΔR distribution between the two higher-p_T b-tagged jets and the invariant mass of the T, as outlined in section 4.7. These variables are presented in fig. 5.2.1, in the $ee + \mu\mu$ channel, after requiring $p_T(Z) > 150$ GeV and $N_{tag} \geq 2$, with a reference signal displayed corresponding to $T\overline{T}$ production, assuming $SU(2)$ singlet quarks with a mass of 700 GeV.

The linear correlation coefficients for the variables included in the signal and background training samples, as well for the data sample, are organised in three matrices as depicted in figs. 5.2.2 and 5.2.3. As expected, for all the samples, the correlations are stronger between the variables corresponding to the transverse momenta of the two higher-p_T b-tagged jets and the total jet transverse momenta H_T(jets). Take, for instance, the correlations for the signal sample in fig. 5.2.2 (a): it is approximately 42% between H_T(jets) and p_T ($b1$). This is due to the definition of the H_T(jets) variable as the scalar sum of the transverse momenta of all the jets, which naturally includes the b-tagged ones. The correlation between H_T(jets) and p_T ($b1$) is stronger that the one between H_T(jets) and p_T ($b2$) ($\sim 24\%$), as expected, since the higher the energy, the higher the contribution to the p_T scalar sum H_T(jets), which justifies a stronger correlation. Notice that the aforementioned correlations are more enhanced in the background (fig. 5.2.2 (b)). Nevertheless, none of the supracited correlation coefficients is high enough to justify the exclusion of any of the variables from the multivariate analysis.

After training and testing, the most performing MVA methods are chosen and used to classify events in data samples with unknown signal and background composition. For the categorization of the multivariate methods trained and tested in terms of performance, it is useful to analyse the background rejection versus signal efficiency (efficiency=1-

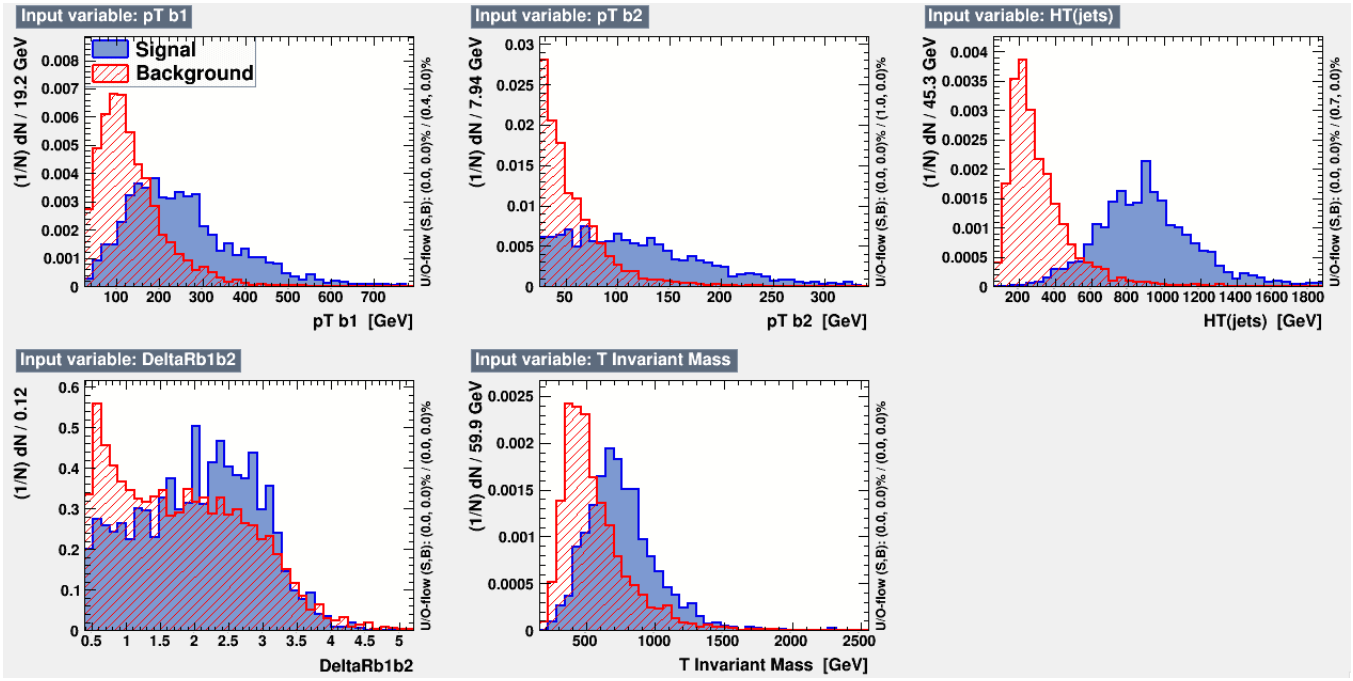

Figure 5.2.1: Unit-normalized input variable distributions, in the $ee + \mu\mu$ channel, after requiring $p_T(Z) > 150$ GeV and $N_{tag} \geq 2$. The reference signal displayed corresponds to $T\overline{T}$ production assuming $SU(2)$ singlet quarks with a mass of 700 GeV. Upper panel, from left to right: $p_T(b1)$, $p_T(b2)$ and H_T(jets). Down panel, from left to right: $\Delta R(b1b2)$ and the reconstructed T quark invariant mass. The vertical text on the right-hand side of the plots indicates the under- and overflows.

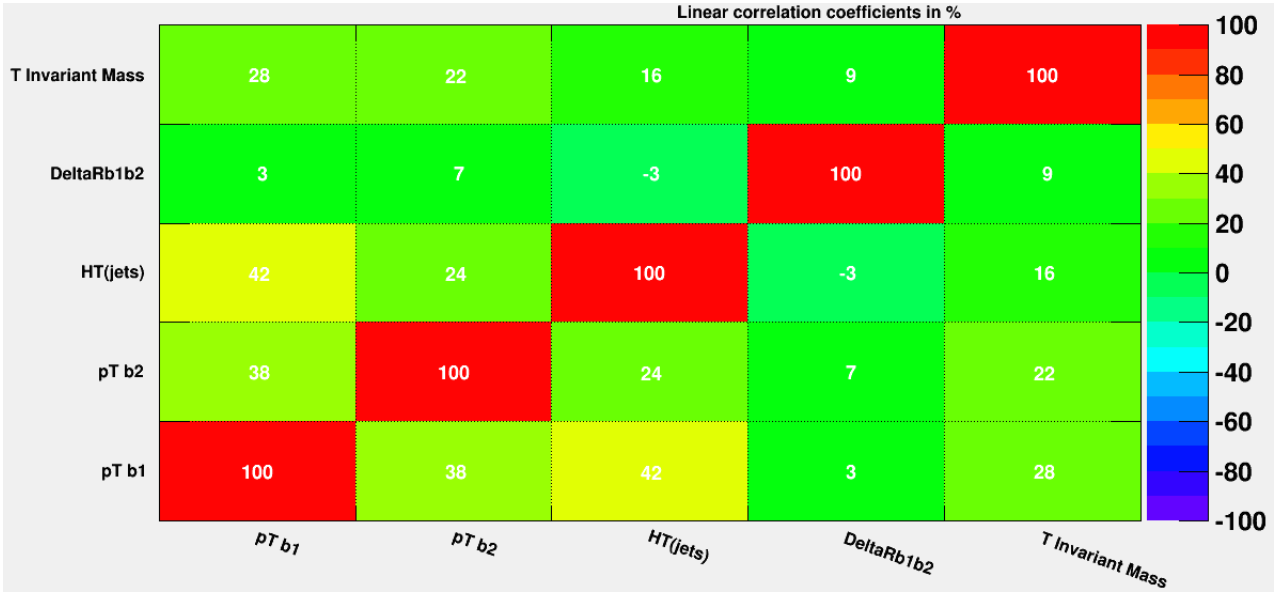

(a)

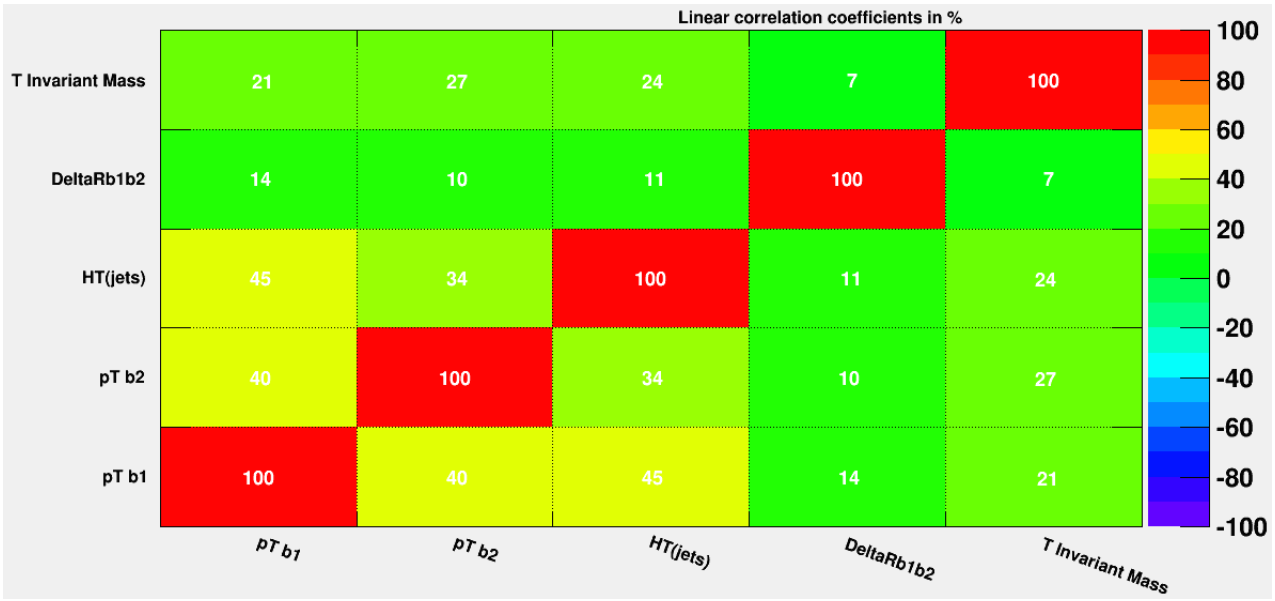

(b)

Figure 5.2.2: Linear correlation coefficients between the discriminating variables used: (a) for a $T\bar{T}$ production signal sample, assuming $SU(2)$ singlet quarks with a mass of 700 GeV; for the total background sample (b). These coefficients are obtained after training (and testing) the classifiers with the aforementioned samples as input.

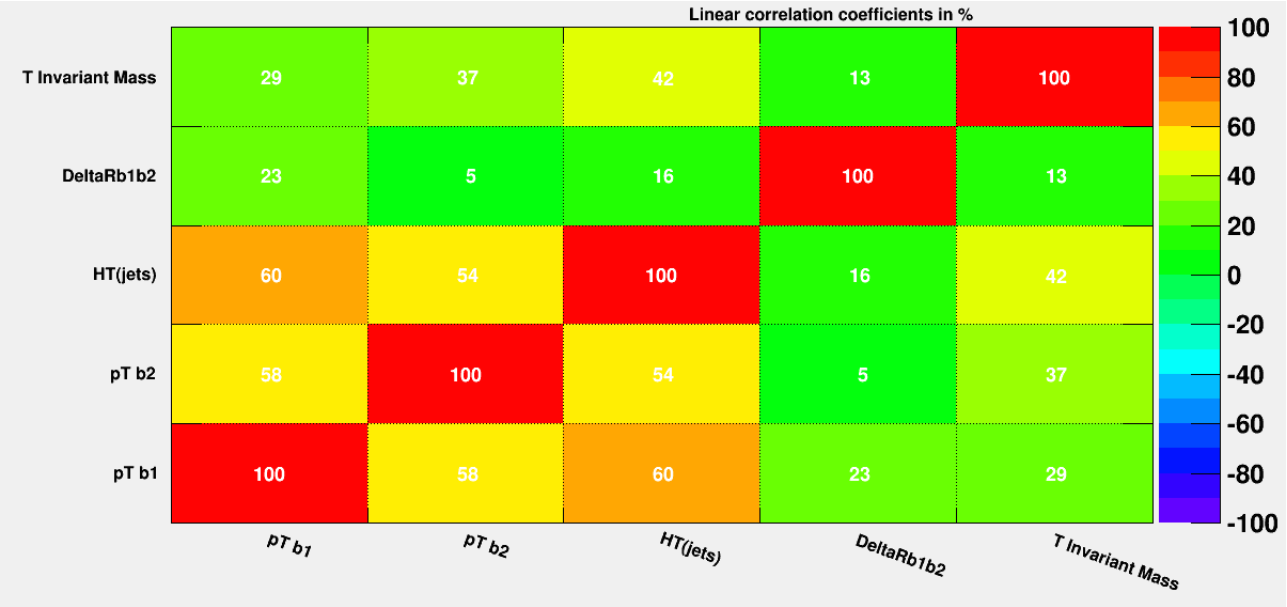

(a)

Figure 5.2.3: Linear correlation coefficients between the discriminating variables used for the data sample.

background rejection), also know as ROC (receiver operating characteristic) curve. The larger the area of the ROC curve, the better the performance. The BDT, the LD (linear discriminant) and the MLPBNN neural network were observed to deliver a good performance, as verified in fig. 5.2.4, hence are chosen to be used in the classification phase (section5.3). Notice, as well, the poor performance of the automatic cuts method implemented in the MVA algorithm, when compared to the other classifiers. These cuts are automatically performed and optimized by the MVA algorithm and correspond to the maximum performance in signal-background discrimination via this method, confirming the much lower gain when compared to the other methods presented.

The training is followed by the testing phase, whose goal is to ensure there was no overtraining. Overtraining occurs when a machine learning problem has too few degrees of freedom, because too many model parameters of an algorithm were adjusted to too few data points. Hence, the sensitivity to overtraining depends on the MVA classifier used. For instance, a linear discriminant can hardly ever be overtrained, whereas, without the appropriate counter measures, boosted decision trees can suffer from at least partial overtraining, owing to their large number of nodes. Overtraining leads to a seeming increase in the classification performance over the objectively achievable one, if measured on the training sample, and to an effective performance decrease when measured with

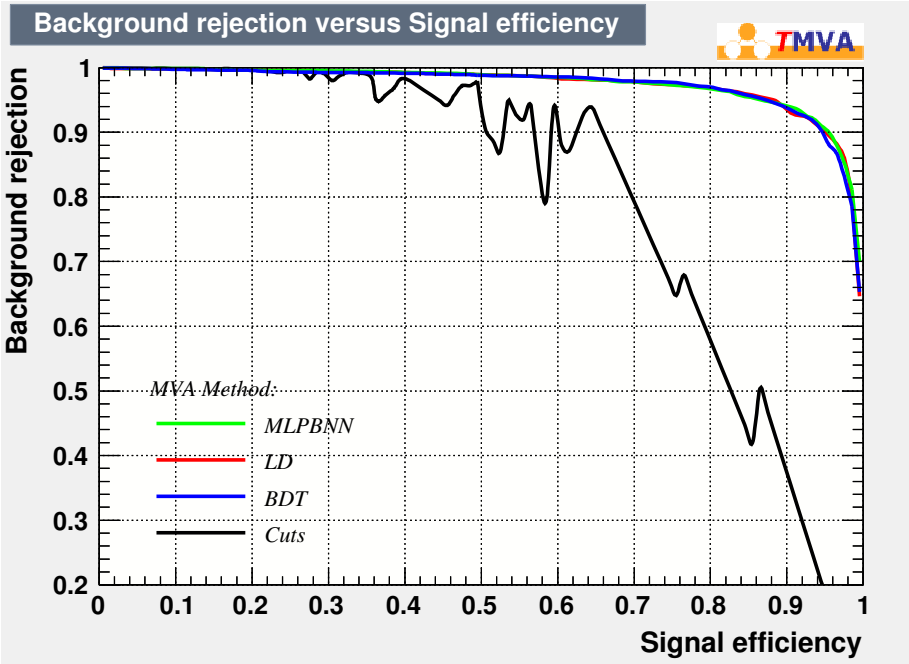

Figure 5.2.4: Background rejection versus signal efficiency plot (ROC curve) for the BDT, LD and MLPBNN classifiers, which are known to have a good performance, as verified by the area covered by their respective curves. The ROC curve for the automatic cuts performed by the MVA algorithm is also shown for comparison.

an independent test sample. A convenient way to detect overtraining and to measure its impact is therefore to compare the performance results between training and test samples. The superimposed responses (of the training and testing samples) of the trained classifiers is presented in fig. 5.2.5. The test and the training samples present similar behaviours/shapes for the three classifiers booked, showing no evidence for overtraining. Hence the focus may turn to the following step in the MVA: the classification phase (section 5.3).

5.3 Applying MVA Classifiers

The BDT, the LD (linear discriminant) and the MLPBNN neural network were applied to this study data sample (refer to section 4.1), to the total background sample, also used in the training/testing of the MVA methods, and to a $T\bar{T}$ production set of signal samples, including quark masses between 350 GeV and 850 GeV in steps of 50 GeV, assuming $SU(2)$ singlet couplings. The outputs of the MVA classifiers are shown for the supracited set of signal samples, for the total background sample and for the data sample (with an unknown distribution of signal and background), in fig. 5.3.1. These histograms will be be the input used to derive limits on the pair-production cross section of a vector-like singlet T quark, with the CLs method [131, 132], which are presented in the next section (6).

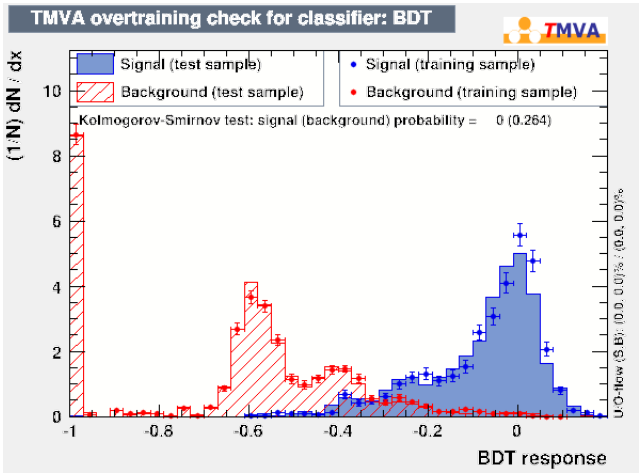

(a)

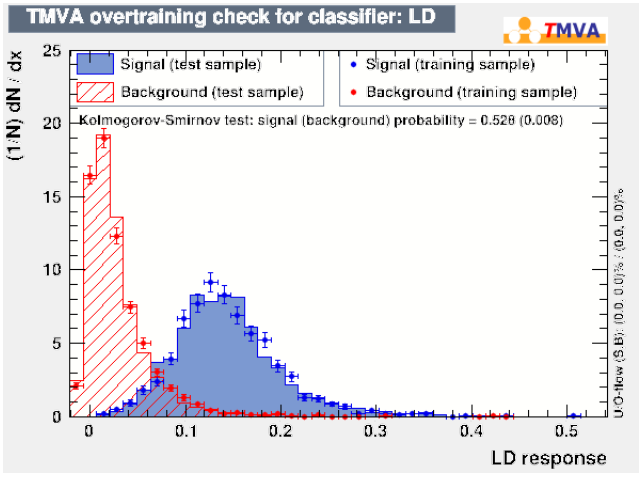

(b)

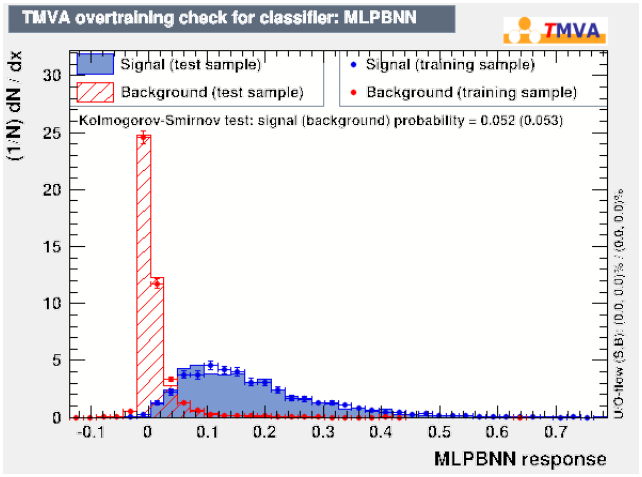

(c)

Figure 5.2.5: Overtraining test, with training and testing samples superimposed, for: (a) BDT, (b) LD and (c) MLPBNN classifiers.

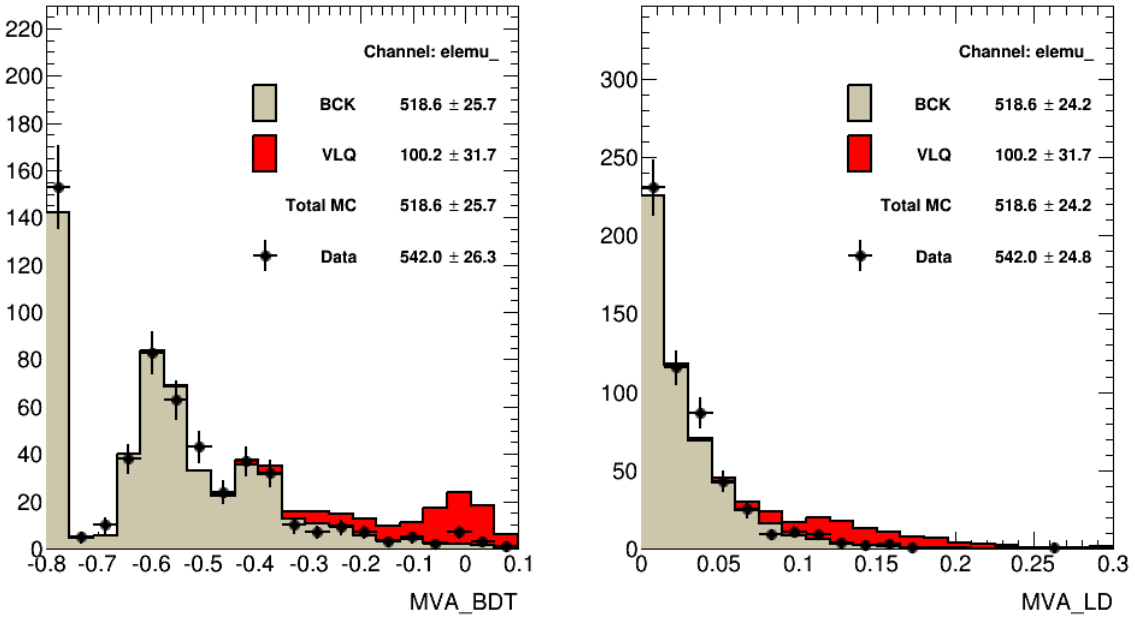

(a) (b)

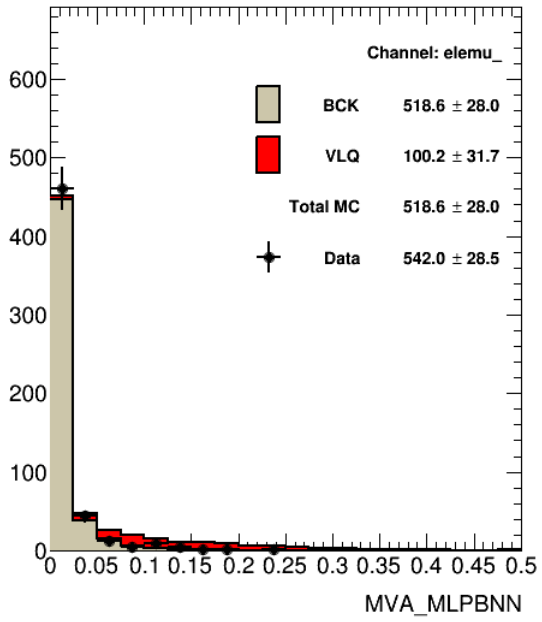

(c)

Figure 5.3.1: Output of the multivariate classifiers employed in this MVA: (a) BDT, (b) LD and (c) MLPBNN. The signal contribution is multiplied by a factor of 10. The leftmost bin in each histogram contains underflow events.

6 Results

A binned Poisson likelihood test is performed on the distributions of the final discriminating variables to assess the compatibility of the observed data with the background-only and signal-plus-background hypotheses, setting upper limits on the pair-production cross section of a vector-like singlet T quark. The test employs a log-likelihood ratio function, $-2\ln(L_{s+b}/L_b)$, where L_{s+b} (L_b) is the Poisson probability to observe data under the signal-plus-background (background-only) hypothesis.

For the pair-production hypotheses, before an MVA analysis, the final discriminating variable used is the $m(Zb)$ distribution shown in fig. 4.6.11, at a final selection level characterized by $H_T > 600$ GeV.

Upper limits are derived according to the CLs prescription [131, 132], and set at the 95% confidence level (C.L.) on the pair-production cross section of a vector-like singlet T quark before (section 6.1.1) and after the employment of multivariate classifiers (section 6.1.2). These cross-section limits are then used to set lower limits on the quark masses.

6.1 Limits On the Singlet T Quark Pair-Production Hypothesis

6.1.1 Before MVA

Fig. 6.1.1 show the pair-production cross-section limit for T quark masses in the interval 350–850 GeV, assuming the branching ratios of an $SU(2)$ singlet T quark. The theoretical curve represents the total pair-production cross section calculated with TOP++, and the width of the curve indicates the uncertainty on the prediction from $PDF + \alpha_s$ and scale uncertainties. The observed (expected) limit on the mass of an $SU(2)$ singlet T quark is 625 GeV(616 GeV), at a 95% confidence level (C.L.).

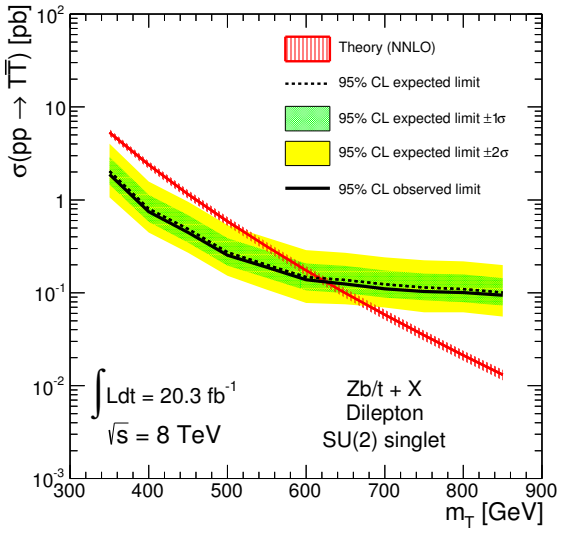

(a)

Figure 6.1.1: Predicted pair-production cross section as a function of the heavy quark mass and observed and expected upper limits for an $SU(2)$ singlet T quark.

6.1.2 After MVA

Fig. 6.1.2 shows the pair-production cross-section limit for T quark masses in the interval 350–850 GeV, assuming the branching ratios of an $SU(2)$ singlet T quark, after the signal-background classification in the frame of a multivariate analysis. These limits are set, at 95% C.L., using the final discriminating variables $p_T(b1)$, $p_T(b2)$, H_T(jets), $\Delta R(b1b2)$ and the reconstructed T invariant mass which were the input of LD, BDT and MLPBNN neural network multivariate methods. Fig. 6.1.2 (a) depicts the pair production cross-section limit for a singlet T, with the results of the MVA classification for a boosted decision tree (BDT). The observed (expected) limit on the mass of an $SU(2)$ singlet T quark is 599 GeV(630 GeV). In fig. 6.1.2 (b) is illustrated the pair production cross-section limit for a singlet T, with the results of the MVA classification for a linear discriminant LD. The observed (expected) limit on the mass of an $SU(2)$ singlet T quark is 611 GeV(642 GeV).

In panel (c) of fig. 6.1.2 is plotted the pair production cross-section limit for a singlet T, with the results of the MVA classification for a MLPBNN neural network. The observed (expected) limit on the mass of an $SU(2)$ singlet T quark is 665 GeV(667 GeV).

All the limits obtained, before and after a multivariate analysis, are organised in table 6.1, for better comparison. The best lower limits on the T quark mass were

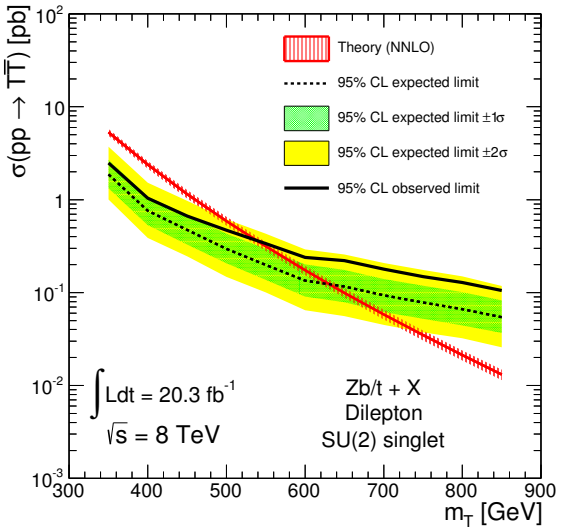

(a)

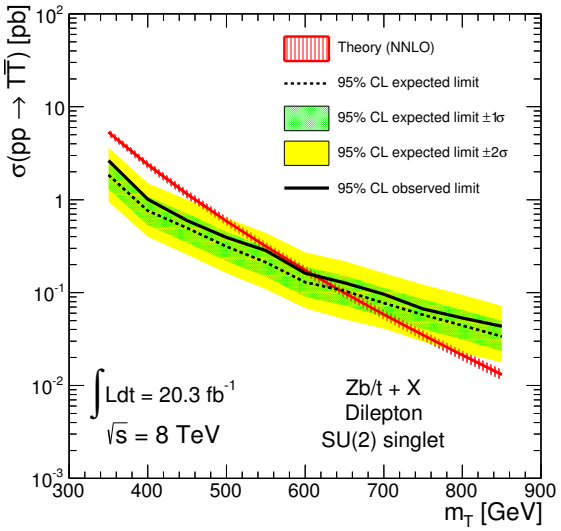

(b)

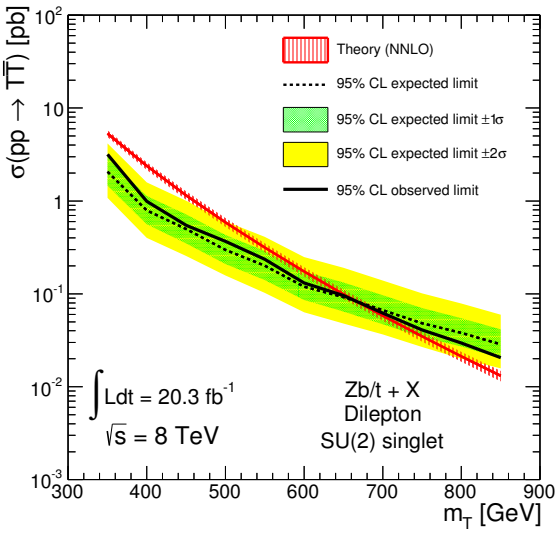

(c)

Figure 6.1.2: Predicted pair-production cross section as a function of the heavy quark mass and observed and expected upper limits for an $SU(2)$ singlet T quark, derived with the outputs of (a) BDT, (b) LD and (c) MLPBNN classifiers.

T singlet observed (expected) mass limit [GeV]			
Before MVA	After MVA		
	BDT	LD	MLPBNN
625(616)	599(630)	611(642)	665(667)

Table 6.1: Observed (expected) 95% C.L. limits on the T quark mass (GeV), assuming pair production of $SU(2)$ singlet quarks, before (left) and after a multivariate analysis (right).

obtained with the results of the MVA classification for a MLBNN neural network, since there is an improvement in the expected limit of 51 GeV, when compared to the limits set before the MVA classification. Furthermore, these results also improve the ones recently published by the ATLAS Collaboration [3], for a combined dilepton+trilepton channel: from an observed (expected) limit on the mass of an $SU(2)$ singlet T quark of 655 GeV (625 GeV) to 665 GeV(667 GeV), when considering the results obtained with the classification obtained with the MLPBNN, which translates to an improvement of 42 GeV, at a 95% confidence level.

7 Conclusions and Further Work

A search for heavy quarks that decay to a Z boson and a third-generation quark has been performed, using a dataset corresponding to an integrated luminosity of 20.3 fb^{-1}, collected by the ATLAS detector at the LHC in pp collisions at $\sqrt{s} = 8\,\text{TeV}$. No evidence for a heavy quark signal is observed when selecting events with topologies sensitive to heavy quark pair-production via the strong interaction. Hence, the results obtained before and after a multivariate analysis using a MLPBNN neural network were used to set lower (observed) mass limits of 625 GeV and 665 GeV (at 95% C.L.), respectively, on vector like T quarks when assuming the $SU(2)$ singlet hypothesis, which confirms the success of multivariate techniques in improving the previously set limits. The mass limit obtained after a MVA also improves the limit recently set by the ATLAS Collaboration [3] in 10 GeV.

Several sources of systematic uncertainty affect the predicted Standard Model backgrounds and signal. However, since this is a search, in which statistical uncertainties dominate over systematics, they were not considered throughout the study. The former can be included in posterior studies. Also, a careful study and optimization of the parameters that characterize the multivariate classifiers employed, as well as using other input discriminating variables, could lead to higher improvements on the limits set for the pair production of not only T singlet quarks, but also B quarks, assuming both $SU(2)$ singlet and doublet hypotheses.

Bibliography

[1] CMS Collaboration. Inclusive search for a vector-like T quark with charge $\frac{2}{3}$ in pp collisions at $\sqrt{s} = 8$ TeV. *Phys.Lett.*, B729:149, 2014.

[2] CMS Collaboration. Search for a vector-like bottom quark partner in same sign di-lepton final states. Technical Report CMS-PAS-B2G-12-020, CERN, Geneva, 2014.

[3] ATLAS Collaboration. Search for pair and single production of new heavy quarks that decay to a Z boson and a third-generation quark in pp collisions at $\sqrt{s} = 8$ TeV with the ATLAS detector. *arXiv:1409.5500 [hep-ex]*, 2014.

[4] M. Aliev, H. Lacker, U. Langenfeld, S. Moch, P. Uwer, et al. HATHOR: HAdronic Top and Heavy quarks crOss section calculatoR. *Comput.Phys.Commun.*, 182:1034, 2011.

[5] ATLAS Collaboration. Search for pair production of new heavy quarks that decay to a Z boson and a third generation quark in pp collisions at 8 TeV with the ATLAS detector. Technical Report ATLAS-CONF-2013-056, CERN, Geneva, June 2013.

[6] J. A. Aguilar-Saavedra. Protos - program for top simulations: http://jaguilar.web.cern.ch/jaguilar/protos.

[7] M. C. N. Fiolhais. Study of the wtb vertex structure in top quark decays with the atlas experiment and future prospects. *Dissertacao de Doutoramento em Fisica, Especialidade de Fisica Experimental, Faculdade de Ciencias e Tecnologia da Universidade de Coimbra, Coimbra*, 2013.

[8] ATLAS Collaboration. The ATLAS Experiment at the CERN Large Hadron Collider. *JINST3 (2008) S08003.*

[9] ATLAS Collaboration. Calibration of the performance of b-tagging for c and light-flavour jets in the 2012 ATLAS data. Technical Report ATLAS-CONF-2014-046, CERN, Geneva, July 2014.

[10] A. Hocker, J. Stelzer, F. Tegenfeldt, H. Voss, K. Voss, et al. TMVA - Toolkit for Multivariate Data Analysis. *PoS*, ACAT:040, 2007.

[11] Y. Okada and L. Panizzi. LHC signatures of vector-like quarks. *Adv.High Energy Phys.*, 2013:364936, 2013.

[12] N. Castro. *Study of the Wtb vertex structure at the ATLAS experiment.* PhD thesis, U. Coimbra, Coimbra, 2008. Presented on 17 Oct 2008.

[13] The ALEPH Collaboration, the DELPHI Collaboration, the L3 Collaboration, the OPAL Collaboration, the SLD Collaboration, the SLD electroweak the LEP Electroweak Working Group, and heavy flavour groups. Precision Electroweak Measurements on the Z Resonance. *ArXiv High Energy Physics - Experiment e-prints hep-ex/0509008*, September 2005.

[14] S. Schael et al. Electroweak Measurements in Electron-Positron Collisions at W-Boson-Pair Energies at LEP. *Phys.Rept.*, 532:119, 2013.

[15] F. Englert and R. Brout. Broken symmetry and the mass of gauge vector mesons. *Phys. Rev. Lett.*, 13:321, August 1964.

[16] G. S. Guralnik, C. R. Hagen, and T. W. B. Kibble. Global conservation laws and massless particles. *Phys. Rev. Lett.*, 13:585, November 1964.

[17] P. W. Higgs. Broken symmetries and the masses of gauge bosons. *Phys. Rev. Lett.*, 13:508, October 1964.

[18] ATLAS Collaboration. Observation of a new particle in the search for the Standard Model Higgs boson with the ATLAS detector at the LHC. *Physics Letters B*, 716:1, 2012.

[19] CMS Collaboration. Observation of a new boson at a mass of 125 GeV with the CMS experiment at the LHC. *Physics Letters B*, 716:30, September 2012.

[20] L. Susskind. Dynamics of spontaneous symmetry breaking in the Weinberg-Salam theory. *Phys. Rev. D*, 20:2619, November 1979.

[21] P. Ramond. Dual Theory for Free Fermions. *Phys.Rev.*, D3:2415, 1971.

[22] Yu. A. Golfand and E.P. Likhtman. Extension of the Algebra of Poincare Group Generators and Violation of P Invariance. *JETP Lett.*, 13:323, 1971.

[23] J. Wess and B. Zumino. A Lagrangian Model Invariant Under Supergauge Transformations. *Phys.Lett.*, B49:52, 1974.

[24] P. Fayet. Supersymmetry and Weak, Electromagnetic and Strong Interactions. *Phys.Lett.*, B64:159, 1976.

[25] F. Iachello. Dynamical supersymmetries in nuclei. *Phys. Rev. Lett.*, 44:772, March 1980.

[26] S. Weinberg. *The Quantum Theory of Fields: Supersymmetry.* The Quantum Theory of Fields. Cambridge University Press, 2000.

[27] C. T. Hill and E. H. Simmons. Strong dynamics and electroweak symmetry breaking. *Phys.Re*, 381:235, July 2003.

[28] N. Arkani-Hamed, A.G. Cohen, E. Katz, and A.E. Nelson. The Littlest Higgs. *Journal of High Energy Physics*, 0207:034, 2002.

[29] M. Schmaltz and D. Tucker-Smith. Little Higgs review. *Ann.Rev.Nucl.Part.Sci.*, 55:229, 2005.

[30] D. B. Kaplan, H. Georgi, and S. Dimopoulos. Composite Higgs scalars. *Physics Letters B*, 136(3):187, 1984.

[31] K. Agashe, R. Contino, and A. Pomarol. The Minimal composite Higgs model. *Nucl.Phys.*, B719:165, 2005.

[32] G.C. Branco and L. Lavoura. On the addition of vector-like quarks to the standard model. *Nuclear Physics B*, 278(3):738, 1986.

[33] P. Ramond. *Proc. 4th Kyoto Summer Institute on Grand Unified Theories and related topics (Kyoto, Japan), eds. M. Konouma and T. Maskawa (World Scientific, Singapore)*, 1981.

[34] F. del Aguila and M.J. Bowick. *Phys.Lett. 119 B 144*, 1982.

[35] F. del Aguila and Mark J. Bowick. The Possibility of New Fermions With Δ I = 0 Mass. *Nucl.Phys.*, B224:107, 1983.

[36] F. del Aguila, M. Perez-Victoria, and Jose Santiago. Effective description of quark mixing. *Phys.Lett.*, B492:98, 2000.

[37] J.A. Aguilar Saavedra. Identifying top partners at LHC. *Journal of High Energy Physics*, 11:30, November 2009.

[38] J.A. Aguilar-Saavedra, R. Benbrik, S. Heinemeyer, and M. Perez-Victoria. Handbook of vectorlike quarks: Mixing and single production. *Phys.Rev.*, D88(9):094010, 2013.

[39] J. Berger, J. Hubisz, and M. Perelstein. A Fermionic Top Partner: Naturalness and the LHC. *Journal of High Energy Physics*, 1207:016, 2012.

[40] O. Eberhardt, G. Herbert, H. Lacker, A. Lenz, A. Menzel, et al. Impact of a Higgs boson at a mass of 126 GeV on the standard model with three and four fermion generations. *Phys.Rev.Lett.*, 109:241802, 2012.

[41] ATLAS Collaboration. Combined coupling measurements of the Higgs-like boson with the ATLAS detector using up to 25 fb^{-1} of proton-proton collision data. Technical Report ATLAS-CONF-2013-034, CERN, Geneva, March 2013.

[42] CMS Collaboration. Combination of standard model Higgs boson searches and measurements of the properties of the new boson with a mass near 125 GeV. Technical Report CMS-PAS-HIG-13-005, CERN, Geneva, 2013.

[43] CMS Collaboration. Search for pair produced fourth-generation up-type quarks in pp collisions at $\sqrt{s} = 7$ TeV with a lepton in the final state. *Phys.Lett.*, B718:307, 2012.

[44] ATLAS Collaboration. Search for pair production of heavy top-like quarks decaying to a high-pT W boson and a b quark in the lepton plus jets final state at $\sqrt{s}$=7 TeV with the ATLAS detector. *Phys.Lett.*, B718:1284, 2013.

[45] S. L. Glashow, J. Iliopoulos, and L. Maiani. Weak interactions with lepton-hadron symmetry. *Phys. Rev. D*, 2:1285, October 1970.

[46] CMS Collaboration. Search for a Vector-like Quark with Charge 2/3 in $t + Z$ Events from pp Collisions at $\sqrt{s} = 7$ TeV. *Phys.Rev.Lett.*, 107:271802, 2011.

[47] ATLAS Collaboration. Search for pair production of a new quark that decays to a Z boson and a bottom quark with the ATLAS detector. *Phys.Rev.Lett.*, 109:071801, 2012.

[48] CMS Collaboration. Search for pair-produced vector-like quarks of charge -1/3 in lepton+jets final state in pp collisions at $\sqrt{s} = 8$ TeV. *Techreport: CMS-PAS-B2G-12-019*, 2012.

[49] ATLAS Collaboration. Search for heavy top-like quarks decaying to a Higgs boson and a top quark in the lepton plus jets final state in *pp* collisions at $\sqrt{s} = 8$ TeV with the ATLAS detector. Technical Report ATLAS-CONF-2013-018, CERN, Geneva, March 2013.

[50] ATLAS Collaboration. Search for anomalous production of events with same-sign dileptons and b jets in 14.3 fb^{-1} of *pp* collisions at $\sqrt{s} = 8$ TeV with the ATLAS detector. Technical Report ATLAS-CONF-2013-051, CERN, Geneva, May 2013.

[51] CMS Collaboration. Search for T5/3 top partners in same-sign dilepton final state. Technical Report CMS-PAS-B2G-12-012, CERN, Geneva, 2013.

[52] ATLAS Collaboration. Search for pair and single production of new heavy quarks that decay to a Z boson and a third generation quark in *pp* collisions at $\sqrt{s} = 8$ TeV with the ATLAS detector. *ATLAS-CONF-2014-036*, CERN, Geneva, 2014.

[53] S. L. Glashow. Partial-symmetries of weak interactions. *Nuclear Physics*, 22(4):579, 1961.

[54] G.'t Hooft. Renormalizable lagrangians for massive yang-mills fields. *Nuclear Physics B*, 35(1):167, 1971.

[55] G. 'tHooft. Renormalization of massless yang-mills fields. *Nuclear Physics B*, 33(1):173, 1971.

[56] T. Nakano and K. Nishijima. Charge independence for v-particles. *Progress of Theoretical Physics*, 10(5):581, 1953.

[57] M. Gell-Mann. The interpretation of the new particles as displaced charge multiplets. *Il Nuovo Cimento*, 4(2):848, 1956.

[58] G. Zweig. An SU(3) model for strong interaction symmetry and its breaking. Version 2. page 22, 1964.

[59] M. Y. Han and Y. Nambu. Three-triplet model with double SU(3) symmetry. *Phys. Rev.*, 139:B1006, August 1965.

[60] O. W. Greenberg. Spin and unitary-spin independence in a paraquark model of baryons and mesons. *Phys. Rev. Lett.*, 13:598, November 1964.

[61] H. David Politzer. Reliable Perturbative Results for Strong Interactions? *Phys.Rev.Lett.*, 30:1346, 1973.

[62] H. D. Politzer. Asymptotic Freedom: An Approach to Strong Interactions. *Phys.Rept.*, 14:129, 1974.

[63] D. J. Gross and F. Wilczek. Ultraviolet Behavior of Nonabelian Gauge Theories. *Phys.Rev.Lett.*, 30:1343, 1973.

[64] J. H. Christenson et al. *Phys.Rev.Lett.13,138*, 1964.

[65] Particle Data Group. *J. Phys. G 37, 075021*, 2010.

[66] H. Burkhardt er al. [NA31 Collab.]. *Phys.Rev.Lett.B 206,169*, 1988.

[67] Belle Collaboration. Observation of large *CP* violation in the neutral *B* meson system. *Phys. Rev. Lett.*, 87:091802, August 2001.

[68] M. Kobayashi and T. Maskawa. CP-Violation in the Renormalizable Theory of Weak Interaction. *Progress of Theoretical Physics*, 49:652, February 1973.

[69] M. Perelstein, M. E. Peskin, and A. Pierce. Top quarks and electroweak symmetry breaking in little higgs models. *Phys. Rev. D*, 69:075002, April 2004.

[70] R. Contino, L. Da Rold, and A. Pomarol. Light custodians in natural composite higgs models. *Phys. Rev. D*, 75:055014, March 2007.

[71] O. Matsedonskyi, G. Panico, and A. Wulzer. Light top partners for a light composite Higgs. *Journal of High Energy Physics*, 2013.

[72] D. B. Kaplan. Flavor at ssc energies: A new mechanism for dynamically generated fermion masses. *Nuclear Physics B*, 365(2):259, 1991.

[73] R. Contino, T. Kramer, M. Son, and R. Sundrum. Warped/composite phenomenology simplified. *Journal of High Energy Physics*, 0705:074, 2007.

[74] K. Huang. *Quarks, Leptons & Gauge Fields.* World Scientific, 1982.

[75] B. A. Dobrescu and C. T. Hill. Electroweak symmetry breaking via top condensation seesaw. *Phys.Rev.Lett.*, 81:2634, 1998.

[76] R. S. Chivukula, B.A. Dobrescu, H. Georgi, and C. T. Hill. Top quark seesaw theory of electroweak symmetry breaking. *Phys.Rev.*, D59:075003, 1999.

[77] C. Anastasiou, E. Furlan, and J. Santiago. Realistic Composite Higgs Models. *Phys.Rev.*, D79:075003, 2009.

[78] A. Carmona, M. Chala, and J. Santiago. New Higgs Production Mechanism in Composite Higgs Models. *Journal of High Energy Physics*, 1207:049, 2012.

[79] B. Grinstein, M. Redi, and G. Villadoro. Low Scale Flavor Gauge Symmetries. *Journal of High Energy Physics*, 1011:067, 2010.

[80] D. Guadagnoli, R. N. Mohapatra, and I. Sung. Gauged Flavor Group with Left-Right Symmetry. *Journal of High Energy Physics*, 1104:093, 2011.

[81] S. P. Martin. Extra vector-like matter and the lightest Higgs scalar boson mass in low-energy supersymmetry. *Phys.Rev.*, D81:035004, 2010.

[82] S. P. Martin. Raising the Higgs mass with Yukawa couplings for isotriplets in vector-like extensions of minimal supersymmetry. *Phys.Rev.*, D82:055019, 2010.

[83] P. Kang, J.and Langacker and B. D. Nelson. Theory and Phenomenology of Exotic Isosinglet Quarks and Squarks. *Phys.Rev.*, D77:035003, 2008.

[84] J.A. Aguilar-Saavedra. Mixing with vector-like quarks: constraints and expectations. *EPJ Web Conf.*, 60:16012, 2013.

[85] F. del Aguila, J.A. Aguilar-Saavedra, and R. Miquel. Constraints on top couplings in models with exotic quarks. *Phys.Rev.Lett.*, 82:1628, 1999.

[86] J.A. Aguilar-Saavedra. Effects of mixing with quark singlets. *Phys.Rev.*, D67:035003, 2003.

[87] A. Atre, M. Carena, T. Han, and J. Santiago. Heavy Quarks Above the Top at the Tevatron. *Phys.Rev.*, D79:054018, 2009.

[88] ATLAS Collaboration. Search for pair production of heavy top-like quarks decaying to a high-p_T W boson and a b quark in the lepton plus jets final state in pp collisions at $\sqrt{s} = 8$ TeV with the ATLAS detector. Technical Report ATLAS-CONF-2013-060, CERN, Geneva, June 2013.

[89] A.D. Martin, W.J. Stirling, R.S. Thorne, and G. Watt. Parton distributions for the LHC. *Eur.Phys.J.*, C63:189, 2009.

[90] A. D. Martin, W. J. Stirling, R. S. Thorne, and G. Watt. Uncertainties on α_S in global PDF analyses and implications for predicted hadronic cross sections. *Eur.Phys.J.*, C64:653, 2009.

[91] J. Marriner. Stochastic cooling overview. *Nucl.Instrum.Meth.*, A532:11, 2004.

[92] L. Evans and P. Bryant. Lhc machine. *Jounal of Instrumentation, 3:S08001*, 2008.

[93] ATLAS Collaboration. Improved luminosity determination in *pp* collisions at $\sqrt{s}$ = 7 TeV using the ATLAS detector at the LHC. *Eur.Phys.J.*, C73:2518, 2013.

[94] ATLAS Collaboration. Atlas computing: Technical design report. technical report cern-lhcc-2005-022, atlas-trd-017, CERN, Geneva, 2005.

[95] ATLAS Collaboration. Luminosity Determination in *pp* Collisions at $\sqrt{s} = 7$ TeV Using the ATLAS Detector at the LHC. *Eur.Phys.J.*, C71:1630, 2011.

[96] ATLAS Collaboration. Electron reconstruction and identification efficiency measurements with the ATLAS detector using the 2011 LHC proton-proton collision data. *Eur.Phys.J.*, C74:2941, 2014.

[97] ATLAS Collaboration. Muon reconstruction efficiency and momentum resolution of the ATLAS experiment in proton-proton collisions at $\sqrt{s}$=7 TeV in 2010. *Arxiv:1404.456*, 2014.

[98] M. Cacciari and G. P. Salam. Dispelling the N^3 myth for the k_t jet-finder. *Phys.Lett.*, B641:57, 2006.

[99] M. Cacciari, G. P. Salam, and G. Soyez. The Anti-k(t) jet clustering algorithm. *Journal of High Energy Physics*, 0804:063, 2008.

[100] M. Cacciari, G. P. Salam, and G. Soyez. FastJet User Manual. *Eur.Phys.J.*, C72:1896, 2012.

[101] Barillari, T. et al. Local Hadronic Calibration. Technical Report ATL-LARG-PUB-2009-001-2., CERN, Geneva, June 2008.

[102] ATLAS Collaboration. Jet energy measurement with the ATLAS detector in proton-proton collisions at $\sqrt{s} = 7$ TeV. *Eur.Phys.J.*, C73:2304, 2013.

[103] ATLAS Collaboration. Commissioning of the ATLAS high-performance b-tagging algorithms in the 7 TeV collision data. Technical Report ATLAS-CONF-2011-102, CERN, Geneva, July 2011.

[104] T. Sjostrand, S. Mrenna, and P. Z. Skands. PYTHIA 6.4 Physics and Manual. *Journal of High Energy Physics*, 0605:026, 2006.

[105] P. Z. Skands. Tuning Monte Carlo Generators: The Perugia Tunes. *Phys.Rev.*, D82:074018, 2010.

[106] H. Lai, M. Guzzi, J. Huston, Z. Li, P. M. Nadolsky, et al. New parton distributions for collider physics. *Phys.Rev.*, D82:074024, 2010.

[107] ATLAS Collaboration. The simulation principle and performance of the ATLAS fast calorimeter simulation FastCaloSim. Technical Report ATL-PHYS-PUB-2010-013, CERN, Geneva, October 2010.

[108] ATLAS Collaboration. The ATLAS Simulation Infrastructure. *European Physical Journal C*, 70:823, December 2010.

[109] GEANT4 Collaboration. Geant4 - a simulation toolkit. *Nuclear Instruments and Methods in Physics Research Section A: Accelerators, Spectrometers, Detectors and Associated Equipment*, 506(3):250, 2003.

[110] S. Catani, L. Cieri, G. Ferrera, D. de Florian, and M. Grazzini. Vector boson production at hadron colliders: a fully exclusive QCD calculation at NNLO. *Phys.Rev.Lett.*, 103:082001, 2009.

[111] T. Gleisberg, S. Hoeche, F. Krauss, M. Schonherr, S. Schumann, et al. Event generation with SHERPA 1.1. *Journal of High Energy Physics*, 0902:007, 2009.

[112] Matteo Cacciari, Michal Czakon, Michelangelo Mangano, Alexander Mitov, and Paolo Nason. Top-pair production at hadron colliders with next-to-next-to-leading logarithmic soft-gluon resummation. *Phys.Lett.*, B710:612, 2012.

[113] M. Beneke, P. Falgari, S. Klein, and C. Schwinn. Hadronic top-quark pair production with NNLL threshold resummation. *Nucl.Phys.*, B855:695, 2012.

[114] Peter Baernreuther, Michal Czakon, and Alexander Mitov. Percent Level Precision Physics at the Tevatron: First Genuine NNLO QCD Corrections to $q\bar{q} \to t\bar{t} + X$. *Phys.Rev.Lett.*, 109:132001, 2012.

[115] M. Czakon and A. Mitov. NNLO corrections to top-pair production at hadron colliders: the all-fermionic scattering channels. *Journal of High Energy Physics*, 1212:54, 2012.

[116] M. Czakon and A. Mitov. NNLO corrections to top pair production at hadron colliders: the quark-gluon reaction. *Journal of High Energy Physics*, 1301:80, 2013.

[117] M. Czakon, P. Fiedler, and A. Mitov. Total Top-Quark Pair-Production Cross Section at Hadron Colliders Through $O(\alpha_S^4)$. *Phys.Rev.Lett.*, 110:252004, 2013.

[118] M. Czakon and A. Mitov. Top++: A Program for the Calculation of the Top-Pair Cross-Section at Hadron Colliders. *Comput.Phys.Commun.*, 185:2930, 2014.

[119] M. Botje, J. Butterworth, A. Cooper-Sarkar, A. de Roeck, J. Feltesse, et al. The PDF4LHC Working Group Interim Recommendations. 2011.

[120] J. Gao, M. Guzzi, J. Huston, Hung-Liang Lai, Z. Li, et al. CT10 next-to-next-to-leading order global analysis of QCD. *Phys.Rev.*, D89(3):033009, 2014.

[121] R. D. Ball, V. Bertone, S. Carrazza, C. S. Deans, L. Del Debbio, et al. Parton distributions with LHC data. *Nucl.Phys.*, B867:244, 2013.

[122] S. Frixione, P. Nason, and C. Oleari. Matching NLO QCD computations with Parton Shower simulations: the POWHEG method. *Journal of High Energy Physics*, 0711:070, 2007.

[123] M. L. Mangano, M. Moretti, F. Piccinini, R. Pittau, and A. D. Polosa. ALPGEN, a generator for hard multiparton processes in hadronic collisions. *Journal of High Energy Physics*, 0307:001, 2003.

[124] G. Corcella, I.G. Knowles, G. Marchesini, S. Moretti, K. Odagiri, et al. HERWIG 6.5 release note. *arXiv: hep-ph/0210213*, 2002.

[125] J. M. Campbell and R. K. Ellis. An Update on vector boson pair production at hadron colliders. *Phys.Rev.*, D60:113006, 1999.

[126] S. Frixione and B. R. Webber. Matching NLO QCD computations and parton shower simulations. *Journal of High Energy Physics*, 0206:029, 2002.

[127] B. P. Kersevan and E. Richter-Was. The Monte Carlo event generator AcerMC versions 2.0 to 3.8 with interfaces to PYTHIA 6.4, HERWIG 6.5 and ARIADNE 4.1. *Comput.Phys.Commun.*, 184:919, 2013.

[128] N. Kidonakis. Differential and total cross sections for top pair and single top production. *arXiv: hep-ph/1205.3453*, page 831, 2012.

[129] J. Alwall, P. Demin, S. de Visscher, R. Frederix, M. Herquet, et al. MadGraph/MadEvent v4: The New Web Generation. *Journal of High Energy Physics*, 0709:028, 2007.

[130] M.V. Garzelli, A. Kardos, C.G. Papadopoulos, and Z. Trocsanyi. $t\bar{t}\,W^{+-}$ and $t\bar{t}\,Z$ Hadroproduction at NLO accuracy in QCD with Parton Shower and Hadronization effects. *Journal of High Energy Physics*, 1211:056, 2012.

[131] T. Junk. Confidence level computation for combining searches with small statistics. *Nucl.Instrum.Meth.*, A434:435, 1999.

[132] A. L. Read. Presentation of search results: The CL(s) technique. *J.Phys.*, G28:2693, 2002.